Mapping The Mantle Transition Zone Beneath Eastern North America

An Automated Receiver Function Approach

Alexander Lower Burky

A Dissertation
Presented to the Faculty
of Princeton University
in Candidacy for the Degree
of Doctor of Philosophy

Recommended for Acceptance
by the Department of
Geosciences

Advisers: Jessica C. E. Irving and Frederik J. Simons

May 2022

© Copyright by Alexander Lower Burky, 2022.
All Rights Reserved.

Abstract

Despite being ever-present beneath our feet, the interior of the Earth remains an enigmatic world of its own. In the last two centuries, the science of *seismology* has begun to peel back the mystery of this world within a world, producing maps of the crust, mantle, outer core, and inner core. The boundaries between these layers are marked by distinct jumps or *discontinuities*, often in chemical composition, and nearly always in seismic velocity. In this thesis, we investigate a particular set of these discontinuities in the mid-mantle, known as the *mantle transition zone*.

This thesis begins with a review of the historical developments in the discovery of the mantle transition zone, and then introduces the method we used to study it—*teleseismic receiver functions*. After this introduction, we present a technical discussion of a key element of seismometry, the *instrument response*. We frame this discussion in the context of a, M_{Lg} 3.1 earthquake that occurred in Marlboro, New Jersey in 2020.

We then continue developing our methods with a receiver function analysis of a seismometer deployed in Bermuda. After discussing the geologic history of the island, we introduce the *iterative time-domain deconvolution* method for calculating receiver functions. With this method, we produce images of the mantle transition zone, and we additionally devise an automated quality control criterion for subsequent receiver function analyses. We find that the transition zone beneath Bermuda is thickened, and discuss potential interpretations in the context of various mineral systems, such as olivine and garnet.

Following this, we apply our methods to a problem of a much larger scale—imaging the mantle transition zone beneath the entirety of eastern North America. Using common conversion point stacks, we produce high-resolution images of the mantle

transition zone. We find three noteworthy features in our stacks: two thinned, and one thickened region. We suggest that the thinned regions are associated with the northern and central Appalachian anomalies. The thickened region is coincident with the supposed location of the Laramide slab. We additionally present an analysis on the effects of different three-dimensional velocity models on the depth correction of receiver functions.

Acknowledgments

A little less than six years ago I moved across the country to pursue a Ph.D. at Princeton. Up to that point, I had spent my whole life living in California. This entire experience would have been impossible without the constant support of my parents and my many siblings, so I would like to thank them first and foremost for always being there for me over the years. To my Dad, thanks for instilling a curiosity about the workings of the universe in me from a very young age, and to my Mom, thanks for encouraging these discussions despite not always being as enthusiastic about having them.

I also want to specifically thank my older brothers: Reb, Matt, and Brent, for always setting a high standard for me while growing up. I don't know if I could have made it this far without having you ever-present as role models throughout my life. To my younger siblings: Mary and Daniel, thanks for giving me the opportunity to be the role model, and thanks for always being willing to listen to me when I ramble on about math, science, programming, or whatever it is I'm thinking about at the moment. Sorry if all of your older brothers set the bar too high. I would also like to thank my entire extended family, for likewise encouraging me to follow my academic passions, particularly my cousin, Johnny, for our many late night discussions about the universe.

I would like to thank my advisors, Jessica Irving and Frederik Simons. Your continued support and probing questions have helped to shape this thesis into what it is today. I have learned and developed immeasurably as a researcher, scientist, and individual under your guidance the past six years here at Princeton. You have encouraged me to produce my best work, in spite of the rigor and difficulty which

that entails, and I thank you for not going too easy on me. It has been a pleasure to work with both of you, and I cannot imagine a better set of mentors for my Ph.D. Furthermore, I would like to thank my advisory and generals committee members: Blair Schoene, Vadim Levin, and Jeroen Tromp. Your thoughtful and critical feedback has been invaluable in helping to hone my skills as a scientist.

The Geosciences family has been incredibly helpful in making all of my work here possible, and I would like to thank Dawn, Mary Rose, Sheryl, and Nora for always supporting me administratively. To my fellow graduate students on the third floor, and throughout the Geosciences Department, thanks for making my time at Princeton as enjoyable as it has been. To Joel, James, Leah, Wenbo, and Yajun thanks for setting a good example for me in my first years, and for helping to ease me into life as a Ph.D. student. To the remaining members of my cohort, Donghoon and John, it feels great to have made it this far with both of you. And to all of the younger students, especially Chao, Congyue, Lucas, Srijan, Sirawich, Ryan, and Travis, thanks for all of the fun memories. We had many, many great meals together, and I will miss all of our great barbecue experiences. Finally, I would like to thank Kenzie for making my last few years at Princeton as happy and fun as they could be. I can't wait to see where our adventures take us next.

Contents

Abstract . . . iii
Acknowledgments . . . v
List of Figures . . . ix

1 Introduction **1**
1.1 The Mantle Transition Zone . . . 1
1.2 Receiver Functions . . . 5
1.3 Summary of Chapters . . . 8

2 Instrument response removal and the 2020 M_{Lg} 3.1 Marlboro, New Jersey, earthquake **10**
2.1 Abstract . . . 10
2.2 Motivation . . . 11
2.3 Mathematical Model . . . 12
2.4 The Transfer Function . . . 13
2.5 SAC Implementation . . . 16
2.6 Open-Source Implementation: `rflexa` . . . 17
2.7 The 2020 Marlboro Earthquake . . . 19
2.8 Conclusion . . . 23
2.9 Data and Resources . . . 24
2.10 Acknowledgments . . . 24

3 Mantle transition zone receiver functions for Bermuda: automation, quality control, and interpretation **25**
3.1 Abstract . . . 25
3.2 Introduction . . . 26
3.3 Data and Methods . . . 32
3.3.1 Receiver Functions . . . 33
3.3.2 Iterative Time-Domain Deconvolution . . . 35
3.3.3 Automating Receiver Function Quality Control . . . 38
3.3.4 Time-to-Depth Conversion . . . 41
3.4 Results . . . 43
3.4.1 Comparison of Manual and Automated Data Selection . . . 43
3.4.2 Frequency Dependence of Results . . . 48
3.5 Discussion . . . 51
3.5.1 Estimation of a Thermal Anomaly . . . 52

3.5.2 Assessment and Interpretation of Discontinuity Structure . . . 53
3.6 Conclusion . . . 55
3.7 Acknowledgments . . . 55
3.8 Supplement . . . 56
3.8.1 Synthetic Data . . . 56
3.8.2 Vespagrams . . . 56
3.8.3 Effects of Filtering and Gaussian Width . . . 61

4 The mantle transition zone beneath eastern North America: A record of subduction and hotspot volcanism 64
4.1 Abstract . . . 64
4.2 Introduction . . . 65
4.2.1 The Northern Appalachian Anomaly . . . 67
4.2.2 The Central Appalachian Anomaly . . . 68
4.3 Data & Modeling . . . 69
4.4 Methods . . . 71
4.4.1 Time to Depth Conversion . . . 73
4.4.2 Common Conversion Point Stacking . . . 74
4.5 Results . . . 75
4.6 Discussion . . . 80
4.6.1 The Importance of 3-D Moveout Corrections . . . 80
4.6.2 The Northern Appalachian Anomaly . . . 82
4.6.3 The Central Appalachian Anomaly . . . 84
4.6.4 MTZ Thickening Associated with the Laramide Slab . . . 85
4.7 Conclusion . . . 86
4.8 Acknowledgments . . . 87
4.9 Supplement . . . 87

5 Conclusion 100
5.1 Summary of Contributions . . . 100
5.2 Looking Forward . . . 101

A Additional Figures and Data Products 103
A.1 Tomographic Cross Sections . . . 103
A.2 Quality Control and Crustal Thickness . . . 106
A.3 The US Array Receiver Function Explorer . . . 107

B Software Guide: `rflexa` 111
B.1 `fetchRF` . . . 112
B.2 `computeRFs` . . . 113
B.3 `iterdecon` . . . 114
B.4 `transfer` . . . 115
B.5 `qcRF` . . . 116
B.6 `rfDepcon` . . . 117
B.7 Utility Functions . . . 118

References 118

List of Figures

1.1 Mantle transition zone triplication . . . 3
1.2 IASP91 velocity model . . . 4
1.3 Mantle transition zone cartoon . . . 6
1.4 Mantle transition zone receiver function diagram . . . 7

2.1 Instrument response plots . . . 14
2.2 Marlboro earthquake unprocessed seismograms . . . 20
2.3 Marlboro earthquake processed seismograms . . . 21
2.4 Instrument response method comparison . . . 22

3.1 Bermuda bathymetry . . . 28
3.2 Tomographic cross sections . . . 30
3.3 Receiver function data example . . . 34
3.4 Quality control illustration . . . 39
3.5 Bermuda dataset statistics . . . 44
3.6 Receiver function stacks . . . 46
3.7 Receiver function record sections . . . 47
3.8 Frequency dependence of receiver functions . . . 49
3.9 Synthetic receiver function record sections . . . 57
3.10 Vespagrams - median slowness . . . 59
3.11 Vespagrams - 65° slowness . . . 60
3.12 Frequency sweep - high to low . . . 62
3.13 Gaussian width variation . . . 63

4.1 USArray network map . . . 70
4.2 Dataset teleseismic earthquake locations . . . 72
4.3 CCP stack piercing points . . . 73
4.4 CCP slice A-A' . . . 77
4.5 CCP slice B-B' . . . 78
4.6 CCP slice C-C' . . . 79
4.7 Eastern North America mantle transition zone summary . . . 81
4.8 Mantle transition zone model differences . . . 83
4.9 Time to depth curves . . . 89
4.10 Northern Appalachian anomaly . . . 90
4.11 Central Appalachian anomaly . . . 91
4.12 Laramide slab anomaly . . . 92

4.13 Model differences - 410 93
4.14 Model differences - 660 94
4.15 Mantle transition zone amplitudes 95
4.16 CCP correlation: GyPSuM vs. GLADM25 96
4.17 CCP correlation: GyPSuM vs. SL2013NA 97
4.18 CCP correlation: LLNL_G3D_JPS vs. GLADM25 97
4.19 CCP correlation: LLNL_G3D_JPS vs. GyPSuM 98
4.20 CCP correlation: LLNL_G3D_JPS vs. SL2013NA 98
4.21 CCP correlation: SL2013NA vs. GLADM25 99
4.22 CCP correlation: IASP91 vs IASP91 + CRUST1.0 99

5.1 Summary of eastern North American MTZ anomalies 101

A.1 Tomography cross section A-A' 104
A.2 Tomography cross section B-B' 105
A.3 Tomography cross section C-C' 105
A.4 USArray $\bar{\nu}$ map 106
A.5 CRUST1.0 Moho depths 107
A.6 CRUST1.0 sediment thickness 108
A.7 US Array receiever function explorer 109
A.8 TA.N61A automated receiver function 109
A.9 TA.O61A automated receiver function 110
A.10 TA.P61A automated receiver function 110

Chapter 1

Introduction

In this thesis, I investigate the nature of the mantle transition zone (MTZ) beneath eastern North America and the western Atlantic using teleseismic receiver functions. This technique produces images of *seismic discontinuities*, locations where elastic wavespeeds have a sudden jump, in the Earth's interior. These discontinuities in the MTZ are thought to be largely the expression of *phase transitions* in the olivine, $(Mg,Fe)_2SiO_4$, mineral system, a ubiquitous mineral in much of the Earth's crust and mantle. The roles of additional minerals, such as garnet, are explored more fully in Chapter 2. Aside from the novelty of observing signals from processes occurring hundreds of kilometers beneath our feet, MTZ receiver functions can give us insight into the *regional variability* of these processes. To set the stage for this dissertation, we briefly review key historical developments in our understanding of the MTZ, and give a brief overview of the receiver function technique.

1.1 The Mantle Transition Zone

The mantle transition zone is a global feature which exists hundreds of kilometers beneath our feet, at depths of roughly 400 to 700 km. Due to its remote nature, most of our knowledge of this region comes from the echoes of seismic waves bouncing around our planet's interior in the aftermath of large earthquakes. Pioneering work

on the MTZ occurred in the early 20th century, as advances in technology and global communication allowed seismologists to construct travel time curves - records of the arrival times of seismic waves as a function of the distance from the earthquake to the seismometer (Bullen 1956). One particularly curious feature was deemed a *triplication*, a segment of the record where multiple waves would arrive at certain distances but not others (see Figure 1.1). Perhaps the most famous investigation of this sort of feature was the one performed by Andrija Mohorovičić, a Croatian seismologist, in the aftermath of an earthquake in October of 1909. By carefully measuring the arrival times of waves from this earthquake recorded across Europe, Mohorovičić concluded that there must be a sharp jump in the velocity of P waves at about 30 km beneath Earth's surface, causing the triplication he observed in the travel-time data (Mohorovičić 1992). This seismological feature has since been dubbed the Moho, in honor of its discoverer, and is observed globally as the boundary between the crust and the mantle.

Just like the "Moho", the discontinuities of the mantle transition zone were gradually discovered as global features as greater and greater volumes of seismic data necessitated their existence. Not long after the work of Mohorovičić, Byerly (1926) drew attention to a discontinuous branch of a travel-time curve in the aftermath of an earthquake in Montana at an epicentral distance of 20° (see Figure 1.1). According to his calculations, this observation indicated a discontinuity in seismic wavespeeds at a depth of roughly 400 km, and in the following decades this feature would be known in the seismological community as the "20° discontinuity" (Nishimura et al. 1958, Lehmann 1970). In the remaining half of the 20th century, massive advances in computational technology and seismometry progressively refined our understanding of the seismic structure of the Earth's interior, culminating in global average Earth models such as PREM (Dziewoński & Anderson 1981). In these models, the 20° dis-

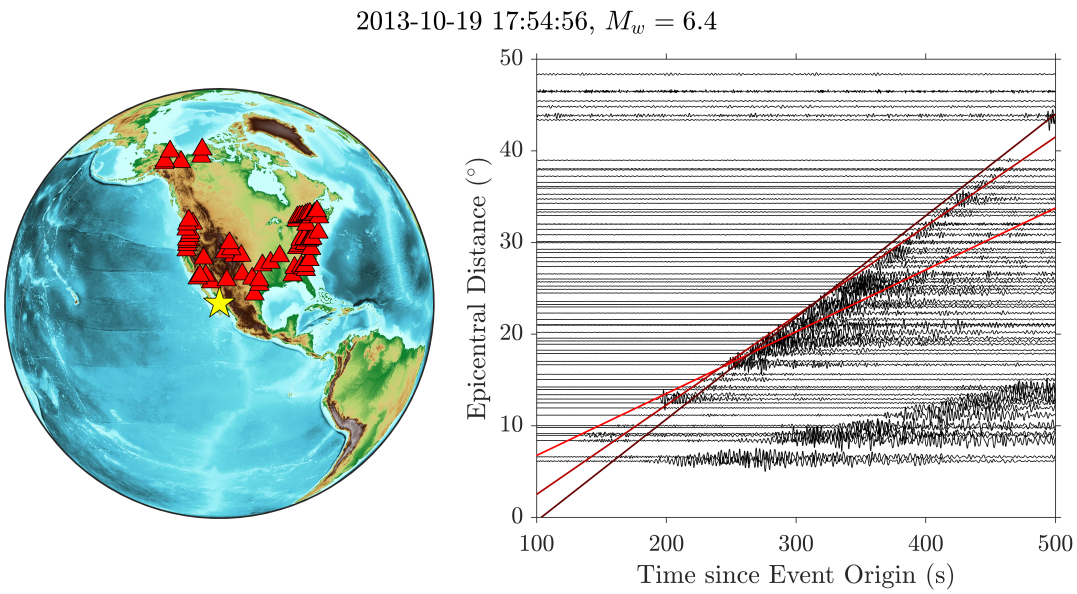


Figure 1.1: A modern observation of the 20° discontinuity. (Left) Map showing the location of a $M_w = 6.4$ earthquake (yellow star) in Baja California recorded by seismometers across North America (red triangles). (*Right*) Record section showing the signals recorded at the seismometers shown on the map. The three overlain lines are attempts to fit the first arrivals using simple constant velocity layers. Note that the slopes of these lines are required to change around 20°, indicating that the seismic velocities must increase at some depth. This type of analysis led to the earliest seismic observations of the mantle transition zone.

continuity became a more formalized feature, known as the mantle transition zone, with two jumps in seismic velocity at depths of 400 and 670 km.

At this point, seismologists could confidently assert the existence of these discontinuities in the MTZ, but entirely different techniques would be required to answer *why* they were occurring. The study of *mineral physics* would be critical in providing these answers, particularly, investigations of the behavior of different mineral compositions at the elevated temperatures and pressures of the Earth's interior. An early analysis by Birch (1952) concluded that high-pressure phases were required to account for seismic observations beneath 900 km, and that somewhere between 200 and 900 km phase transitions or compositional changes must occur. He suggested that one plausible transition which could explain a discontinuity at around 400 km

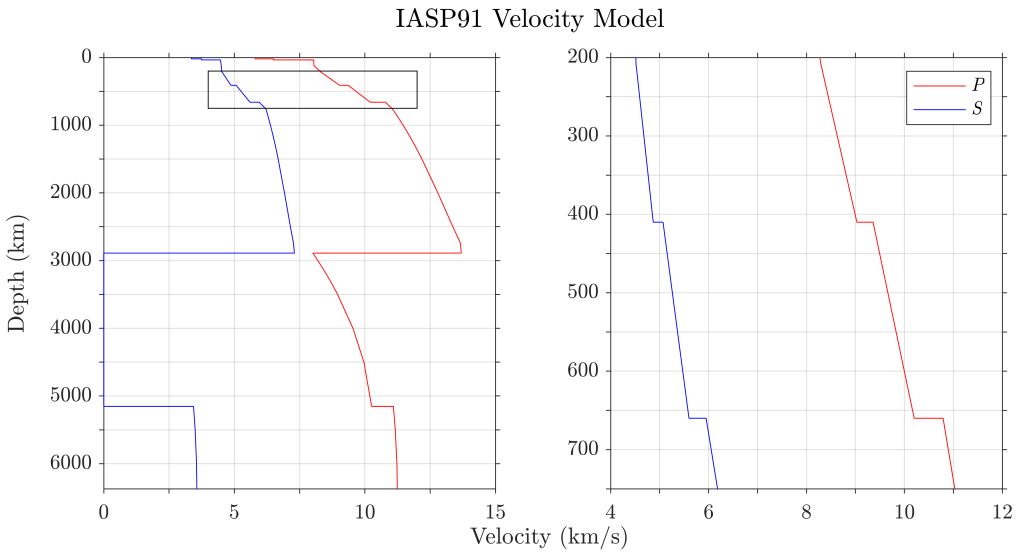


Figure 1.2: Profiles of the P and S wave velocities as a function of depth for the (*Left*) entire Earth, and (*Right*) mantle transition zone, according to 1-D model IASP91 (Kennett & Engdahl 1991). Note the two discontinuities in the mantle transition zone at depths of 410 and 660 km, respectively.

depth was the transition of olivine to a high-pressure cubic phase. However, this phase could not be experimentally verified at the time. Birch seemed well aware of the importance of verifying the existence of such a phase, and he even went so far as to state that, "the transitional layer appears to hold the key to a number of major geophysical problems" (Birch 1952).

With the invention of the diamond anvil cell in 1958 (Piermarini 2001), mineral physicists could finally begin to experimentally explore the behavior of different mineral assemblages under the temperatures and pressures of the MTZ. The suspicions of Birch proved correct, and it was shown that olivine transformed to β-$(Mg,Fe)_2SiO_4$ at pressure and temperature conditions consistent with a depth of roughly 400 km (Akimoto & Fujisawa 1968). In addition, a second discontinuity around 650 km was experimentally verified as the transition from $(Mg,Fe)_2SiO_4$ spinel to $MgSiO_3$ perovskite and (Mg,Fe)O magnesiowüstite (Ringwood 1991). These breakthroughs even provided estimates of the Clapeyron slopes of these phase transitions, relations between the associated pressure and temperature of the mineral transformation. This

information opened the door to interpretive studies of the regional variability of the MTZ, an exercise undertaken in a large part of this thesis.

Modern seismic MTZ studies are chiefly concerned with making high-resolution determinations of the exact depths of the 410 and 660 km discontinuities (e.g. Deuss et al. 2013). Since the pressure in the Earth's interior is approximately homogeneous at a given depth, and mineral phase transitions are chiefly controlled by pressure and temperature, any regional variation in the depth of an MTZ discontinuity can be viewed as an indication of thermal variability. Due to the opposite Clapeyron slopes of the 410 and 660 phase transitions (e.g. Jenkins et al. 2016), a simple rule of thumb can be used to relate the thickness of the MTZ and the sign of a potential thermal anomaly (see Figure 1.3): when it is hot, the MTZ is expected to be thin, and when it is cold, the MTZ is expected to be thick. As with many rules of thumb, this one has its shortcomings, which are explored more fully in the Chapter 3 of this thesis (Burky et al. 2021*b*). In spite of these shortcomings, seismic determinations of the depths of the 410 and 660 remain incredibly valuable as one of the few techniques we have for probing this remote region of our planet.

1.2 Receiver Functions

As stated in the outset, the main tool which we will employ in our investigations of the MTZ in this thesis is the *teleseismic receiver function*. A thorough overview of the theory behind receiver functions is given in Chapter 3, so we will limit the discussion here to a brief overview of the key ideas and major historical developments. A receiver function can be thought of as the *transfer function* of a *linear time-invariant* system, which takes a single input and produces a single output. In our particular application, the input is a P wave, and the output is a sequence of converted S waves. The receiver function therefore characterizes the Earth properties which convert P waves

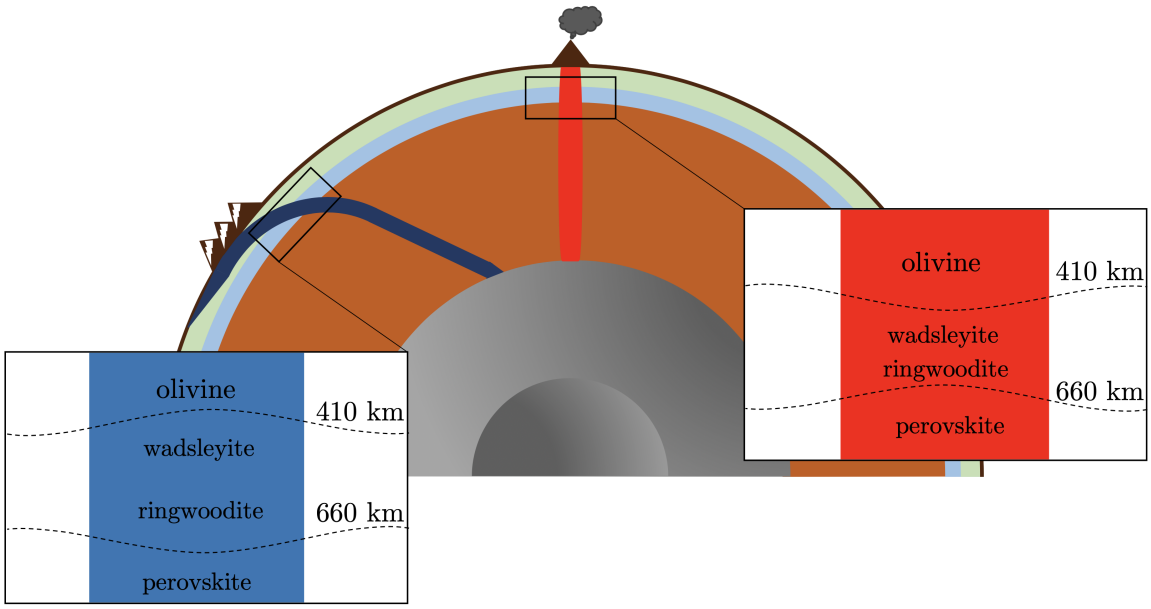


Figure 1.3: Simplified cartoon of the behavior of the mantle transition zone discontinuities in two different tectonic settings. In cold enviornments, such as in the presence of subducting oceanic crust, the transition zone is expected to thicken. On the contrary, in warm environments, such as in the presence of an upwelling mantle plume, the transition zone is expected to thin. These simple yet powerful relationships allow us to use seismology to map out the thermal state of the mantle.

to S waves, e.g. seismic discontinuities. If we can isolate the converted S waves and the incident P wave on a seismogram, then we can construct a receiver function and determine the depths at which these phase conversions occurred (see Figure 1.4).

One of the most desirable features of receiver functions is their focused geographic resolution. In order to produce a receiver function, all that one needs is a single seismometer and a single earthquake. For this reason, receiver functions are often employed in remote locations where data availability is scarce, such as on an island in the middle of the ocean (see Chapter 3) , or on the surface of an extraterrestrial body (e.g. Lognonné et al. 2020). In addition, this focused geographic resolution gives receiver functions an advantage over other body wave methods of investigating the MTZ, such as SS or PP precursors (e.g. Waszek et al. 2018), since there is a short and well-defined path from the discontinuities of interest to the seismometer (see Figure 1.4).

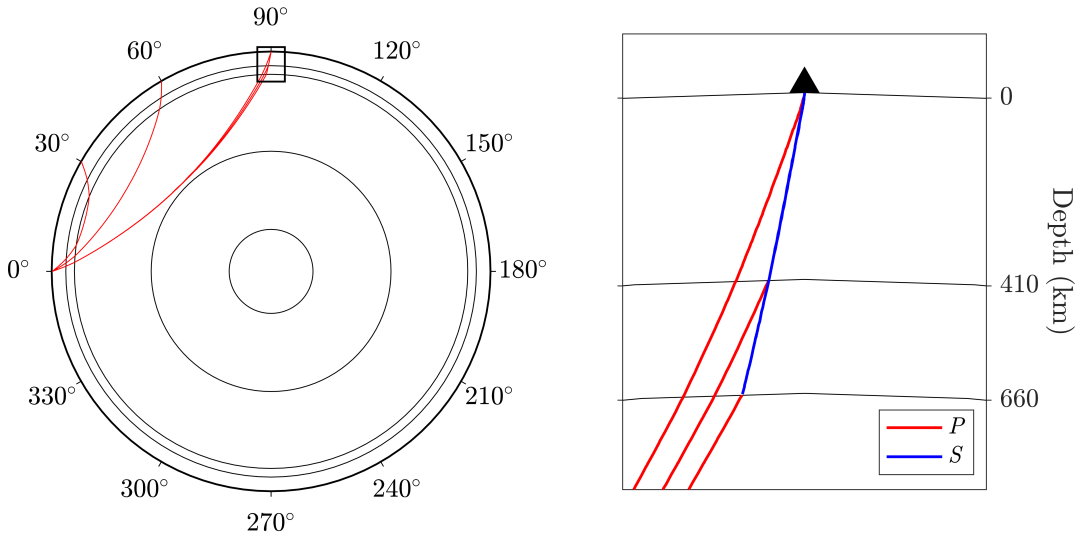


Figure 1.4: (*Left*) Raypaths of body wave phases typically used in MTZ receiver function studies. Note that rays from events with epicentral distances less than 30° do not reach the MTZ, and rays from events with epicentral distances greater than 90° begin to get diffracted by the outer core. (*Right*) Inset showing the phase conversions from the MTZ beneath a seismometer (black triangle) that can be isolated with the receiver function technique.

Historically, one of the earliest applications of "receiver functions" can be traced to work done by Phinney (1964), right here from the Department of Geosciences at Princeton University. Phinney proposed that the ratio of the vertical component spectrum to the horizontal component spectrum of seismic data produced a function which depended on the structure beneath a station. He then applied this method of calculating spectral ratios to data from New Mexico and Bermuda, and determined the thickness of the crust at each location to be roughly 40 and 12 km thick, respectively. After Phinney, the receiver function concept was formalized in a comprehensive paper by Langston (1979), where he applied the method to an investigation of the strcuture of the crust beneath Mount Rainier in Washington.

At roughly the same time as Langston's work on crustal applications of receiver functions, (Vinnik 1977) published the first application of this method to converted phases from the MTZ. By isolating P to SV converted phases in the long-period

P wave coda of seismic records, Vinnik was able to detect signals from seismic discontinuities near 410 and 660 km depth. This work provided seismologists with a geographically focused probe of the MTZ, but was still limited by sparse data availability and limited computational resources.

Fast-forwarding to the present, receiver functions have become a ubiquitous tool for seismic studies ranging from the near surface down to the MTZ. Due to their ease of computation, receiver functions have become a routine data product, and they are calculated for nearly every seismic deployment involving three-component seismometers (e.g. Crotwell & Owens 2005). Receiver functions have been employed on global scales to studies of the MTZ, from which we have come to learn that it is a global boundary (e.g. Shearer & Masters 1992, Andrews & Deuss 2008). Despite this, the ever-increasing quantity and quality of seismic data warrants the continued application and study of receiver functions to a wide variety of geophysical research. In this thesis, we hope to show that there are still many things to learn about the MTZ from receiver functions, and that many of the nuances of this method require careful and precise consideration.

1.3 Summary of Chapters

Following the introduction, this dissertation contains two independently published research articles (Chapters 2 and 3), a third article which has been submitted and is awaiting review (Chapter 4), and a conclusion (Chapter 5). All of this work was performed under the supervision of Jessica Irving and Frederik Simons, and aside from Chapters 1, 5, and the Appendices, only complete, first-authored manuscripts are included in this dissertation.

In Chapter 2, we explore a necessary process in all observational seismology workflows - the correction for the *instrument response*. We review the theory of transfer

functions and convolution, and in doing so hope to demystify a step which is frequently taken for granted when processing seismic data. This work sets the foundation for the following two chapters, which build up toward a fully automated data processing workflow for MTZ receiver function research. In Chapter 3, the focus shifts to the acquisition, processing, and analysis of large volumes of data recorded by a seismometer in Bermuda. This work introduces *receiver functions* as a tool to investigate the discontinuity structure of the MTZ, and provides a thorough review of the iterative time domain deconvolution algorithm (Ligorría & Ammon 1999). Our observations are then interpreted in the context of Bermuda's geologic history and tectonic setting.

In Chapter 4, our most recent work, we apply the methods developed in Chapters 2 and 3 to a problem of a much grander scale - imaging the MTZ beneath a massive swath of eastern North America. Using receiver functions in conjunction with *common conversion point stacking*, we produce high-resolution images of the MTZ. We then discuss these images in the context of the complex and varied history of the region, paying particular attention to three regions of interest. To round out this dissertation, Chapter 5 summarizes these projects and describes potential future work to build on this research.

Chapter 2

Instrument response removal and the 2020 M_{Lg} 3.1 Marlboro, New Jersey, earthquake*

2.1 Abstract

To better understand earthquakes as a hazard, and to better understand the interior structure of the Earth, we often want to measure the physical displacement, velocity, or acceleration at locations on the Earth's surface. To that end, a routine step in an observational seismology workflow is the removal of the instrument response, required to convert the digital counts recorded by a seismometer to physical displacement, velocity, or acceleration. The conceptual framework, which we briefly review for students and researchers of seismology, is that of the seismometer as a linear time-invariant system, which records a convolution of ground motion via a transfer function that gain-scales and phase-shifts the incoming signal. In practice, numerous software packages are widely employed to undo this convolution via deconvolution of the instrument's transfer function. Here, to allow the reader to understand this

*This chapter was published with the citation **Burky, A. L.**, Irving, J. C. E., & Simons, F. J. (2021). Instrument response removal and the 2020 M_{Lg} 3.1 Marlboro, New Jersey, earthquake. *Seismol. Res. Lett., 92*, 3865–3872, doi: 10.1785/0220210118.

process, we start by taking a step back to fully explore the choices made during this routine step, and the reasons for making them. In addition, we introduce open-source routines in Python and MATLAB, as part of our `rflexa` package, which identically reproduce the results of the Seismic Analysis Code (SAC), a ubiquitous and trusted reference. The entire workflow is illustrated on data recorded by several instruments on Princeton University campus in Princeton, New Jersey, of the September 9, 2020 magnitude 3.1 earthquake in Marlboro, New Jersey.

2.2 Motivation

As seismologists, we are interested in analyzing the ground motion at a particular location, often in the aftermath of an earthquake. To accomplish this task, in modern seismology, large deployments of digital broadband seismometers, accelerometers, and other ground motion sensors are installed around the globe.

These instruments sense the ground motion at their location, recording a digital version of how they respond mechanically and electrically to the ongoing motion (Bormann 2012, Havskov & Alguacil 2016). Hence, a seismogram is a digitized version of the analog quantities of interest, i.e. displacement, velocity, or acceleration, convolved with the instrument response, expressed in 'counts' (Ringler & Bastien 2020).

The details of the digitization process (see, e.g., Asch 2009) are beyond the scope of this chapter. As scientists, we are typically interested in undoing the effects of the instrument to arrive back at the original physical quantities of interest. In order to accomplish and understand this process, we require some results from the theory of linear time-invariant systems (see, e.g., Scherbaum 2001), namely, the properties of convolution and deconvolution, which we briefly review here.

2.3 Mathematical Model

The seismometer is modeled as a linear time-invariant system, which takes an input signal, $x(t)$, and produces an output signal, $y(t)$, according to the convolution integral

$$y(t) = \int_{-\infty}^{\infty} x(t-\tau)h(\tau)\,d\tau, \tag{2.1}$$

where $h(\tau)$ is referred to as the *impulse response* of the system. In our scenario, the observed, causal, output of the seismometer is $y(t)$, the physical ground motion is $x(t)$, and the effect of the conversion is captured by the impulse response, $h(\tau)$. In order to solve this equation for $x(t)$, we can use a well-known property of convolution integrals: that the convolution of two functions in the time domain amounts to a multiplication of those functions in the frequency (Laplace or Fourier) domain. This allows us to rewrite eqn. (2.1) as

$$y(t) = \mathcal{L}^{-1}\{Y(s)\} = \mathcal{L}^{-1}\{X(s)H(s)\}, \tag{2.2}$$

where $Y(s) = \mathcal{L}\{y(t)\}$, $X(s) = \mathcal{L}\{x(t)\}$, $H(s) = \mathcal{L}\{h(t)\}$, $\mathcal{L}$ represents the Laplace transform,

$$X(s) = \mathcal{L}\{x(t)\} = \int_{0}^{\infty} x(t)\,e^{-st}\,dt, \tag{2.3}$$

with $\mathcal{L}^{-1}$ its inverse, and $s = \sigma + i\omega$ is a complex number, with angular frequency $\omega = 2\pi f$, where f is the common frequency (in Hz). In the transformed space, the Laplace domain, $H(s)$ is called the *transfer function*. The equivalent (though not identical) quantity in the Fourier domain is the *complex frequency response* (Wielandt 2012).

The transfer function can be represented as the ratio of two complex-valued poly-

nomials (Scherbaum 2001),

$$H(s) = k\frac{(s-z_1)(s-z_2)...(s-z_m)}{(s-p_1)(s-p_2)...(s-p_n)}, \tag{2.4}$$

with zeros z_i, $i = 1, \ldots, m$, and poles p_i, $i = 1, \ldots, n$, and a gain of k. Therefore, knowledge of the poles, zeros, and gain of the seismometer allows us to construct the transfer function and successfully remove it from the seismogram.

If we rearrange eqn. (2.2), we can solve for $x(t)$ as

$$x(t) = \mathcal{L}^{-1}\left\{\frac{Y(s)}{H(s)}\right\}. \tag{2.5}$$

This reduces our problem of solving for the ground motion $x(t)$ to a division of the Laplace (or Fourier) transform of the seismogram by the instrument's transfer function (or the complex frequency response), which is simple in theory but requires care in practice. It is worth noting that in the preceding discussion we have been working within the framework of continuous variables and infinite time. In practice, seismograms are finite-time, discretized time series, and all of the aforementioned operations are replaced by their discrete counterparts, accompanied by appropriate preprocessing steps, including demeaning, detrending, and treatment of the edges (e.g., tapering, zero-padding).

2.4 The Transfer Function

Transfer functions are made publicly available for all broadband digital seismometers deployed by the major seismological research consortia (i.e. IRIS, GSN, GEOSCOPE, etc.). In practice, the information is typically stored in the form of a `RESP` or a `SAC_PZ` file, but the critical information we need to correct the signal for the instrument response are the poles, zeros, and the gain constant of the system.

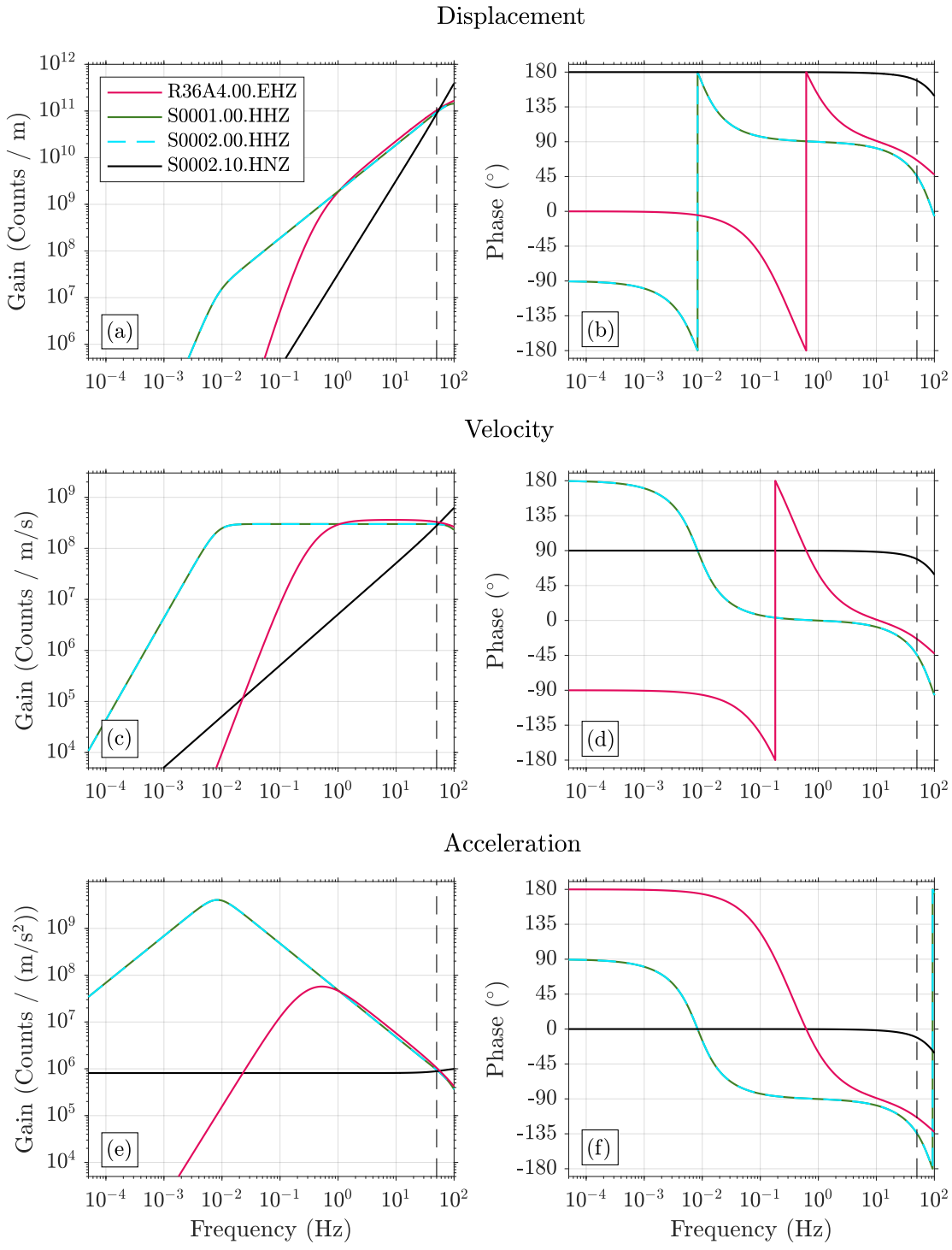


Figure 2.1: (a,b) Displacement, (c,d) velocity, and (e,f) acceleration amplitude and phase responses of a variety of instruments which recorded the Marlboro, New Jersey earthquake in 2020. The Nyquist frequency of each instrument is indicated by the dashed vertical line at 50 Hz. Note that the amplitude responses to velocity of the Nanometrics Trillium Compact 120s seismometers and the Raspberry Shake 3D are flat, as is the response to acceleration of the Titan 1g accelerometer.

As a complex-valued function, the transfer function can be difficult to visualize and comprehend. Fortunately, the effect of the transfer function on the amplitude and phase of an input signal can be extracted to help us gain a better understanding of what it represents.

The *amplitude response* of the system can be calculated by taking the absolute value of the transfer function, using:

$$|H| = \sqrt{\mathrm{Re}(H)^2 + \mathrm{Im}(H)^2}. \tag{2.6}$$

Geometrically, this is the length of the complex-valued H, given by the square root of the sum of the squares of its real and imaginary parts.

The *phase response* of the system is calculated by finding the argument of the transfer function, using:

$$\mathrm{Arg}\{H\} = \mathrm{atan2}\{\mathrm{Im}(H), \mathrm{Re}(H)\}. \tag{2.7}$$

Geometrically, this is the angle that the complex-valued H makes with the real axis, given by the arctangent of the ratio between its imaginary and real parts.

Figure 2.1 shows examples of the amplitude and phase responses, as a function of frequency f, for the vertical component of a Raspberry Shake 3D (R36A4.00), two Nanometrics Trillium Compact 120s seismometers (S0001.00 and S0002.00), and a Nanometrics Titan 1g accelerometer (S0002.10). All of these sensors were operating in Princeton, New Jersey at the time of the September 9, 2020 $M_{Lg} = 3.1$ earthquake in Marlboro, New Jersey. We note that these responses have different, yet related shapes for different choices of output units. This is due to the fact that each of these response curves differ by a factor of $i\omega$, and thus correspond to successive rotations of the frequency response by $2\pi f$. Most broadband seismometers have a portion of their amplitude response that is flat in velocity, as can be seen for the Raspberry Shake 3D

and the Trillium Compact 120s (Figure 2.1c). The Titan 1g has a flat response to acceleration (Figure 2.1e).

It is important to keep in mind how gain and phase vary as a function of frequency, because this affects the outcome of the eventual instrument response removal by deconvolution or spectral division as we discuss next. However implemented, undoing the system response by converting a record from one of the Trillium Compact 120s seismometers to velocity amplifies the output at periods longer than 100 s (below 0.01 Hz), whereas performing the same operation on the Raspberry Shake 3D greatly amplifies the output at periods longer than 1 s (below 1 Hz). While the proper removal of the instrument response ensures that the frequency-dependent shape of the instrumental transfer function is accounted for, signal-to-noise considerations will dictate whether the original output at those periods can be trusted, or indeed, is of any interest.

These considerations illustrate the need for a judicious application of pre-filtering prior to instrument response removal. A pre-filter removing only periods longer than about 100 s might be fine for the Trillium Compact 120s, but would be an inappropriate choice for the Raspberry Shake 3D, which is not designed to record signals at such a long period.

2.5 SAC Implementation

Before continuing to our example of removing the instrument response, we briefly review the existing SAC algorithms which do so (Goldstein & Snoke 2005). As mentioned previously, the instrument response information typically comes as a `RESP` file or a `SAC_PZ` file. SAC provides functionality for removing either response specification using the `transfer` function, and although the results are nearly indistinguishable, there are minor differences in the algorithms that are worth commenting

on. The essential problem solved by both algorithms is: given poles, zeros, and gain, construct the transfer function, and deconvolve it from the seismogram of interest.

The main difference between the two algorithms is in the first step: the construction of the transfer function. When SAC `transfer` is called with a `RESP` file, it calls `evalresp`, an external C program, which constructs the transfer function with a length equal to that of the data vector. The call is restricted to returning a transfer function with no more than $2^{16} = 65,536$ points, and in the event that the data vector is longer, the transfer function is interpolated to match the length of the data vector . In contrast, when SAC removes the instrument response using a `SAC_PZ` file, it internally constructs the transfer function from the poles, zeros, and gain constant, with a length equal to that of the data vector rounded to the next power of 2, with no upper bound on the number of samples. After this, in both cases, the discrete Fourier transform of the zero-padded seismogram of interest is taken, the pre-filter is applied, and that frequency representation is divided by the (interpolated) frequency response function. SAC then takes an inverse discrete Fourier transform of the data to return to the time domain. The difference between these two methods is often subtle but sometimes noticeable.

2.6 Open-Source Implementation: `rflexa`

As a means of practically introducing these concepts to researchers and students of seismology, we have incorporated an instructional module as part of our `rflexa` software package. This module is available in both MATLAB and Python, to accommodate a wider range of programming backgrounds. The key elements of the module are: downloading seismic data and requesting and saving the instrument response information (in the `RESP` or `SAC_PZ` file format, or both), parsing the response to construct the transfer function, visualizing the transfer function, and removing the

transfer function (correcting for the instrument response). We hope that this will serve as a useful starting point for new and experienced students of seismology.

To briefly showcase some of rflexa's functionality, we examine data from the $M_{Lg} = 3.1$ earthquake in Marlboro, New Jersey (Figure 2.2). Four different instruments recorded this event in Princeton, New Jersey: a Raspberry Shake 3D, located roughly 5 m above ground level in university student housing (Figure 2.2a), and two Trillium Compact 120s seismometers and a Titan 1g accelerometer, all located in the basement of the Geosciences Department Guyot Hall (Figure 2.2b-c). The earthquake occurred roughly due east of Princeton, at an epicentral distance of 31.4 km, and the motion recorded on each instrument was of a similar order of magnitude, despite the different response characteristics of each sensor. To appropriately compare the records on each instrument, however, we ought to convert each record to a consistent physical unit (displacement, velocity, or acceleration). To obtain the results shown in Figure 2.3 we utilized the transfer function of the rflexa library, which was benchmarked against the SAC function of the same name (Figure 2.4).

To call transfer, we need a vector of equally spaced (preprocessed) data, their sampling interval, a vector of four frequencies that define the corners of a cosine filter applied to the data before deconvolving the instrument response, and three strings that specify: the desired output type, the path to the file containing the instrument response information, and a flag indicating whether that file is of type SAC_PZ or RESP. The function returns the appropriate ground motion. An example of the syntax used to call the function in MATLAB to produce the velocity records in Figure 2.3 is:

```
freqLims = [0.1, 0.2, 10, 20];
groundmotion = transfer(instrumentcounts,...
        deltat,freqLims,'velocity','pzFile','sacpz');
```

After successfully calling transfer and removing the instrument response from

the records shown in Figure 2.2, we observe that the shapes of the waveforms shown in Figure 2.3 are quite similar. One can even see coherent arrivals in the P wave coda on all 4 instruments. In addition, the amplitude of the velocity is roughly the same for each instrument. This example highlights the importance of correctly accounting for the instrument response as a preliminary step in the analysis of seismic data, as we can now compare all of our records consistently. With the ever increasing quantity and diversity of seismic instruments (Anthony et al. 2019, Simon et al. 2021), properly correcting for the instrument response remains as significant as ever.

In addition to providing functionality for removing the instrument response, `rflexa` provides a function which allows for the quick visualization of the instrument response contained in a `SAC_PZ` or `RESP` file. This function, `bodePlot`, which takes its name from the electrical engineering and control theory literature, takes two inputs, corresponding to the last two inputs to `transfer` defined above. An example of this function's syntax, by which we generated the panels in Figure 2.1, is:

```
bodePlot(pzFile,'sacpz');
```

We hope and expect that this function might prove useful as researchers consider the sensitivity of the instruments they are using before choosing pre-filtering corner frequencies. Both of these functions, and their dependencies, have analogous versions in Python. Also included are helper functions to save and parse `SAC_PZ` and `RESP` files in both languages.

2.7 The 2020 Marlboro Earthquake

Before concluding, it is worth commenting on the earthquake itself, given that seismicity is so uncommon in New Jersey and the northeast United States. Some authors have proposed that seismicity in the northeast may not be characterized by a Poissonian distribution (Ebel & Kafka 2002), suggesting that rare events such as this

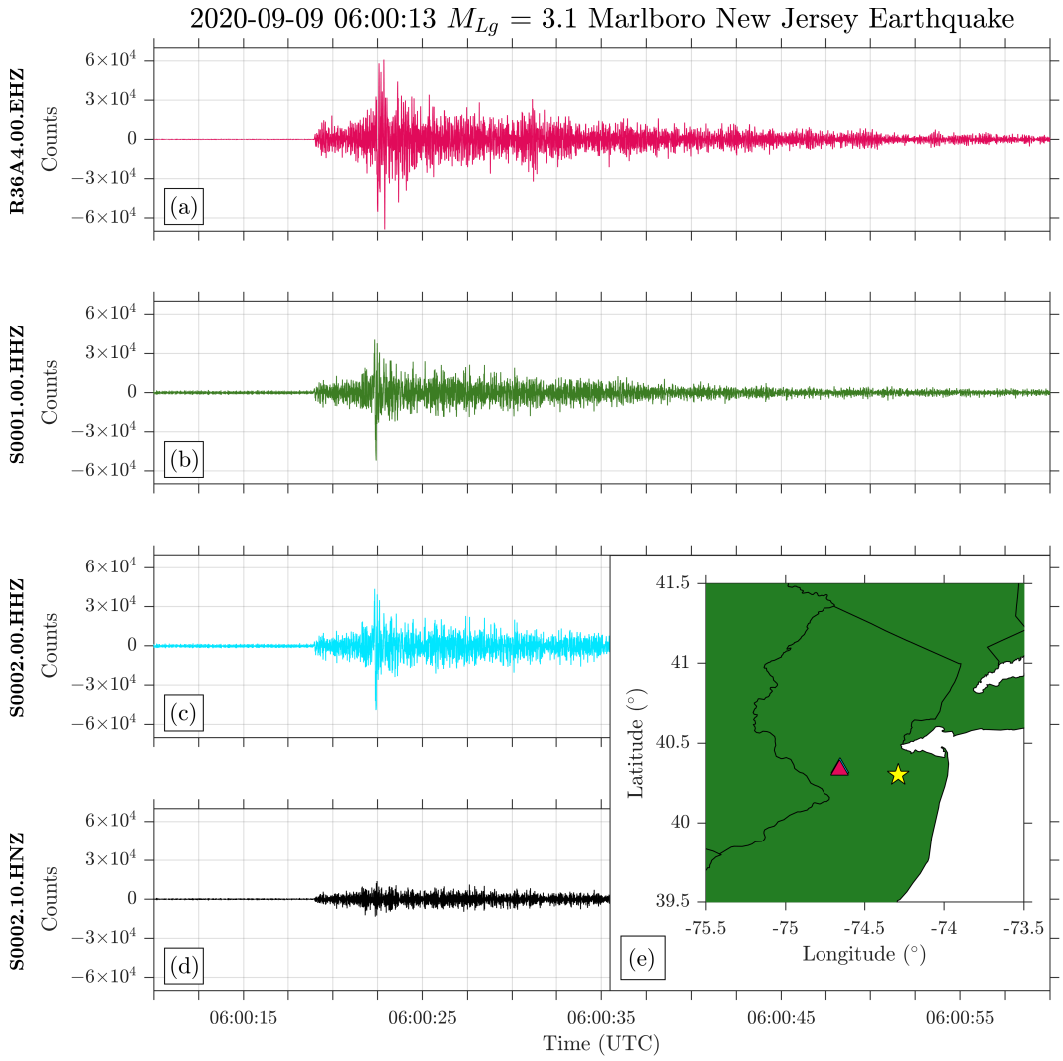


Figure 2.2: Unprocessed vertical-component records of the September 9, 2020 M_{Lg} 3.1 Marlboro, New Jersey earthquake from four different instruments: (a) a Raspberry Shake 3D, (b) a Trillium Compact 120s, (c) a Trillium Compact 120s (part of a Trillium Cascadia), and (d) a Titan 1g accelerometer (also part of the Trillium Cascadia), all located in Princeton, NJ. (e) The location of the instruments (triangles) relative to the earthquake (star). Note that all records are in digital counts. Instruments (b), (c), and (d), are located within 0.5 m of one another in the basement of a building on campus, and instrument (a) is located roughly 5 m above ground level in a two-story university student housing building. The USGS NEIC reported a location of 40.302°N 74.289°W, and a depth of 5.6 km for this event.

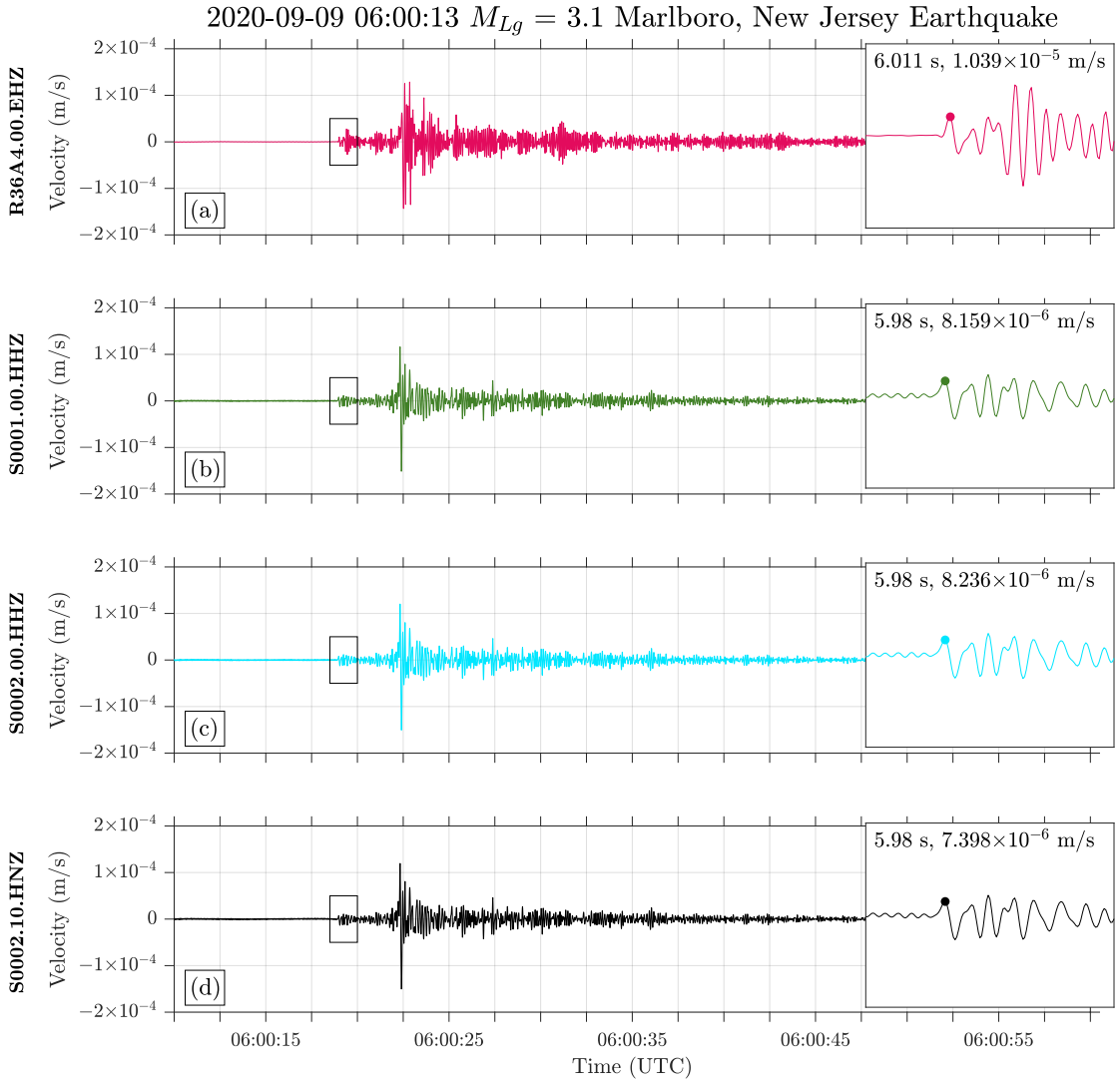


Figure 2.3: (a-d)The seismograms of Figure 2.2 after bandpass filtering between 0.2 and 10 Hz, and removing the instrument response to convert the records to velocity. Note that the amplitude of motion recorded on each instrument is approximately equal. The first motions, corresponding to the P wave arrival, recorded by each instrument are emphasized in the zoomed-in sections. Perhaps surprisingly, the Raspberry Shake 3D, in (a), has the least pre-event noise of all of the instruments shown. Annotations in the inset panels provide the arrival time and amplitude of the maximum of the first arriving pulse, marked by a filled circle.

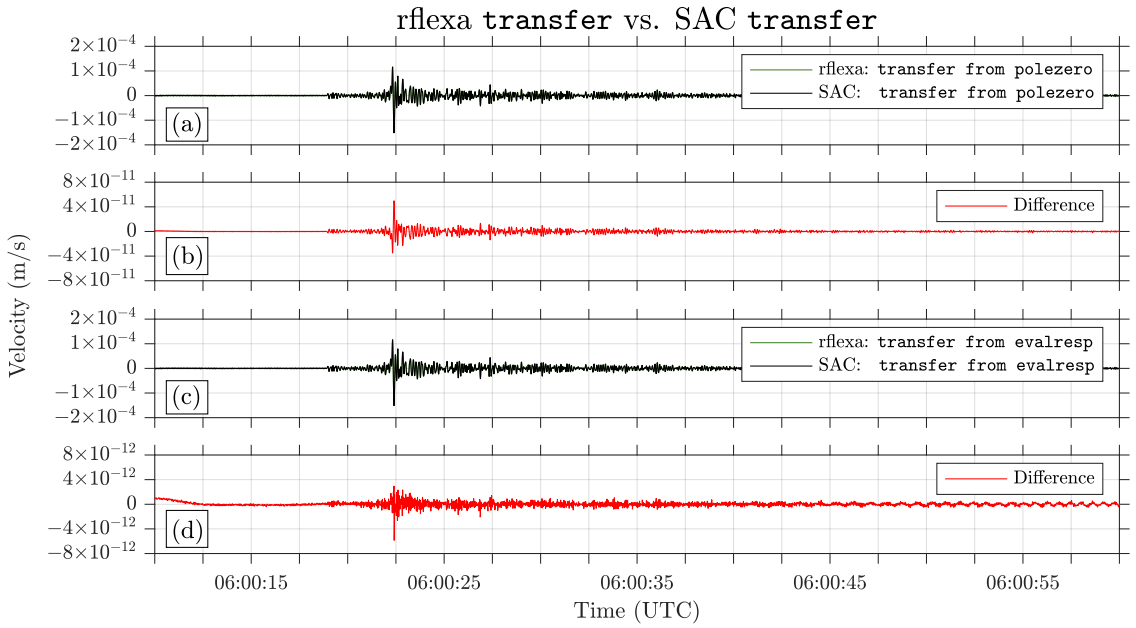


Figure 2.4: Comparison of instrument response removal methods. (a) Record after instrument response removal using the `transfer from polezero...` syntax in SAC, and the record converted using the analogous command in our open-source package, `rflexa`. (b) Difference (in red) between the two records in (a). (c) Records after instrument-response removal using the `transfer from evalresp...` syntax in SAC. (d) Difference (in red) between the two records in (c). The differences between the results are on the order of machine precision, verifying that the algorithms are benchmarked acceptably.

ought to be paid attention to as potential indicators of periods of enhanced seismicity. From a cultural perspective, this earthquake was reported as having been felt by over 7000 individuals and reported to the United States Geological Survey *Did You Feel It*? (Wald et al. 2012) service, which is unsurprising given the high population density of the New Jersey/New York metropolitan area. Geologically speaking, the earthquake occurred near the boundary of the Vincentown/Hornerstown Formation, of Paleocene age, and the Tinton/Red Bank Formation of upper Cretaceous age (Owens et al. 1995). Both of these units are composed of quartz sand, with the Vincentown/Hornerstown Formation additionally containing coquina and bryozoan reef deposits. The nearest mapped fault in the region is the Ramapo fault, which trends NE/SW approximately 50 km to the NW of the epicenter of the Marlboro earthquake. Scattered seismicity has occurred near this fault in recent times (Page et al. 1968), but the general pattern of seismicity in the greater New York City area does not, however, show clear concentration along the Ramapo or any other mapped fault (Kafka et al. 1985, 1989). Thus, the cause of the Marlboro earthquake remains enigmatic.

2.8 Conclusion

We have reviewed the physical motivation for, and some mathematical theory behind, the removal of the instrument response from digital seismic records. After outlining the practical details of acquiring and accounting for the instrument response, we discussed appropriate use-cases and considerations. We then presented open-source routines in MATLAB and Python which perform the instrument response removal and provided functions for visualizing transfer functions. Lastly, we presented examples from four different instruments of records of the $M_{Lg} = 3.1$ Marlboro, New Jersey earthquake as a concrete illustration of instrument response removal in practice—for a

rare earthquake in our home state. The interested reader can find the code, tutorials, animations, and instructional modules at: `https://github.com/alexburky/rflexa/tree/master/transfer`.

2.9 Data and Resources

Seismograms used in this study were recorded using instruments on or near Princeton University, and are available with their corresponding instrument response data at: `https://github.com/alexburky/rflexa/tree/master/transfer/data`. In addition, the Raspberry Shake 3D data are available for download online from the IRIS Data Management Center at www.iris.edu. We have also made use of the SAC software package, which can be requested at `http://ds.iris.edu/ds/nodes/dmc/forms/sac/`, and Matlab version R2020b which can be accessed at `http://www.mathworks.com/products/matlab`. All websites were last accessed in July 2021.

2.10 Acknowledgments

We would like to thank the Incorporated Research Institutions for Seismology (IRIS) for providing the SAC software package (and its source code) to use as a reference for benchmarking our codes. Partial support for this work was provided by NSF under grant EAR-1736046. We thank Lucas Sawade for providing access to the Raspberry Shake 3D data, and we thank the Princeton Department of Geosciences, the High Meadows Environmental Institute, and the Freshman Seminar Program for acquiring the instrumentation. We are grateful to Alan Kafka for contributing his insight and Adam Ringler for a detailed and constructive review.

Chapter 3

Mantle transition zone receiver functions for Bermuda: automation, quality control, and interpretation*

3.1 Abstract

The origin of the Bermuda rise remains ambiguous, despite, or perhaps because of, the existence of sometimes incongruous seismic wave-speed and discontinuity models in the sub-Bermudian mantle. Hence, whether Bermuda is the surface manifestation of a mantle plume remains in question. Using the largest data set of seismic records from Bermuda to date, we estimate radial receiver functions at the Global Seismographic Network (GSN) station BBSR in multiple frequency bands, using iterative time-domain deconvolution. Motivated by synthetic experiments using axisymmetric spectral-element forward waveform modeling, we devise a quality metric for our receiver functions to aid in the automation and reproduction of mantle transition zone discontinuity studies. We interpret the complex signals we observe by considering the

*This chapter was published with the citation **Burky, A. L.**, Irving, J. C. E., & Simons, F. J. (2021). Mantle transition zone receiver functions for Bermuda: automation, quality control, and interpretation. *J. Geophys. Res. Solid Earth*, 126, e2020JB020177, doi: 10.1029/2020JB020177.

mineralogical controls on mantle transition zone discontinuity structure, and conclude that our results are likely to be indicative of a thicker than average mantle transition zone. Our result is incompatible with the canonical model of a whole mantle plume in an olivine dominated mantle; however, considerations of phase transitions in the garnet system would allow us to reconcile our observations with the possible presence of a through-going hot thermal anomaly beneath Bermuda.

3.2 Introduction

Intraplate, or hot-spot, volcanism is typically interpreted as the result of plate motion over a spatially localized region of long-lived deep-mantle upwelling (Morgan 1971). Arguably the most famous example of this process is the Hawaiian-Emperor Seamount Chain (e.g Steinberger et al. 2004). Whether Bermuda belongs in this category of an intraplate volcano originating from a deep-mantle plume source remains uncertain. The island of Bermuda, situated atop a roughly 10^6 km^2 bathymetric swell in the Western Atlantic Ocean (Figure 3.1) lacks an age-progressive seamount chain and present-day active volcanism. Radiometric dating of borehole samples from the island and adjacent swell area revealed that the volcanic pedestal was formed during the Middle Eocene (ca. 48–45 Ma), and reached subaerial extent in the Late Eocene, approximately 40–36 Ma (Vogt & Jung 2007). The pedestal has remained volcanically dormant since, and is now overlain by a fossiliferous carbonate platform. In spite of these facts, which suggest an isolated volcanic episode leading to Bermuda's formation, the region is included in some plume-hot-spot catalogs (Sleep 1990, King & Adam 2014), though it fails to meet others' definitions of a mantle plume (Courtillot et al. 2003) due to its lack of a hotspot track and weak evidence for a significant upper mantle low velocity anomaly from seismic tomography. Additionally, several studies suggest a link between the igneous activity which formed Bermuda and other

volcanic events, such as the formation of the Mississippi Embayment (Cox & Van Arsdale 2002, Liu et al. 2017) and the reactivation of the New Madrid rift system (Chu et al. 2013), though it may not be linked to all the magmatism along its purported track (Mazza et al. 2014).

Recent work in whole mantle seismic tomographic imaging has facilitated the observation and interpretation of several of these deep-mantle plume structures (e.g. French & Romanowicz 2015), particularly in association with the Pacific and African LLSVPs (Lekić et al. 2012). The presence of a strong, high temperature mantle upwelling should be visible in tomographic images of mantle velocity. To explore this hypothesis in the context of Bermuda, we made cross sections through two seismic tomography models (Figure 3.2), the joint P and S velocity model LLNL_G3D_JPS (Simmons et al. 2015) and the radially anisotropic S velocity model SEMUCB_WM1 (French & Romanowicz 2014). Both models display a low velocity anomaly beneath Bermuda relative to the one-dimensional (1-D) average velocity of the profile interrogated. This anomaly extends as a continuous feature to roughly 1500 km depth, and then is deflected eastward (Figure 3.2b,c) by what appears to be the relict Farallon slab (Sigloch et al. 2008). In addition to a broad low velocity anomaly, both models show a localized low velocity anomaly of varying depth extent directly beneath Bermuda. This feature is observed most clearly in the North-South cross section through model LLNL_G3D_JPS (Figure 3.2e, directly beneath the central gray circle), and motivates our investigation. In model SEMUCB_WM1 this feature is pronounced at depths shallower than 410 km, and is faintly continuous through the mantle transition zone where it reaches maximum amplitude near 1000 km depth (Figure 3.2f).

This chapter has two objectives: (1) to assess the validity of the plume-hot-spot hypothesis for Bermuda using seismological techniques, specifically, by (2) developing a robust method to do so on a small (single-station) and noisy (island) data set.

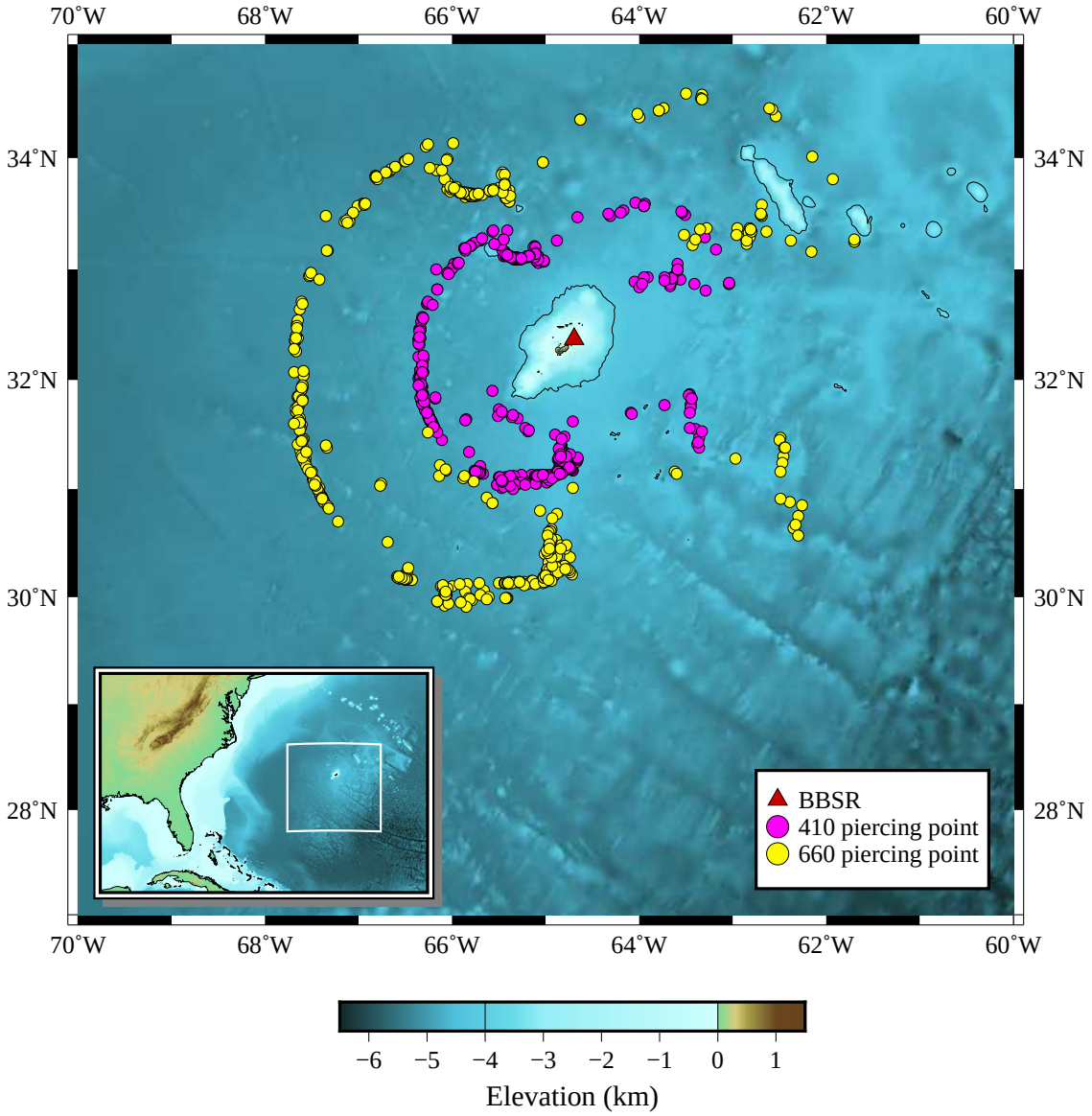


Figure 3.1: Bathymetry (Becker et al. 2009) of the study region, showing the location of Global Seismographic Network (GSN) station BBSR, and incoming *P410s* and *P660s* piercing points from the 226 earthquakes with high enough quality to be used in our receiver-function analysis. The bathymetric swell is roughly outlined by the 4 km depth contour. Note the absence of a well defined hotspot track, which would be expected to trend East-West.

In this chapter, we investigate the topography of the 410 km and 660 km mantle discontinuities beneath Bermuda.

The mantle transition zone plays an important role in determining and revealing the behavior of mantle flow, and the topography of the seismic wave-speed discontinuities, at the nominal depths of 410 km and 660 km (hereafter referred to as 'the 410' and 'the 660'), provides a proxy for the thermal and compositional state beneath a region (e.g. Helffrich & Wood 2001). The 410 is understood to be controlled by the olivine to wadsleyite phase transition, an exothermic reaction at relevant pressure (P) and temperature (T) conditions, whose Clapeyron slope, dP/dT, is positive (Bina & Helffrich 1994). The 660 is more complicated (Vacher et al. 1998, Simmons & Gurrola 2000), due to the negative Clapeyron slope of the endothermic ringwoodite to bridgmanite and magnesiowüstite (ferropericlase) phase transition (Ito et al. 1990), and the positive Clapeyron slope of the exothermic majorite garnet to perovskite phase transition (Hirose 2002). A 'cold' mantle transition zone (e.g. one influenced by subduction) is expected to be thick. A 'hot' mantle transition zone may have one of two different expressions: if it is a garnet-dominated system one would expect simultaneous depression of both discontinuities (e.g. Jenkins et al. 2016). Alternatively, the more commonly expected situation is that a hot, olivine-dominated system should exhibit a thin transition zone, with a depressed 410 and an elevated 660 (Bina & Helffrich 1994).

In order to characterize the 410 and 660 beneath Bermuda, we calculate radial receiver functions (Phinney 1964, Vinnik 1977, Langston 1979, Ammon 1991, Ligorría & Ammon 1999) using earthquake data recorded on Global Seismographic Network (GSN) station BBSR. Using radial receiver functions calculated with the iterative time-domain deconvolution algorithm, Benoit et al. (2013) measured a 215 km thick mantle transition zone beneath BBSR. These authors then used the global average transition zone thickness of 242 km (Lawrence & Shearer 2006) in conjunction with phase transition information to calculate the thermal anomaly implied by their measurement, arriving at a result of 172 to 320 K hotter than the reference model. In

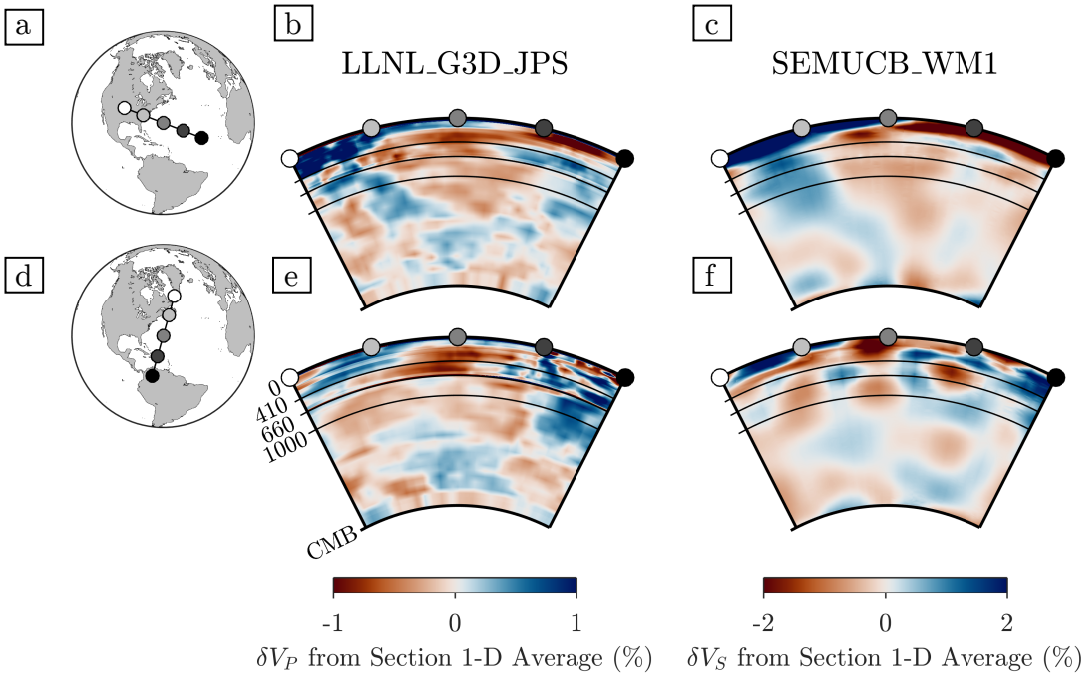


Figure 3.2: Cross sections centered on Bermuda through whole mantle tomography (b,e) V_P component of model LLNL_G3D_JPS (Simmons et al. 2015) and (c,f) V_S model SEMUCB_WM1 (French & Romanowicz 2014). Wave speed perturbations are shown relative to the one-dimensional (1-D) average velocity profile for the region shown in the cross section. Note the consistently imaged low seismic velocity anomaly extending through the mantle transition zone, but not necessarily through the entire mantle, beneath Bermuda. The anomaly is particularly apparent in the North-South cross sections (e and f).

addition, their analysis of shear wave splitting revealed an isotropic (null splitting) upper mantle beneath Bermuda, which they interpreted as indicative of vertically upwelling mantle flow beneath the island. Another well documented study of the transition zone structure beneath Bermuda was performed by Gao & Liu (2014) as part of a larger investigation of the transition zone structure beneath the contiguous United States. Unlike Benoit et al. (2013), this study used a frequency-domain approach to calculate radial receiver functions for both *Pds* and *PPds* phases. Despite these differences, their study reaffirmed the results of Benoit et al. (2013), reporting a transition-zone thickness some 16 km thinner than the 250 km thickness of IASP91 (Kennett & Engdahl 1991), mainly due to a depression of the 410 km discontinuity down towards ∼440 km. In contrast to these two studies, Tauzin et al. (2008), using radial receiver functions calculated with the iterative time-domain deconvolution algorithm, found no notable thinning of the mantle transition zone under Bermuda. Instead, they reported a normal mantle transition zone thickness, albeit one with both the 410 and 660 deeper than the average at the stations they investigated. A key difference in the processing of each of these studies is their application of filtering; Benoit et al. (2013) performed no pre-filtering, Gao & Liu (2014) filtered all records between 5–50 s, and Tauzin et al. (2008) filtered all records between 10–25 s.

We build on these studies by including more recent waveform data, introducing a quantitative metric for classifying the quality of individual receiver functions, and by exploring the effects of different filtering parameters on the resulting receiver functions. Our methodology therefore lends itself to providing a reproducible benchmark for future studies.

3.3 Data and Methods

We use teleseismic earthquake data from station BBSR in the Global Seismographic Network (network code IU). Several instruments have been operated at this station since its opening; we use the broadband channels (BH) with location ID 00. We requested seismograms from events with moment magnitudes $M_w > 5.5$ that occurred within an epicentral distance range of 30°–90° from the station between August 2002 and November 2019 resulting in 1,866 event records. We removed the appropriate instrument response from each seismogram, converting from digital counts to three-component displacement.

We are interested in isolating the conversions, due to impedance contrasts in the upper mantle beneath our station, of compressional wave energy into vertically polarized shear-wave energy. The three-component displacement record is

$$\mathbf{u}(t) = [u_Z(t) \quad u_N(t) \quad u_E(t)]^{\mathrm{T}}, \tag{3.1}$$

where the subscripts Z, N and E refer to the vertical (up), north, and east components of motion in the local Cartesian coordinate system centered on the station. The particle motion of the P wave, and of the vertically (SV) and horizontally (SH) polarized shear waves is best expressed in a Cartesian coordinate frame relative to the seismic ray. We rotate the station components into the ray plane via the matrix transformation:

$$\begin{bmatrix} u_R(t) \\ u_T(t) \end{bmatrix} = \begin{bmatrix} \cos\theta & \sin\theta \\ -\sin\theta & \cos\theta \end{bmatrix} \begin{bmatrix} u_N(t) \\ u_E(t) \end{bmatrix}, \tag{3.2}$$

where $u_R(t)$ and $u_T(t)$ are now referred to as the radial and tangential displacement components, respectively, and θ is the azimuth at the station: the angle, measured clockwise from north at the station, to the extended great-circle arc directed from the earthquake epicenter to the recording station. The radial component of motion at the

station is positive when directed away from the earthquake hypocenter. For the steep angles of incidence of teleseismic events, we make the assumption that $u_Z(t)$ contains the most important record of the P-wave motion and that $u_R(t)$ is most indicative of the SV-wave signal.

The final steps in our preprocessing are filtering and windowing (tapering) of the rotated seismograms. We analyze our results with no pre-filtering, and compare them to results using zero-phase filtering, utilizing a fourth-order, two-pass Butterworth filter with corner frequencies of 0.02 and 1 Hz, or 1–50 s period, respectively. Subsequently, we window the data around the calculated theoretical P arrival time in the IASP91 velocity model (Kennett & Engdahl 1991), with the `TauP-Toolkit` (Crotwell et al. 1999), retaining data 30 s prior to and 90 s after this predicted time. We taper the seismograms using a Tukey window with cosine fraction 0.25. Examples of the resulting waveforms are shown in Figure 3.3, ready for use in studying the conversion of $u_Z(t)$ into $u_R(t)$ motion, or alternatively, of P into SVenergy. For clarity and to aid in reproducing our results, we briefly summarize the theoretical basis for the Ligorría & Ammon (1999) analysis method that we employ.

3.3.1 Receiver Functions

Our modeling stipulates that the conversion between compressional (vertical-component) and vertically-polarized shear (radial-component) motion is a linear time-invariant system (Bendat & Piersol 2000), characterized by a convolutional ($*$) response, $f_{Z\to R}(t)$,

$$u_R(t) = (u_Z * f_{Z\to R})(t) = \int_{-\infty}^{\infty} u_Z(\tau)\, f_{Z\to R}(t-\tau)\, d\tau. \tag{3.3}$$

It is this response which we seek to determine and subsequently study as it relates to Earth structure. In the spectral domain, after forward Fourier transformation $\mathcal{F}$,

$$\widetilde{u}_R(\omega) = \widetilde{u}_Z(\omega)\, \widetilde{f}_{Z\to R}(\omega), \quad \text{where} \quad \mathcal{F}(u) = \widetilde{u} \quad \text{and} \quad \mathcal{F}(f_{Z\to R}) = \widetilde{f}_{Z\to R}, \tag{3.4}$$

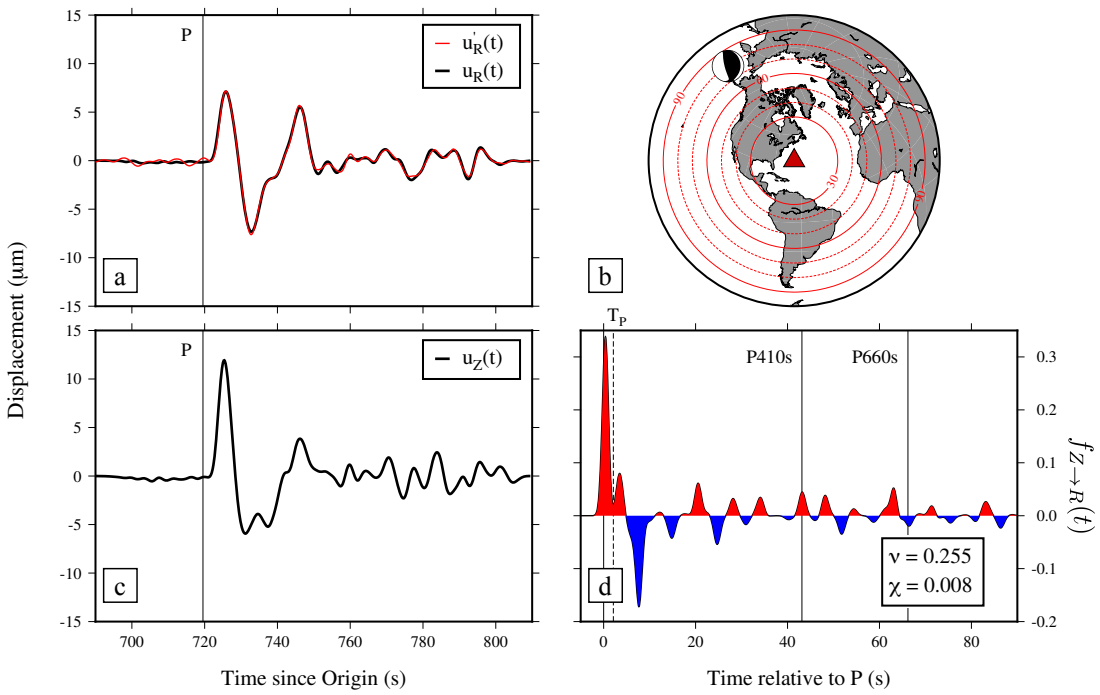


Figure 3.3: (a) Unfiltered radial and predicted radial (u_R and u'_R) and (c) vertical (u_Z) component displacement seismograms recorded in Bermuda for the June 14, 2005 M_W=6.8 earthquake at 53.9 km depth (C200506141710A). The vertical line shows the predicted P arrival time according to 1-D velocity model IASP91. (b) Map showing the event with its corresponding Global CMT focal mechanism (Ekström et al. 2012) solution. The red circles indicate different epicentral distances from BBSR. (d) Radial receiver function computed for this event using a Gaussian width factor $\tilde{\sigma} = 1.0$ Hz (see main text). The model quality factor, ν, and data misfit, χ, as discussed in the text, are included for reference.

and ω is the angular temporal frequency. Thus, in theory, the frequency-domain representation of the receiver function is recoverable by forming the ratio

$$\widetilde{f}_{Z\to R}(\omega) = \frac{\widetilde{u}_R(\omega)}{\widetilde{u}_Z(\omega)}. \tag{3.5}$$

As written, eq. (3.5) is a solution without a practical method for achieving it (Langston 1979). Of the many algorithms that have been developed to stably obtain an estimate of $f_{Z\to R}(\omega)$ from noisy, windowed, sampled data, we choose the iterative time-domain deconvolution approach of Ligorría & Ammon (1999), as detailed in the next section.

3.3.2 Iterative Time-Domain Deconvolution

Although the theoretical basis for the iterative time-domain deconvolution is in fact in the time-domain, algorithmic implementations, to our knowledge, very often rely on frequency domain operations. Here, we present a description of the algorithm as it operates in practice. In the following description, it is implied that characters with a tilde (e.g. $\widetilde{u}_R$) represent the discrete Fourier transform of time domain entities.

Contrary to the idealized scenario described in the previous section, the structural signal that we wish to recover from real seismic data is contaminated with noise. Therefore, in the discrete domain of noisily observed data, we model the system as

$$\widetilde{u}_R(\omega) = \widetilde{u}_Z(\omega)\,\widetilde{f}_{Z\to R}(\omega) + \widetilde{n}(\omega), \tag{3.6}$$

a version of eq. (3.4) contaminated by additive noise, $\widetilde{n}(\omega)$, about which we make the minimal assumption that it is uncorrelated and incoherent with the signal, such that:

$$\langle \widetilde{u}_Z(\omega)\widetilde{f}_{Z\to R}(\omega)\,\widetilde{n}^*(\omega)\rangle = 0, \tag{3.7}$$

where the angular brackets denote ensemble averaging and the star is used for the complex conjugate. Hence, from eqs (3.6)–(3.7), the system response, the theoretical quantity that we seek to recover, is then given by

$$\widetilde{f}_{Z\to R}(\omega) = \frac{\langle \widetilde{u}_R(\omega)\,\widetilde{u}_Z^*(\omega)\rangle}{\langle \widetilde{u}_Z(\omega)\,\widetilde{u}_Z^*(\omega)\rangle}. \tag{3.8}$$

We reformulate the problem as one in which we wish to find, using a prime to denote an *estimate*, the $\widetilde{f}'_{Z\to R}$ (or, in the time domain, $f'_{Z\to R}$) that, when multiplied (or convolved) with the observed vertical-component seismogram, $\widetilde{u}_Z$ (or u_Z), produces an approximation to the radial component $\widetilde{u}'_R$ (or u'_R) that is sufficiently close to the

observed $\widetilde{u}_R$ (or u_R). The residual is denoted

$$\Delta\widetilde{u}_R = \widetilde{u}_R - \widetilde{u}'_R. \tag{3.9}$$

Ligorría & Ammon (1999) formulated the time-domain solution iteratively as follows. We denote the iterates with a superscript, $\widetilde{u}'^{(j)}_R$, $\Delta\widetilde{u}^{(j)}_R$, and $f'^{(j)}_{Z\to R}(t)$, and initialize the process at iteration $j = 0$ using

$$\begin{cases} \widetilde{u}'^{(0)}_R(\omega) & = 0, \\ \Delta\widetilde{u}^{(0)}_R(\omega) & = \widetilde{u}_R(\omega), \\ f'^{(0)}_{Z\to R}(t) & = 0. \end{cases} \tag{3.10}$$

Writing Δt for the time interval of the discretized sampling sequence of observations $n = 0, \ldots, N-1$, and introducing the notation

$$\|u_Z\|_2^2 = \Delta t \sum_{n=0}^{N-1} [u_Z(n\Delta t)]^2, \tag{3.11}$$

we proceed to determining, for iteration $j > 0$, the auxiliary quantities

$$\begin{cases} f_j(t) & = \mathcal{F}^{-1}\left\{\Delta\widetilde{u}^{(j-1)}_R(\omega)\,\widetilde{u}^*_Z(\omega)\,/\|u_Z\|_2^2\right\}, \\ t_j & = \arg\max\{f_j(t)\}, \\ F_j & = \max\{f_j(t)\}, \end{cases} \tag{3.12}$$

which we use to determine the jth receiver-function estimate as a train of Gaussians,

$$f'^{(j)}_{Z\to R}(t) = f'^{(j-1)}_{Z\to R}(t) + F_j\,\sigma\sqrt{2\pi}\,g(t; t_j, \sigma^2), \tag{3.13}$$

where $g(t; t_j, \sigma^2)$ is a Gaussian density function with an expectation t_j, as constrained by the data via eq. (3.12), and with a variance, σ^2, predetermined based upon band-

width considerations at the onset, and held constant throughout the procedure. As defined here, σ is the time-domain version of what we call the "Gaussian width factor", which has as its frequency-domain counterpart,

$$\tilde{\sigma} = 1/\sigma, \qquad \text{the "Gaussian width factor"}. \tag{3.14}$$

We recognize $f_j(t)$ in eq. (3.12) as a time-domain equivalent of eq. (3.8), without the averaging brackets, and replacing the effect of the denominator, via Parseval's theorem, by the mean-squared energy $\|u_Z\|_2^2$ computed in the time-domain as introduced in eq. (3.11). The expression (3.13) matches the maximum amplitude, F_j, of the intermediate quantity $f_j(t)$ at the location of its peak, t_j.

The evolving receiver-function estimate $f'^{(j)}_{Z\to R}(t)$ is applied to the unchanged vertical-component data $u_Z(t)$ by frequency-domain multiplication to form the evolving radial-component prediction. This prediction is then transformed back into the time domain and subtracted from the original data $u_R(t)$ to define the updated residual

$$\Delta u_R^{(j)}(n\Delta t) = u_R(t) - \mathcal{F}^{-1}\left\{\widetilde{f}'^{(j)}_{Z\to R}(\omega)u_Z(\omega)\right\}, \tag{3.15}$$

which re-enters equation (3.12) at each iteration.

As the iterations proceed, we monitor the quality of the fit via the fractional energy of the residual in (3.15), compared to the observed radial-component displacement record, again in the time-domain, as

$$\chi_j = \frac{\sum_{n=0}^{N-1}[\Delta u_R^{(j)}(n\Delta t)]^2}{\sum_{n=0}^{N-1}[u_R(n\Delta t)]^2}. \tag{3.16}$$

We iterate over eqs (3.12)–(3.15), counting $j = 1, ..., J$, until the change of misfit χ_j

in subsequent iterations is smaller than some predefined tolerance,

$$\Delta\chi_j = \chi_j - \chi_{j-1} < \varepsilon. \tag{3.17}$$

We use a value of $\varepsilon = 10^{-5}$, and impose the additional constraint that the total number of iterations be limited to $J \leq 1,000$. See Figure 3.3 for an illustration summarizing the algorithm.

The time-domain receiver-function estimate is $f'^{(J)}_{Z\to R}$, or $f'_{Z\to R}$, for short, and its associated data misfit is χ_J, or simply χ in what follows.

3.3.3 Automating Receiver Function Quality Control

Now that we have fully documented our method for producing receiver functions, we describe our methods for assessing their quality for our primary objective of resolving the discontinuity structure of the mantle transition zone beneath our station. Although χ, the fractional residual at the final iteration, quantifies the quality of a receiver function $f'_{Z\to R}$ in its performance solving eq. (3.6) for the unknown true $f_{Z\to R}$, it provides neither insight nor control on the quality of the seismograms fed into the deconvolution algorithm (for this, see also Yang et al. 2016), nor does it factor in any prior notion of what a "good" receiver function should resemble. To account for these considerations, we impose three quality control criteria: one on the input seismograms, and two on the output receiver functions.

The first measure of quality, imposed on the input seismograms, is the signal-to-noise ratio (SNR) of $u_Z(t)$ and $u_R(t)$. We use the method outlined in Gao & Liu (2014), where the SNR is defined as $\max|A_s|/|\bar{A}_n|$, where $\max|A_s|$ is the maximum absolute value of the record over the interval ranging from 8 s before to 12 s after the predicted arrival time of P in the IASP91 model, and $|\bar{A}_n|$ is the mean absolute

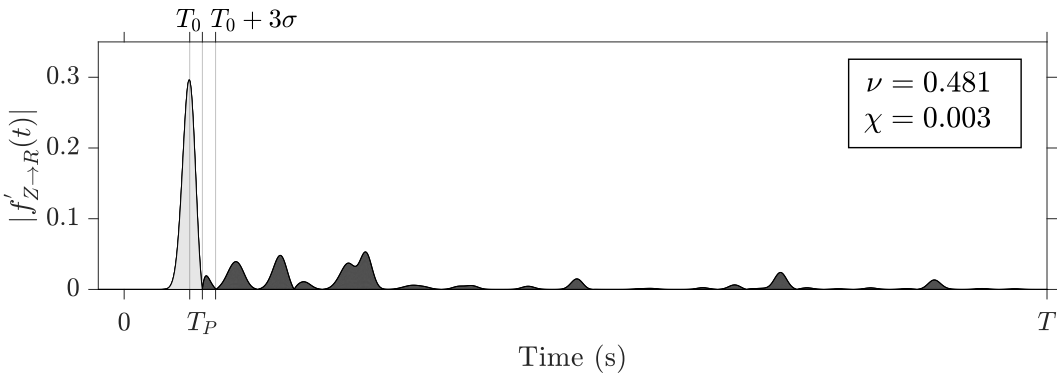


Figure 3.4: Illustration of our quality control metric, ν, on a synthetic receiver function made in model IASP91 using AxiSEM. Synthetics were calculated for a $M_w = 6.0$ event, at 20 km depth. The receiver function shown corresponds to the recorded displacement 52° away from our synthetic event. The metric weights the main P arrival relative to the P wave coda. The Gaussian width $\tilde{\sigma} = 1.0$ Hz, and the length of the window considered, $T = 120$ s. The light gray shaded area corresponds to the numerator in eq. (3.18).

value of the record between 20 and 10 s before the predicted P arrival time. We only accept input data with SNR ≥ 4.

The second measure of quality, and the first imposed on the receiver functions themselves, is on the data misfit χ (eq. 3.16). We accept receiver functions which yield a final value of $\chi \leq 0.2$, or equivalently, where convolution of the u_Z data with the receiver function estimate $f'_{Z\to R}$ produces a final fit to the u_R data that is 80% or greater in terms of energy.

Our third and final measure of quality is a metric designed to quantify the shape or distribution of information within the receiver function. Forward modeling experiments that we conducted using 1-D reference model IASP91 with the spectral-element wave-propagation code AxiSEM (Nissen-Meyer et al. 2014) showed that a "good" receiver function produced using the Ligorría & Ammon (1999) algorithm described in the previous section will display its largest amplitude spike at time zero, corresponding to the incident P wave arrival. Subsequent spikes have smaller amplitudes, representing the longitudinal-to-shear *Pds* phases converted at discontinuities at depths d km, and their surface and internal reverberations. Significant departures from this char-

acteristic shape or figure-of-merit can be caused by noisy input records and phases interfering in the P wave coda, such as the surface reflection PP at epicentral distances smaller than 35° and the core-reflected phase PcP in the epicentral distance range 50°–60°. It is therefore reasonable to demand that a "good" receiver function show a large Gaussian pulse due to the incident P wave arrival, compared to any other subsequent Gaussian pulses in the receiver-function coda. These considerations motivate us to define a quality control metric as

$$\nu \equiv \frac{\int_0^{T_P} f'_{Z\to R}(t)\,dt}{\int_0^{T} |f'_{Z\to R}(t)|\,dt}, \qquad \nu \in [-1,1], \tag{3.18}$$

where T is the length of the entire time window under consideration, and T_P is defined as the smallest of the set of times t whereby the receiver function or its first derivative vanish, within a restricted window of length 3σ after T_0, at which the receiver function $f'_{Z\to R}(t)$ reaches its maximum value due to the incident P wave,

$$T_P = \min\left[\left\{t : f'_{Z\to R}(t) = 0\right\}, \left\{t : \frac{df'_{Z\to R}(t)}{dt} = 0\right\}\right] \quad \text{for} \quad t \in [T_0, T_0 + 3\sigma]\,, \tag{3.19}$$

where $\sigma = \tilde{\sigma}^{-1}$ is the temporal Gaussian width factor defined in eq. (3.14). By this definition we effectively isolate the earliest major pulse in the receiver function. See Figure 3.4 for an illustration. Large values of ν correspond to "good" receiver functions while small values of ν correspond to receiver functions with "ringy" P wave codas.

We note that this criterion might be unhelpful in those cases where the presence of a low-velocity layer or complex crustal structure causes receiver functions to be very oscillatory (Zelt & Ellis 1999, Yu et al. 2015). In such cases, we suggest that the distribution of ν values may reflect the presence of such structure. At present, we believe this metric, as used in this chapter, is best suited for studying mantle transition zone

structure beneath stations installed on bedrock. Further investigation of its characteristics in a variety of geologic environments will help to develop an understanding of its strengths and limitations in aiding receiver function studies of the subsurface. Finally, we emphasize that in addition to effectively filtering "bad" receiver functions from our dataset, our metric ν provides an easily implementable, reproducible, and objective measure of receiver function quality which can be incorporated into a data analysis workflow.

We are certainly not the first group to attempt to automate the calculation of receiver functions, and those interested in the subject are likely familiar with the existing EARS product (Crotwell & Owens 2005), which performs automated analysis of crustal structure using receiver functions. The key difference between our method and EARS is that they limit their quality control criterion to a SNR consideration and a deconvolution fit consideration. In addition, since they are interested in investigating the crust they use a higher value of $\tilde{\sigma} = 2.5$ for their Gaussian width factor. Our method allows for a similar automation procedure for mantle transition zone receiver functions, but also improves upon it by introducing an additional measure on the quality of individual receiver functions, ν.

3.3.4 Time-to-Depth Conversion

The final step in our workflow involves the conversion of the obtained receiver functions from the time domain into the depth domain. In order to achieve this mapping, we must assume a velocity model which allows us to associate times of specific pulses in our receiver functions with *Pds* conversion depths d, thereby also correcting for the temporal moveout of the *Pds* phases due to the spread of event-station distances in our data (Kind & Vinnik 1988, Gurrola et al. 1994). For a 1-D Earth model, following Chevrot et al. (1999) and others, the conversion is performed using the approximate

expression

$$t_{Pds}(p,z) = \int_0^Z \left[\sqrt{V_S^{-2}(z) - p^2 r^{-2}} - \sqrt{V_P^{-2}(z) - p^2 r^{-2}} \right] dz, \tag{3.20}$$

where p represents the P wave ray parameter (s/km) of the receiver function being converted, $r \in [0,1]$ is the normalized Earth radius for a candidate discontinuity at a particular depth Z, and $V_P(z)$ and $V_S(z)$ are the P and S wave speed profiles as a function of depth, z. The integral in Eq. (3.20) is computed at $\Delta z = 1$ km intervals in depth from 0 to 800 km to map time t to Pds conversion depth Z. We work with the 1-D velocity model IASP91, so as to provide a more direct comparison of our results to those of Gao & Liu (2014). Once these moveout times were calculated, we depth-converted and stacked all of our accepted receiver functions in the following manner (Liu & Gao 2006),

$$\bar{f}_{Z\to R}(p,z) = \frac{1}{M} \sum_{m=1}^{M} f'^{m}_{Z\to R}\left(t^m_{Pds}[p,z]\right), \tag{3.21}$$

where $\bar{f}_{Z\to R}(p,z)$ is the amplitude of the stack as a function of depth z and ray parameter p, M is the number of receiver functions, $t^m_{Pds}[p,z]$ is the moveout time for the mth receiver function as a function of depth, z, for the ray parameter p corresponding to the given event, and $f'^{m}_{Z\to R}\left(t^m_{Pds}[p,z]\right)$ is the amplitude of the mth receiver function at time $t^m_{Pds}[p,z]$, the moveout time calculated in eq. (3.20).

In addition to depth converting receiver functions using the 1-D velocity model IASP91, we performed 3-D depth corrections using the joint P and S velocity model LLNL_G3D_JPS. To do this, we ray traced individual paths through the model for each of our selected events. Using the P and S velocity profiles calculated for each path, we solved eq. (3.20) to associate times with conversion depths in each receiver function. We subsequently stacked these receiver functions using eq. (3.21).

To estimate standard deviations for our stacked receiver functions, we applied

the bootstrap resampling procedure (Efron & Tibshirani 1986), where stacks are generated using a random subset of the receiver-function data. This resampling was carried out 1000 times.

Finally, to establish confidence in our methodology and to build an intuition for our ability to resolve the mantle transition zone discontinuities, we applied our methods to a set of 2 Hz synthetic data. We calculated synthetics using the web-based Syngine tool (van Driel et al. 2015), using the event depths, locations, and CMT solutions of our dataset. The results of this experiment gave us confidence that our method worked, and can be found in supplementary Figure S1.

3.4 Results

We are now equipped to begin viewing the mantle transition zone discontinuity structure beneath Bermuda through the lens outlined above. Our observations are directly influenced by the choices of parameters we use to construct them; therefore, we systematically catalog the behavior of our observations as functions of these parameters. First, we compare the performance of our automated quality control metric, ν, to a control experiment conducted manually. We then explore the influence of interference from the surface reflected phase *PP* on our receiver function data. Third, and finally, we investigate the behavior of our results as a function of the pre-filtering applied to the seismograms. This analysis elucidates some of the nuances of the receiver function method in general, and additionally informs us about the nature of the mantle transition zone beneath Bermuda.

3.4.1 Comparison of Manual and Automated Data Selection

To benchmark our automated quality control metric against a hand-picked receiver function workflow, we manually selected high quality receiver functions from our

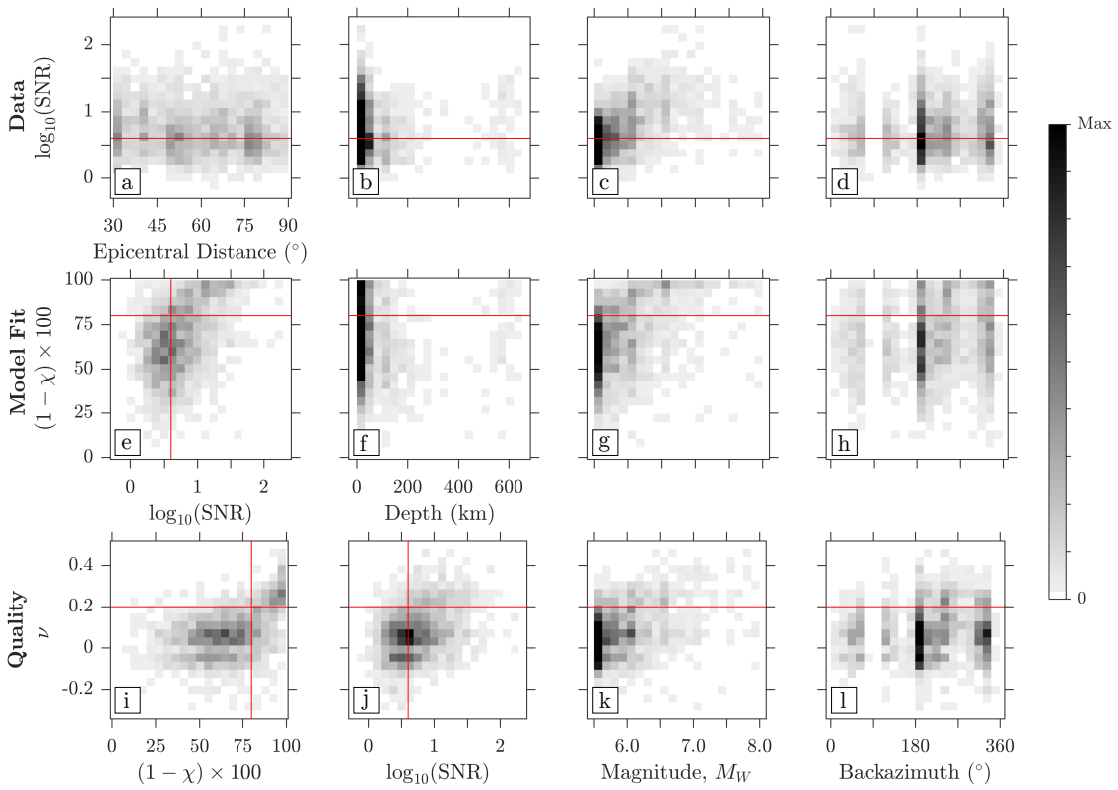


Figure 3.5: Summary of data and model quality statistics for the 1,866 events and their corresponding radial receiver functions. Threshold values used in the automated quality control selection are shown by the red lines. White denotes the absence of data density in a given bin, whereas black denotes maximum data density. Of particular interest are the relations between the vertical component data SNR, convolutional model fit, and receiver function quality parameter, ν (panels e, i, and j). Where axis labels are absent it is implied that the plot shares an axis label with the plots below it or the plots to its left.

dataset calculated with a Gaussian width $\tilde{\sigma} = 1.0$ Hz. A receiver function was accepted if it had a large, positive polarity first arrival, no monochromatic or "ringy" oscillations, and no negative-polarity arrivals of greater magnitude than the first arrival in the receiver function. In addition, we only considered receiver functions which resulted in a data fit $(1-\chi)\times 100 \geq 80\%$. This process resulted in the selection of 226 receiver functions, which were then depth-converted and stacked according to the procedure outlined in Section 3.3.4. The resulting stack and accompanying statistics for this data set are shown in Figure 3.6. We note that this data set has our quality metric ν ranging between 0.1 and 0.5. This suggests that this metric may successfully be capturing the features which receiver function practitioners typically associate with high-quality receiver functions.

Next, we repeated the receiver function stacking procedure, but this time we automated the quality control process by selecting only receiver functions with a fit greater than 80%, a signal-to-noise ratio, SNR ≥ 4, and quality metric $\nu \geq 0.2$. This value of ν was chosen based on finding that all of our synthetic data had $\nu > 0.3$. We subsequently adjusted this value down until we arrived at a suitable cut off in terms of the number of receiver functions retained. In all, 204 receiver functions met these criteria. The resulting automated stack bears a close resemblance to the manual one, aside from slight shifts in the depths corresponding to the maximum peaks in the stacks. Additionally, both methods preserve the complex nature of the 660 km discontinuity.

Inspection of the automated and manual stacks reveals a consistent signal associated with the 520 km discontinuity ('the 520') beneath Bermuda. Initially, we found this to be an interesting feature, potentially bearing compositional implications. Further probing of the dataset, however, revealed that this feature is less significant, being magnified by contamination of receiver functions in the 30–35° distance range by the *PP* phase. This is shown in Figure 3.7, where we analyzed our receiver func-

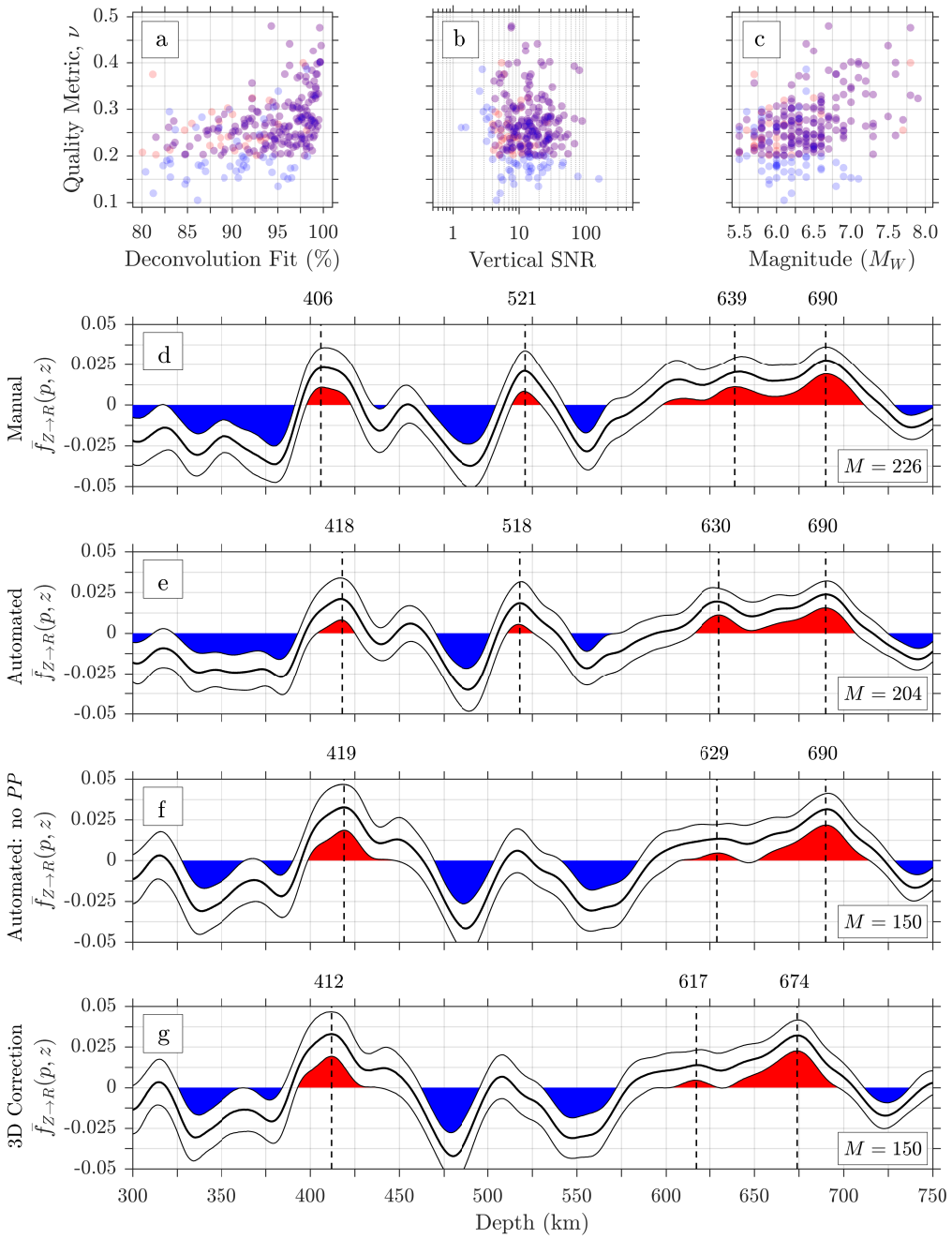


Figure 3.6: (a-c) Quality control statistics. Filled red dots correspond to the data selected by the automatic algorithm, light blue dots correspond to data selected by manual inspection, and purple dots correspond to data selected by both methods. (d) Manual, (e) automated, (f) automated after removal of *PP*, and (g) automated after removal of *PP* with 3D depth correction receiver function stacks. The stacks are made from receiver functions with no pre-filtering, computed using a Gaussian width factor $\tilde{\sigma} = 1.0$ Hz. The bold central line is the bootstrapped mean, and the thin upper and lower lines represent bootstrap estimates of two standard deviations about the mean. The dashed vertical lines indicate the locations of relevant maxima with the corresponding depths annotated above each plot. Note the general agreement between the automated and manual results.

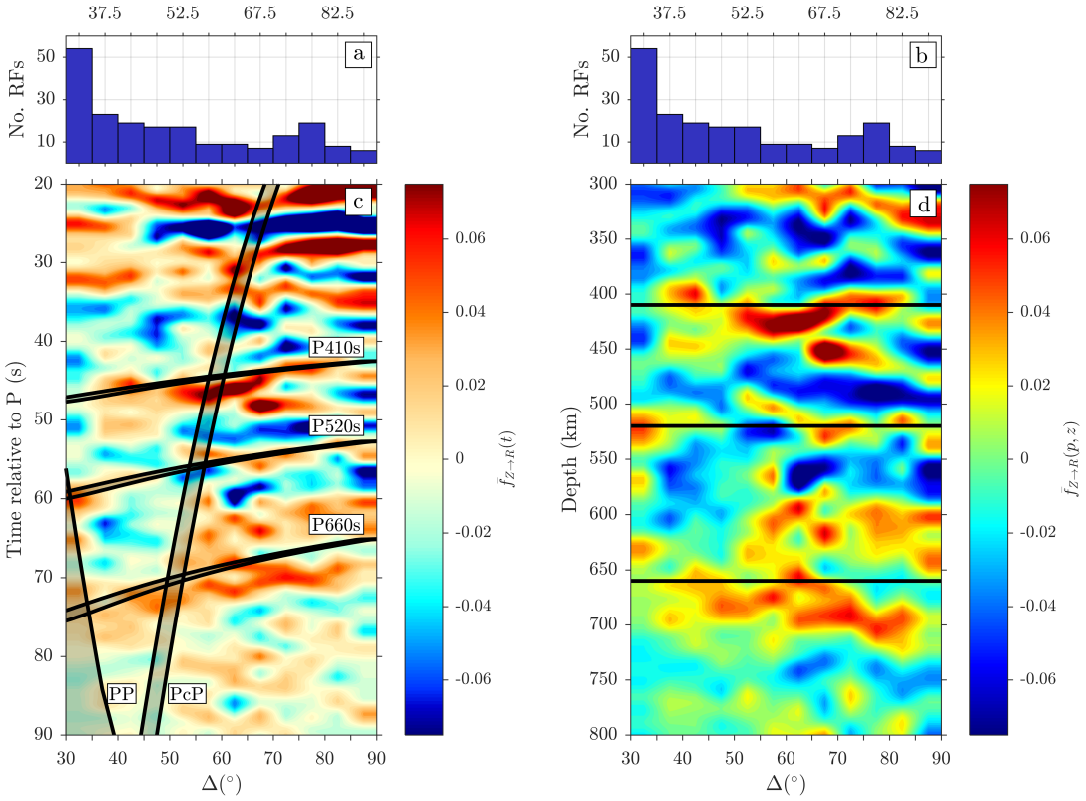


Figure 3.7: (a-b) Identical histograms showing the distribution with epicentral distance of the receiver functions that went into the construction of the panels below them. (c) Time-domain receiver functions arranged by epicentral distance. Binning is in 5° increments starting at 30°. Shaded gray regions indicate theoretical arrival times of *PP*, *PcP*, and relevant *Pds* phases from the mantle transition zone calculated using IASP91 according to eq. (3.20), for a range of earthquake depths between 0 and 653 km. Note the large signal from *PP* in the 30° to 35° bin, with a similar arrival time to *P520s*. (d) Depth-domain receiver functions, moveout-corrected using 1-D model IASP91. The 410 appears depressed, with a prominent signal between 50 and 80°, but the resolution of the depth of the 660 is poor, as it appears to occur over a broader depth range.

tions as a function of epicentral distance to see if arrivals had the correct moveout (Dueker & Sheehan 1997, Helffrich et al. 2003), and was subsequently verified by synthetic experiments. After accounting for this contamination by removing receiver functions from earthquakes with epicentral distances below 35°, the imprint of the signal associated with the 520 km discontinuity diminished (Figure 3.6f).

To explore the effects of 3-D heterogeneity on our result, we performed the same process but chose to depth convert our receiver functions using model LLNL_G3D_JPS. The resulting stack, taking into account 3-D effects, the absence of PP, and using a fully automated quality control method, is shown in Figure 3.6g. We find that the 3-D depth correction has the effect of shifting the peaks associated with the mantle transition zone up to shallower depths, while also slightly decreasing the observed transition zone thickness from 271 km to 262 km. The shifting of arrivals to shallower depths is largely due to a more accurate, thin, crustal structure, which shifts all arrivals to earlier times due to traveling a greater distance at higher mantle velocities. Aside from these slight shifts, the overall shape of the result is remarkably similar to Figure 3.6f.

3.4.2 Frequency Dependence of Results

The filter chosen when preprocessing the seismic data exerts an influence on our final results (Leahy 2009). In the stacks presented in Figure 3.6, no pre-filtering was performed. To explore the effect of filtering, we chose to pre-filter the data using a variety of pass-bands before proceeding to calculate receiver functions. The filter that we used was a fourth-order, two-pass Butterworth filter with corner frequencies at 0.02 and 1 Hz. The long-period corner of this filter was decremented in 1 s intervals, from a starting period of 50 s down to a final period of 2 s. After filtering, we calculated receiver functions using a Gaussian width factor $\tilde{\sigma} = 1.0$ Hz, and depth-converted and stacked using 1-D model IASP91 following the methodology outlined above. Earthquakes with epicentral distances smaller than 35° were discarded from the stacks. The results of this experiment are displayed in Figure 3.8. Relatively high frequency receiver functions can be found on the left hand side of Figure 3.8b, and relatively low frequency receiver functions to the right. Examples of the filter bandwidths are shown in Figure 3.8a, with shading corresponding to the receiver

functions in Figure 3.8b. For comparison, Figure 3.8c is a copy of the receiver function previously shown in Figure 3.6f.

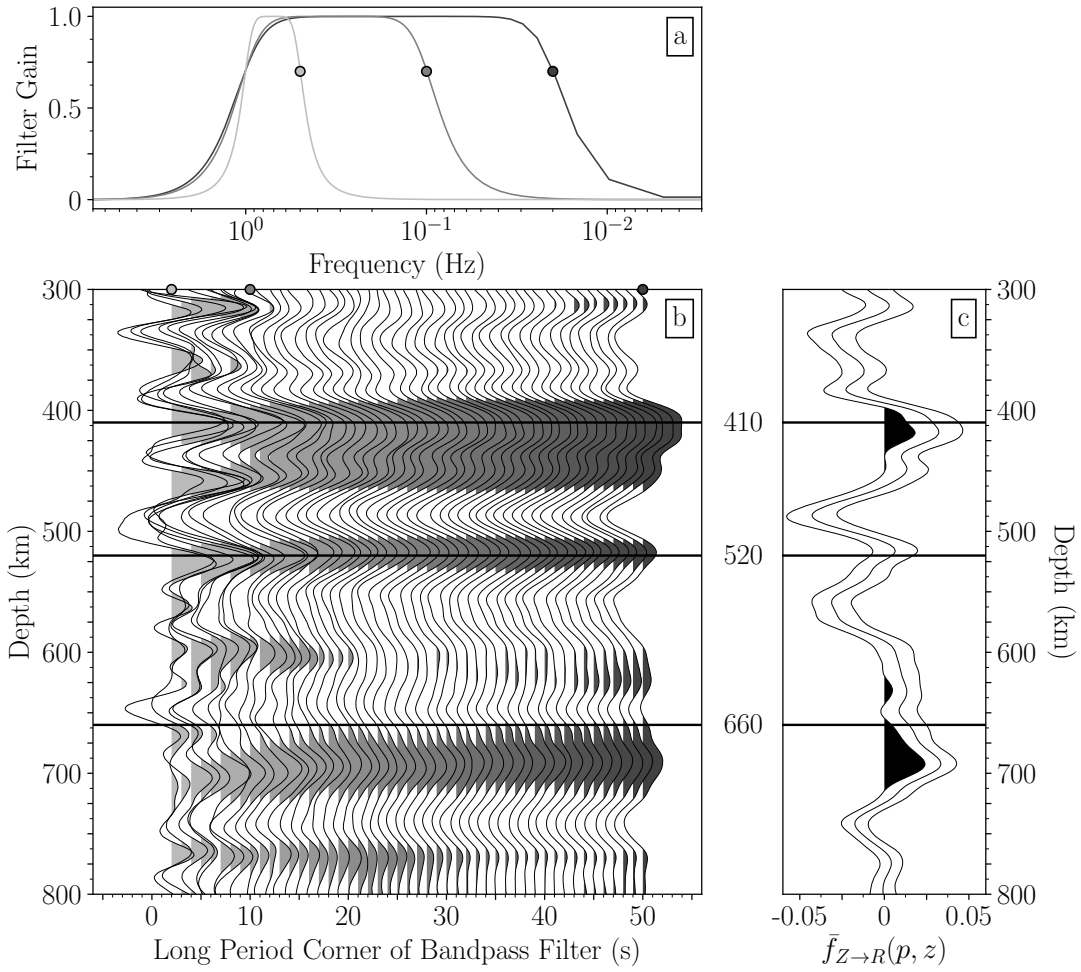


Figure 3.8: The effect of pre-filtering on receiver function stacks, using (a) a narrowing bandpass filter. (b) Depth-converted and stacked receiver functions as a function of the long-period corner of the bandpass filter used to pre-filter seismograms, alongside (c) the unfiltered, automated stack from Figure 3.6f for comparison. The short period corner is fixed at 1 s. Positive areas are colored gray, with the shading indicating the sense of the narrowing bandpass filter (a) depicted above. Note the frequency dependence of the 660 km discontinuity, which weakens at short periods, and the splitting of the peaks near 410 km into distinct peaks at short periods. Additionally, the presence of the 520 despite removal of records with *PP* interference is noteworthy, although the prominence of this signal may be exaggerated by the absence of bootstrap standard deviations.

The 410 and 660 are observed across the entire range of frequencies shown. The

depths of the discontinuities are consistent with the results shown in Figure 3.6, giving us additional confidence in their robustness. A particularly noteworthy feature is the double-peaked nature of the 410, which separates into two independent peaks at higher frequencies. Additionally, we observe a strong frequency dependence of the shallower signal in the vicinity of the 660. This observation suggests that the deeper peak observed at 674 km in our 3-D depth corrected stacks, which is consistently observed across the range of frequencies we tested, corresponds to the 660. The shallower peak at 617 km, despite appearing statistically significant in our 3-D depth corrected stacks (Figure 3.6g), appears to be a strongly frequency dependent feature.

Surprisingly, the 520 appears to be consistently imaged when the seismic data are pre-filtered. This result was unexpected, seeing as we excluded data from events with epicentral distances smaller than 35° in order to avoid interference from the *PP* phase. The visibility of this feature may be slightly exaggerated in Figure 3.8 compared to Figure 3.6f, where it is not statistically significant at the 2σ level, due to the absence of the uncertainties associated with the bootstrap resampling. Its relative prominence in the frequency bands chosen may also be indicative of the spectral characteristics of the discontinuity—perhaps it is a longer-wavelength, broader feature which is best observed at longer periods. This would be consistent with mineralogical understanding of the 520 as a broader discontinuity than the 410 or 660 (e.g. Tsujino et al. 2019).

To better constrain our observations, we produced slowness stacks, or vespagrams (Davies et al. 1971, Cottaar & Deuss 2016), of our results to determine whether or not they showed arrival times and slownesses consistent with the *Pds* phases of interest. The results of this experiment are included in Figures S2 and S3 of the supplement. The vespagrams show that the main 410 arrival and deeper 660 arrival appear consistent with the predicted arrival times and slownesses of $P410s$ and $P660s$. The secondary peak after 410 has a positive slowness, and is thus not likely related

to the 410 km discontinuity. The small peak before 660 appears broad and poorly focused in the vespagram, and thus remains difficult to classify. Additionally, there is a positive slowness arrival which contributes to this peak, which further clouds our ability to assert its robustness. We also found that the arrival from the 520 appears to have the correct slowness and arrival time of $P520s$, even after excluding events with epicentral distances smaller than 35°.

In addition to this experiment, we also performed the complimentary experiment of varying the short-period corner of the filter used from 1 s up to 50 s. The effects of this alternative series of filters were less revealing, and we found that the 410 remained visible up to periods of 25 s while the 660 was quickly suppressed at periods beyond 10 s. This suggests that the 410 may be a broader feature, an observation typically associated with water in the transition zone (van der Meijde et al. 2003), while the 660 is sharper. The results of this experiment can be found in supplementary Figure S4.

Lastly, we explored the effect of the Gaussian width factor used in the iterative time-domain deconvolution. We progressively incremented the Gaussian width factor used from 0.5 to 1.0 with a step size of 0.05, and depth converted and stacked the resulting receiver functions. The 410 and 520 remained observable and largely unchanged by this procedure, but the 660 showed some variation. At low Gaussian width factors the distinct peaks observed near 660 became indistinguishable, and progressing to higher Gaussian width factors caused them to separate out into two distinct peaks. These results are shown in supplementary Figure S5.

3.5 Discussion

Our results suggest a considerably different picture of the mantle transition zone beneath Bermuda than the previous work of Benoit et al. (2013) and Gao & Liu (2014). Contrary to the strong depressions of the 410 observed by those authors, we

only observe a modest 2 km depression of the 410 to 412 km depth, and we consistently observe a prominent signal from the 660 at a depth centered on 674 km, as shown in our 3-D depth corrected stack (Figure 3.6g). These measurements are indicative of a slightly thicker than average mantle transition zone beneath Bermuda, at 262 km thick. Although this result is not readily compatible with the idea of a whole-mantle plume beneath Bermuda, previous work has also suggested poor correlation of receiver function imaged thinned transition zones with candidate hotspot locations (Tauzin et al. 2008).

3.5.1 Estimation of a Thermal Anomaly

Using our depth-converted and stacked receiver functions, we can make an estimate of the transition-zone thickness beneath station BBSR to use as a proxy for determining the temperature anomaly from the global average. We use the following equation from Helffrich (2000) to calculate this anomaly for our calculated transition-zone thicknesses,

$$z = z_0 + \delta T \left(\frac{dz}{dP}\right) \left[\left(\frac{dP}{dT}\right)_{660} - \left(\frac{dP}{dT}\right)_{410}\right], \tag{3.22}$$

where z represents observed transition-zone thickness, and $(dP/dT)_{660}$ and $(dP/dT)_{410}$ are the Clapeyron slopes of the ringwoodite to bridgmanite and magnesiowüstite (ferropericlase) phase transition, and the olivine to wadsleyite phase transition, respectively. Following Akaogi et al. (2007), we use values of $(dP/dT)_{660} = -2.6$ MPa/K and $(dP/dT)_{410} = 3.1$ MPa/K in our estimation, and following Benoit et al. (2013), a value of $z_0 = 242$ km (Lawrence & Shearer 2006) for our global average transition-zone thickness.

3.5.2 Assessment and Interpretation of Discontinuity Structure

If we take the common approach of assuming that we are only observing the ringwoodite to bridgmanite and magnesiowüstite phase transition at the base of the transition zone in our dataset, then we choose the peak at 674 km to be representative of this transition, as it is the dominant signal across all frequencies. Using an observed value of $z = 262$ km (Figure 3.6g), results in a temperature anomaly of $\delta T = -137$ K for the mantle transition zone beneath Bermuda relative to the global average. This result is inconsistent with the presence of a hot thermal anomaly at depth beneath Bermuda in an olivine dominated mantle.

Alternatively, a second interpretation, more consistent with the idea of a hot thermal anomaly, can be justified if we consider garnet. Work by Hirose (2002) revealed that majorite garnet, a potentially major mantle constituent mineral, transforms into an aluminum bearing perovskite near 660 km depth. In addition, this phase transition is associated with a positive Clapeyron slope, meaning that the transition depth increases with increasing temperature.

Unfortunately, we cannot simply adapt eq. (3.22) to estimate the temperature anomaly taking this garnet phase transition into account. If we attempt to replace $(dP/dT)_{660}$ with $(dP/dT)_{maj.}$, the Clapeyron slope of the majorite garnet to perovskite phase transition, we find that, due to the large positive value of $(dP/dT)_{410}$, whether temperature is positively or negatively correlated with relative thickness depends on the chosen value of $(dP/dT)_{maj.}$. The appropriate value to choose for this slope is uncertain (Jenkins et al. 2016). We also do not have a good estimate for the appropriate value of z_0 for a region where the garnet system dominates. Thus we cannot extract a temperature estimate from our observations of transition zone thickness. Nonetheless, the presence of a complex 660 and the suggestion of a hot upper mantle from tomography lend some credence to this second interpretation.

Previous receiver function studies have observed similarly complex structure on the 660 and have attributed it to majorite garnet (Andrews & Deuss 2008). In addition, investigations using *PP* (Day & Deuss 2013, Deuss et al. 2006) and *SS* (Houser & Williams 2010) precursors have revealed the presence of reflections from below 660 km consistent with this interpretation. Taking these factors into consideration suggests that we may be observing a hot thermal anomaly beneath Bermuda, consistent with previous results and the idea of a whole mantle plume penetrating the mantle transition zone beneath Bermuda.

We can quantify the magnitude of such a potential hot anomaly using the tomographic models shown in Figure 3.2. Using observed seismic velocities, we can produce an estimate of the relevant temperature anomaly (Cammarano et al. 2003). From Figure 3.2, we find a $\delta V_P = -0.5\%$ and a $\delta V_S = -0.5\%$, which correspond to a roughly +100 K temperature anomaly in the transition zone beneath Bermuda. We note here that damped tomographic inversions often underestimate the amplitude of velocity anomalies **?**e.g¿[]French+2014, which suggests that this tomography-derived estimate is a lower bound on the real value.

It is also worth commenting on our observation of a discontinuity near 520 km depth. The 520 is discounted as a global feature in most seismic reference models, but is thought to arise from the wadsleyite to ringwoodite phase transition (Frost 2008). Previous studies of the mantle transition zone beneath Bermuda failed to observe a signal from the 520, but as shown by Figures 3.6 and 3.8, it can be observed although it is clearly frequency dependent. The presence of signal from the 520 at longer periods is consistent with a previous study by Shearer (1990), where long-period *PP* and *SS* data were used. Although we are using converted rather than reflected seismic phases in our analysis, our results appear to be consistent with theirs in the 1 to 50 s period range. Further analysis of receiver function data at these periods will

prove interesting, and could give greater insight into the global nature of the 520 km discontinuity.

3.6 Conclusion

We have introduced an automated and objective measure of receiver function quality that is simple to implement and tune. Using this measure produces results consistent with those typically sought when studying the mantle transition zone with receiver functions. We applied our technique to a geologically interesting location, and found results which shed new light onto the complexity of the mantle transition zone beneath Bermuda. The choice of parameters used when conducting a receiver function study can have a great deal of influence on the final result and interpretation. Considering only phase transitions in the olivine system, our results suggest a thicker than average, 262 km thick mantle transition zone reflecting a cold thermal anomaly of −137 K beneath Bermuda. Such a result was unexpected. Alternatively, considering phase transitions of garnet may lead to another possible interpretation of our observations, suggestive instead of a hot (+100 K) thermal anomaly, contingent upon this transition's presence, importance, and properties in the mantle transition zone under Bermuda. All of our results are constrained by data from a single seismometer located on the island. Future studies of this region would benefit tremendously from increased instrumentation of the island and the surrounding seafloor.

3.7 Acknowledgments

The computer code developed for this work, `rflexa`, is available at the archival repository, figshare (doi: 10.6084/m9.figshare.12311870.v1). We acknowledge the use of GMT Version 5.4.4 (Wessel et al. 2013) and the Seismic Analysis Code (SAC) Version 101.6a (Goldstein & Snoke 2005). Data for this study were provided by

the IRIS DMC (doi: 10.7914/SN/IU). This work was partly supported by the U.S. National Science Foundation under grants EAR-1736046 and OCE-1917085, and by Princeton University. High-performance computing resources were provided by the Princeton Institute for Computational Science & Engineering (PICSciE). Thorough and constructive comments by two anonymous reviewers, and by the Associate Editor, helped us improve the manuscript significantly.

3.8 Supplement

3.8.1 Synthetic Data

To verify that our methodology worked and to get a sense for the resolvability of mantle transition zone discontinuities, we calculated high frequency (2 Hz) synthetic data using the Syngine web-tool (van Driel et al. 2015). This allowed us to calculate synthetic data corresponding to the event depths, locations, and CMT solutions of our actual dataset. The results of this experiment are shown in Figure 3.9. Despite the non-uniform azimuthal and geographic extent of the data used in our study, we can indeed resolve clear and distinct signals corresponding to the 410 and 660 km discontinuities.

3.8.2 Vespagrams

An additional technique that can help to determine whether or not an observed signal is coming from a discontinuity is the calculation of vespagrams, or slowness stacks. In order to produce a vespagram, all receiver functions must be aligned and a reference slowness must be chosen. We chose to explore two different reference slownesses, the first corresponding to the median slowness of our dataset, and the second corresponding to an epicentral distance of 65°. The second slowness was chosen due to the shape

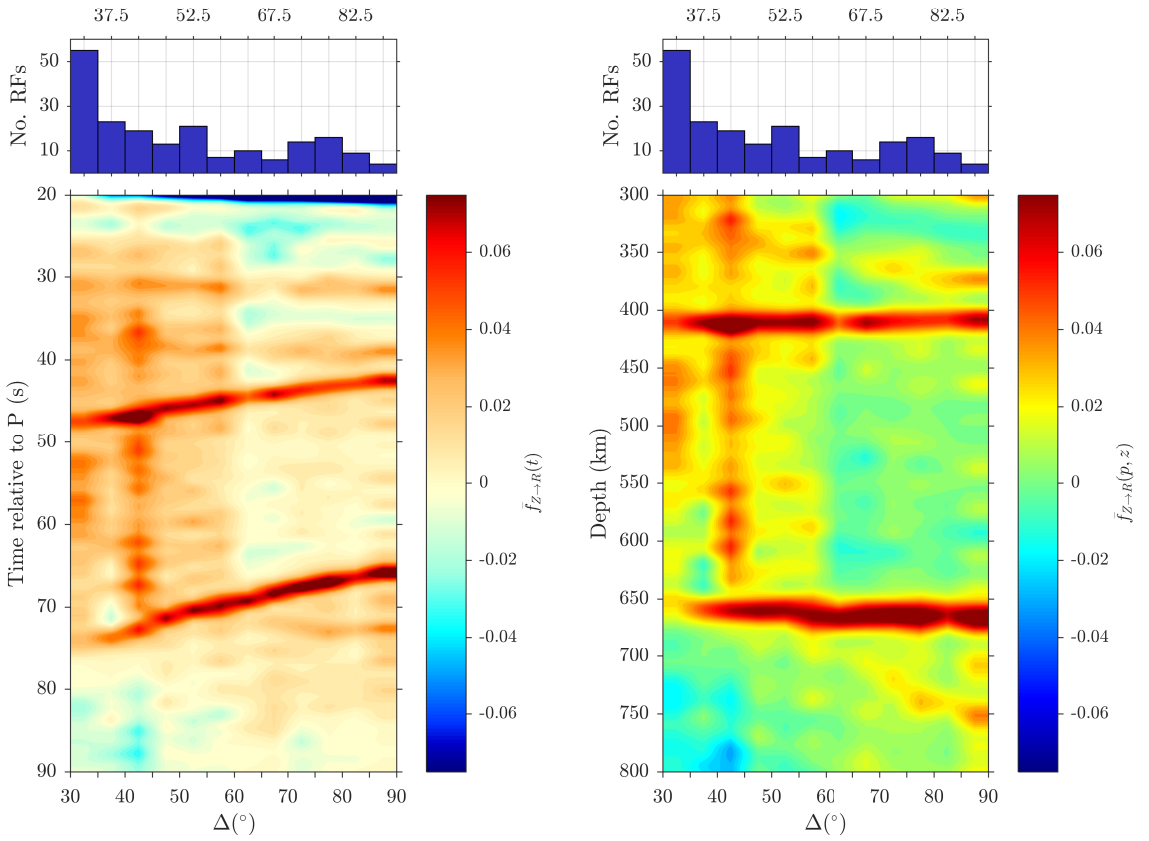


Figure 3.9: *(Left)* Synthetic receiver function data as a function of time, produced using the event depths and CMT solutions (when available) of the data used in our study. Data are binned in 5° increments, starting at 30°, as in Figure 3.7 of this chapter. *(Right)* Depth-domain synthetic receiver functions moveout corrected using 1-D model IASP91. Note that we can effectively identify the 410 and 660 km discontinuities. Interestingly, we find a considerable amount of positive amplitude 'noise' at epicentral distances less than 60° which is not associated with any discontinuity structure in the 1-D model.

of the $P410s$ and $P660s$ moveout curves, which are better approximated by a linear function at epicentral distances greater than 60° (see Figure 3.7c of this chapter).

Individual receiver functions are given a slight positive or negative time shift corresponding to the slowness perturbation being applied, and then added together. We chose to investigate a range of slowness perturbations, δp, between -0.4 and 0.3 s/°, a sufficient range to observe signals with the predicted slownesses for $P410s$, $P520s$, and $P660s$. Each of these slowness stacks is then plotted together, and the results are shown in Figures 3.10 and 3.11. We observe bright spots (in this

case, colored red) when the receiver functions stack coherently, and by comparing the slowness and travel times of these coherent arrivals to our predictions we can determine if they match.

In Figures 3.10 and 3.11, we show predicted vespgrams calculated using the synthetic data mentioned above, observed vespagrams for events with epicentral distances between 30° and 90°, and observed vespagrams for events with epicentral distances between 35° and 90°. By testing these two different ranges, we hope to determine whether or not the signal we observe near 520 km is related to the presence of a discontinuity or is simply an artifact caused by contamination from *PP*. In both cases, we observe a small but coherent signal at the predicted slowness and arrival time of $P520s$, giving us confident that we are observing a weak signal from this discontinuity. Additionally, we find that the observed signals from the 410 and 660 have the appropriate slownesses, but are not as sharp as the arrival from the 520. The signal which appears to arrive just after the 410 appears to be associated with a positive slowness feature, so is likely an unrelated artifact. Interpretations of the 660 remain complicated, with a clear arrival with the correct slowness coming in just after the predicted time, but also with a fuzzy signal at earlier times.

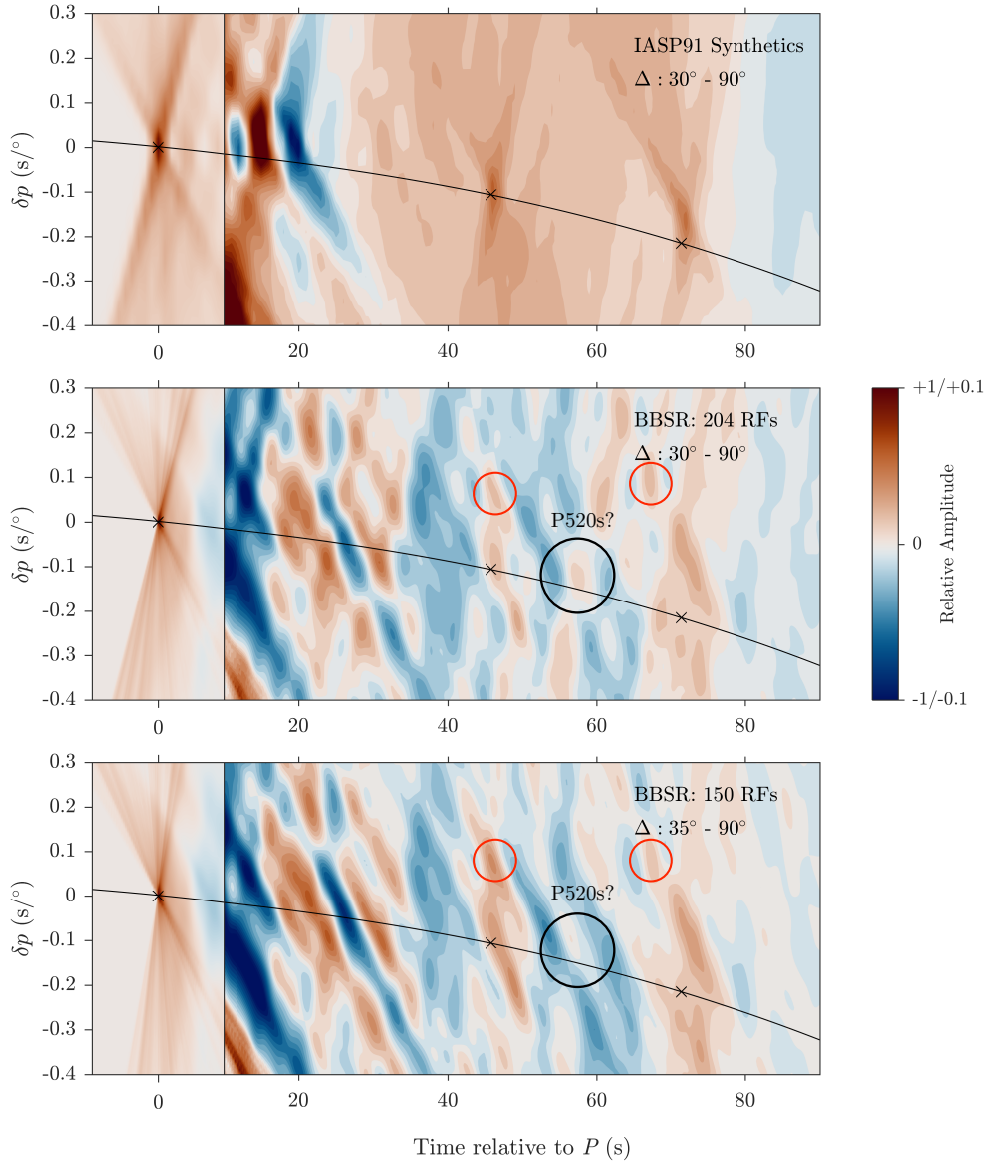


Figure 3.10: *(Top)* Vespagram showing the predicted arrival times and relative slownesses of P, $P410s$ and $P660s$ (denoted by small crosses), for a set of synthetic data using the same event-station locations and CMT solutions as the real dataset. A reference slowness of 7.775 s/° was used, corresponding to an epicentral distance of 47.5°, the median event epicentral distance of the dataset. *(Middle)* Vespagram calculated using the observed BBSR data, using the same procedure as the top panel. Predicted *Pds* conversion times are indicated by the line. The positive amplitude region which stacks to produce a small 520 signal is indicated with a black circle. The two small red circles indicate positive slowness arrivals which may contribute to our observed 410 and 660 signals. The positive slowness arrival before the predicted 660 time is likely contributing to the small peak we observe at 617 km in our 3-D depth-corrected stacks, weakening our ability to assert its robustness. *(Bottom)* Same as middle panel, but for BBSR data with epicentral distances 35° to 90°, to eliminate interference from *PP*. Note that there is still a modest signal with a slowness and travel time corresponding to $P520s$.

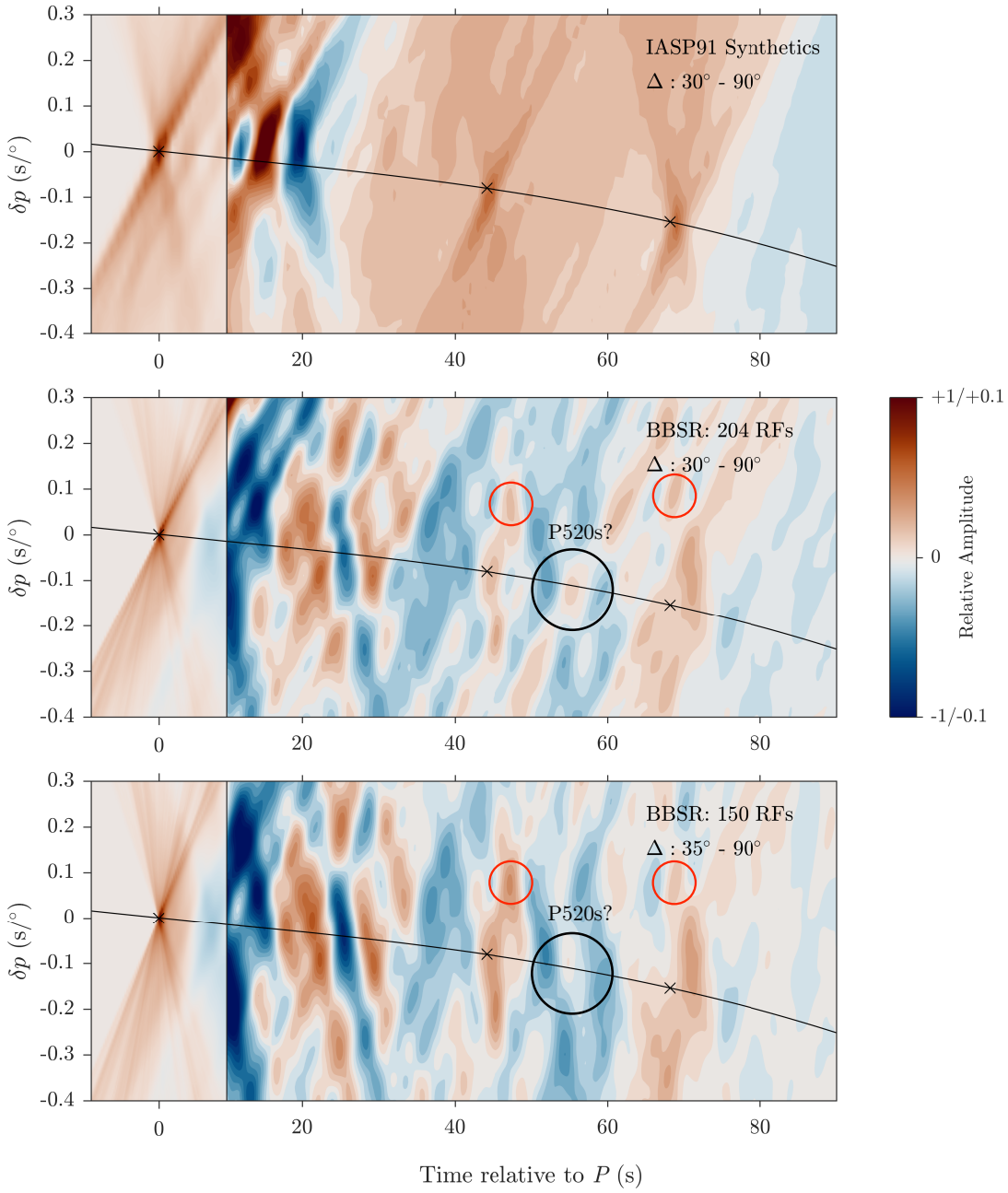


Figure 3.11: Same as Figure 3.10, but using a reference slowness of 6.510 s/°, corresponding to an epicentral distance of 65°. Note that this reference slowness provides a better fit to the synthetic data. This is because the moveout curve of $P410s$ and $P660s$ is non-linear at epicentral distances less than approximately 60°, but becomes essentially linear at epicentral distances beyond that.

3.8.3 Effects of Filtering and Gaussian Width

In addition to investigating the effect of varying the long period corner of the bandpass filter used on the seismic data, we performed experiments where we varied the short period corner of the filter as well as the Gaussian width factor used in the iterative time-domain deconvolution. For the filtering experiment, we held the long period corner fixed at 50 s, and progressively varied the short period corner from 1s to 50 s. The results of this experiment are shown in Figure 3.12. Note that the signal from the 410 persists longer than the signal from the 660 in this experiment, suggesting that it may be a longer wavelength, lower frequency structure. The 520 and 660 are rapidly diminished, suggesting that they may be shorter wavelength features. Beyond 30 s, all signals are effectively eliminated due to the filter becoming too narrow band.

To investigate the effects of the Gaussian width factor, we calculated receiver functions using Gaussian width factors between 0.5 and 1.0, using a step size of 0.05. These receiver functions were then depth converted and stacked, and the results are shown in Figure 3.13. We find that the observability and shape of the 410 and 520 km discontinuities are largely unaffected by the Gaussian width factor used. The 660, on the other hand, shows a more interesting dependence. For low Gaussian width factors, corresponding to lower frequencies, the 660 appears broader and single peaked. As we move to higher Gaussian width factors, two individual peaks begin to separate out, leading to the shallow and deep signals near 660 observed earlier in this chapter.

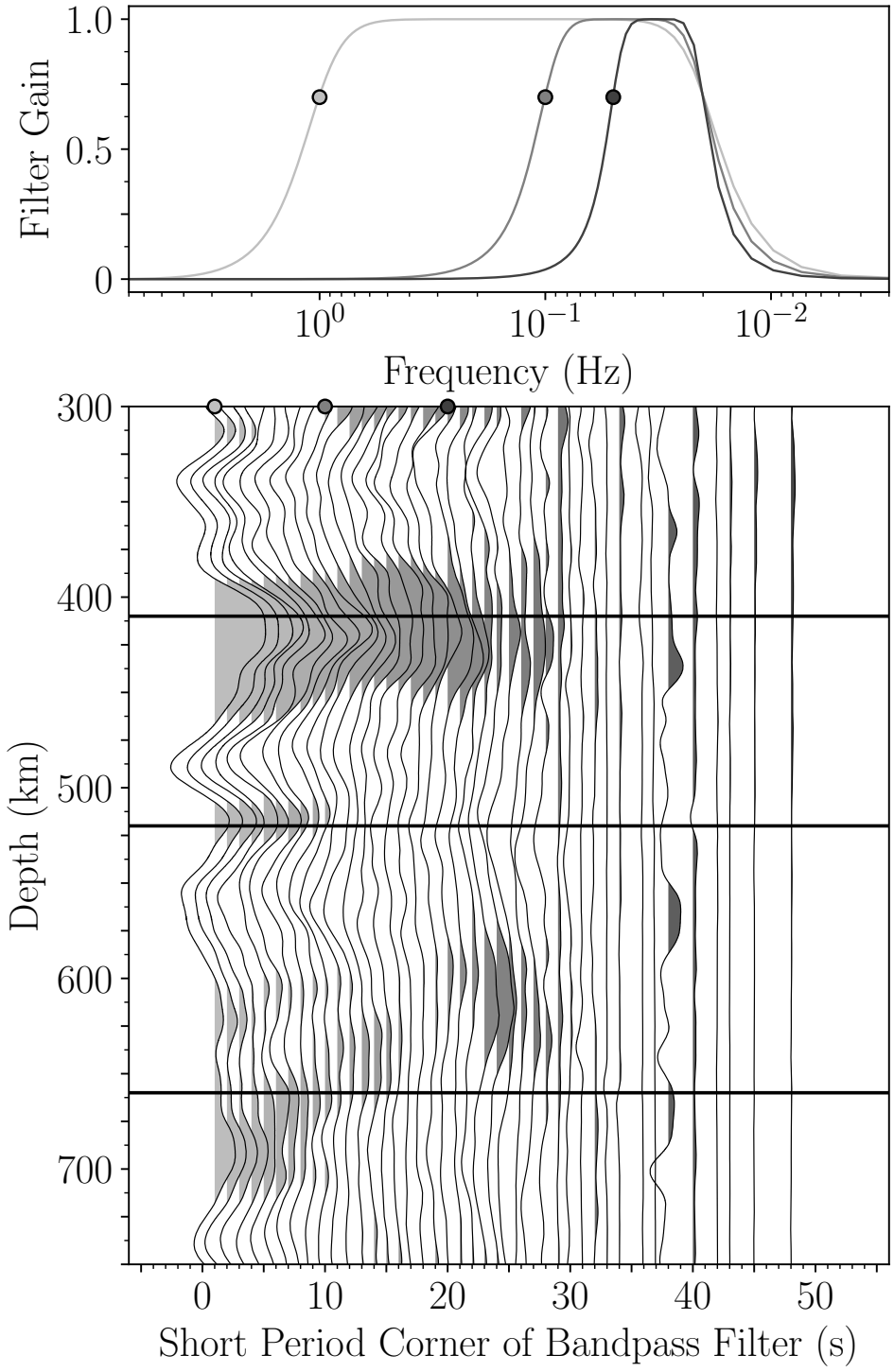


Figure 3.12: Same as Figure 8 of the main text, but varying the short period corner of the bandpass filter used on the input seismograms instead of the long period corner. The long period corner is fixed at 50 s. Positive areas are colored grey, with the shading indicating the sense of the narrowing bandpass filter shown in the top panel.

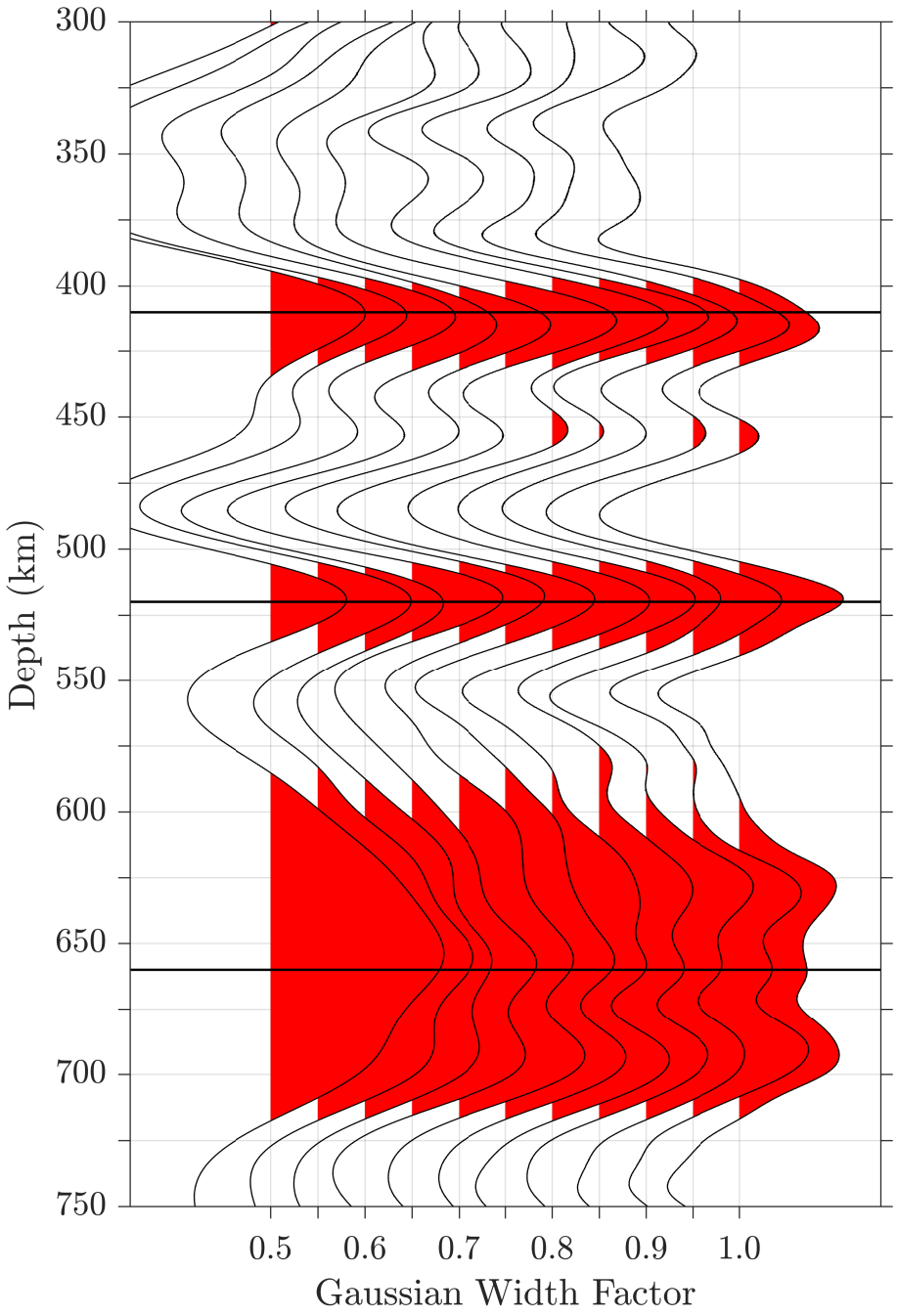


Figure 3.13: Effect of varying the Gaussian width factor used to produce receiver functions from unfiltered data. Higher Gaussian width factors can be interpreted as higher frequency receiver functions, hence the increased resolution of short wavelength features.

Chapter 4

The mantle transition zone beneath eastern North America: A record of subduction and hotspot volcanism*

4.1 Abstract

The eastern continental margin of North America, despite being a passive margin at present, records a comprehensive tectonic history of both mountain building and rifting events. This record is punctuated by several igneous events, including those associated with the Great Meteor and Bermuda hotspots. To gain a better understanding of the state of the mantle beneath this region, we employ the massive quantity of seismic data recorded by the USArray to construct images of the mantle transition zone beneath eastern North America. To construct these images, we first calculate P-to-s receiver functions using the iterative time domain deconvolution algorithm. These receiver functions are then automatically filtered by their quality, using a set of rigorous criteria, and subsequently summed using common conversion point stack-

*This chapter has been submitted as a standalone manuscript with the same title as this chapter and authorship, **Burky, A. L.**, Irving, J. C. E., & Simons, F. J. to *Earth and Planetary Science Letters* and is awaiting peer-review.

ing. We show several cross sections through these stacks, highlighting remarkable features such as a thinned transition zone beneath the previously observed northern Appalachian and central Appalachian low-wavespeed anomalies, as well as thickened transition zone beneath western Tennessee associated with the Laramide slab stagnating at depth. In addition to discussing these geologically-relevant features, we perform a technical analysis of the effects of using various seismic velocity models for the moveout correction of our receiver functions. We find that the thickness of the mantle transition zone under eastern North America is a robust measurement, while the resolved depths of the 410 and 660 km discontinuities are model dependent.

4.2 Introduction

To acquaint the reader with the key events that have shaped the geologic history of eastern North America, we briefly review them here. A sensible starting point is the Appalachian orogeny, which occurred roughly 300 Ma during the collision of the African and North American continents (Hatcher et al. 2010). Around 230–200 Ma, the supercontinent of Pangaea broke up, causing eastern North America to rift apart from Africa (Brunsvik et al. 2021). By roughly 100 Ma, the Farallon slab was subducting beneath central North America (Sigloch 2011), while the Great Meteor hotspot was active beneath New England (Kinney et al. 2021). Finally, roughly 50–30 Ma, magmatic activity in the region led to the formation of Bermuda and scattered basaltic volcanism in the central Appalachians (Mazza et al. 2014). When we consider all of these events, it makes sense that eastern North America warrants a special classification as a *volcanic* passive margin (Geoffroy 2005).

In this work, we employ mantle transition zone (MTZ) receiver functions to map out the depths of the 410 and 660 km discontinuities (hereafter referred to as 'the 410' and 'the 660') beneath eastern North America, as well as the overall MTZ thickness

(for a comprehensive review of mantle seismic discontinuities, see Deuss et al. 2013). Our high-resolution results are made possible by the dense spatial coverage of data provided by the USArray (Long et al. 2014). Previous receiver function studies using USArray data have observed a variety of features in the MTZ beneath the eastern US: notably, thickening beneath the midwest from Iowa to Tennessee (Maguire et al. 2018) and moderate thinning beneath areas along the Atlantic coastal plain into the Appalachians (Keifer & Dueker 2019). These observations agree with an earlier receiver function study which also identified thinning in the region (Li et al. 1998).

In addition to receiver functions, work has been done using *SS* precursors to map the structure of the MTZ beneath North America. One difficulty with these studies is the reliance on favorable event-station geometries for *SS* bounce points, leading to poorer resolution than receiver functions beneath the USArray in North America (Houser 2016, Huang et al. 2019). This problem has only recently begun to be remedied with methods to use near station topside reverberations, such as $Ss660s$, which increase the range of usable geometries for precursor studies (Shearer & Buehler 2019). Interestingly, this study also observed thickening of the MTZ beneath the midwest, with a pronounced thickening below western Tennessee. The thinning beneath the Atlantic coastal plain, however, appears more modest but lies on the boundary of the study's resolvable region.

Adding to the complexity of this region is the New Madrid Seismic Zone (NMSZ) beneath eastern Missouri and western Tennessee, which has been the host of several large earthquakes in recorded history (Page & Hough 2014). MTZ studies have identified significant thickening beneath the NMSZ (Gao & Liu 2014), but the link between these two features remains uncertain (Forte et al. 2007). This thickening has, however, been attributed to a stagnant portion of the Farallon slab, referred to as the Laramide slab, residing in the MTZ today (Sigloch 2011). This feature has

been consistently resolved in a P wave travel-time tomography study (Wang et al. 2019), and a joint P and S wave travel-time tomography study (Savage 2021).

4.2.1 The Northern Appalachian Anomaly

In the northeastern United States, seismic studies have revealed the presence of a strong, localized, low-velocity anomaly, which has been hypothesized as an indication of geologically recent asthenospheric upwelling 100 to 300 km beneath New England (Menke et al. 2016, Levin et al. 2018). This feature has been referred to as the Northern Appalachian Anomaly (NAA) (Schmandt & Lin 2014). Geographically coincident with this feature is the track of the Great Meteor Hotspot (Morgan 1971), which is thought to have underlain the region from ∼140 to 100 Ma (Kinney et al. 2021), but now underlies the Atlantis-Meteor Seamounts (Sleep 1990) east of the Mid-Atlantic Ridge. Attributing the present day seismic velocity anomalies to this long gone hotspot appears contradictory (Eaton & Frederiksen 2007), and has encouraged authors to propose alternative scenarios such as edge-driven convection (King & Anderson 1998), or lithospheric delamination after the Appalachian orogeny some 300 Ma (Nelson 1992, Levin et al. 2000).

A geochemical study by Torgersen et al. (1995) measured excess ^{3}He in groundwater in New Hampshire. Their observations were suggestive of geologically recent contamination by a reservoir containing primordial mantle helium, which is typical of volcanically active regions such as ocean islands (Jackson et al. 2017)—not of geologically old and quiescent regions like the northeastern United States. One possible explanation for this signature is that it is a remnant of the extensive White Mountain plutonism (190-90 Ma) associated with the passage of the Great Meteor plume.

Moving deeper, several recent tomography models have imaged low velocity anomalies extending through the mantle transition zone (MTZ) beneath this region. Sigloch (2011) refers to these features as the “slow blanket” above the old Farallon slab, owing

to their location directly above an eastward dipping high velocity feature beneath the Midwest and eastern North America. A more recent tomography study by Savage (2021) also imaged low V_P and V_S anomalies extending through the MTZ beneath this region. The appearance of these anomalies directly above the old Farallon slab is not likely to be a coincidence, and some authors have speculated it may be the signature of a deep de-watering phenomenon (van der Lee et al. 2008).

4.2.2 The Central Appalachian Anomaly

Moving south, the presence of a roughly linear seismic low-velocity anomaly in the lower lithosphere extending from Missouri to Virginia has been tenuously interpreted as a previously undetected hotspot track (Chu et al. 2013). This theory is reinforced by the presence of 75-Myr-old diamondiferous kimberlites in Kentucky (Agee et al. 1982), thought to be sourced from a deep mantle reservoir. The timing of these events, however, is inconsistent with Eocene ($\sim$47 Ma) basaltic volcanism in this same region (Mazza et al. 2014). This second event is temporally coincident with offshore magmatic activity which led to the formation of Bermuda and its associated large bathymetric swell (Vogt & Jung 2007), whose origin remains ambiguous (Burky et al. 2021*b*) due to the lack of an associated hotspot track and geochemical signatures (Mazza et al. 2019).

A study of seismic anisotropy in this region observed null splitting near the Atlantic coast, which the authors interpreted as vertical flow induced by the impinging Farallon slab (Long et al. 2010). These observations are compounded by the presence of high attenuation in the asthenosphere beneath the area, ascribed to upwelling asthenosphere and the possible presence of melt (Byrnes et al. 2019). Seismic tomography models consistently resolve a low velocity anomaly extending through the upper mantle beneath this region at present (e.g. Simmons et al. 2010, 2012, Schaeffer & Lebedev 2014, Lei et al. 2020), belying the relation to a long-gone hotspot once

again. These low velocity anomalies are so persistent in tomography models that they have been referred to as the Central Appalachian Anomaly (CAA) (Schmandt & Lin 2014).

4.3 Data & Modeling

Our main tool in this work is the P-to-s conversion of teleseismic earthquake waves at discontinuities in the mantle. To isolate these converted phases, we first requested three-component seismograms recorded by a subset of USArray stations (network code TA, for transportable array) for all recorded earthquakes (typically in a timespan of 2 years within 2012-2016 for each station) with a moment magnitude, $M_w > 5.5$, and within an epicentral distance, $35° \leq \Delta \leq 90°$, of the station (see Figure 4.1). This resulted in 1,995 events recorded by 702 stations. We then removed the mean and trend from each record, and corrected for the instrument response, converting our seismograms from digital counts to units of velocity (m/s) using the methods outlined by Burky et al. (2021*a*). Before any subsequent processing, we bandpass filtered all seismograms between 0.02 and 0.2 Hz using a third-order Butterworth filter. Each record was then cut 30 s before and 90 s after the theoretical P-wave arrival time in 1-D seismic velocity model IASP91 (Kennett & Engdahl 1991), to create a record containing only the P-wave and its coda. To maximize P-to-s converted energy, we rotated the horizontal components from the north and east (NE) orientation to the radial and transverse (RT) orientation.

After performing these preliminary processing steps, we calculated receiver functions by deconvolving the vertical (Z) component from the radial (R) component using the iterative time domain deconvolution algorithm of Ligorría & Ammon (1999) (see also Burky et al. 2021*b*). This resulted in 173,801 receiver functions. Before continuing with any analysis, we performed an automated quality control of these receiver

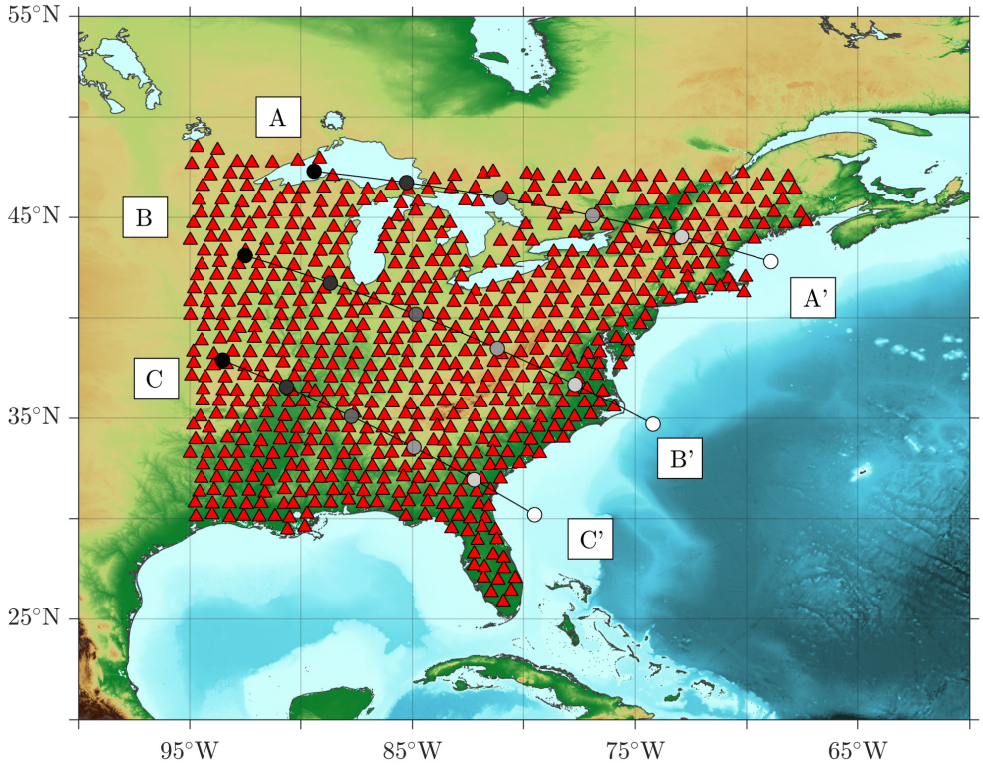


Figure 4.1: Geographic distribution of the USArray Transportable Array (TA) seismometers (red triangles) which contributed data to our study. Overlain great-circle sections indicate the locations of cross-sections A-A', B-B', and C-C', which are discussed later in this chapter. The colored dots are intended to act as a reference for distances along the cross-section. Also worth noting are the Great Meteor seamounts near label A', and the bathymetric swell surrounding Bermuda east-southeast of label B'.

functions. The four parameters that we calculate for each receiver function are, (1) the Z component signal-to-noise ratio (SNR), (2) the R component SNR, (3) the quality of fit calculated during the iterative time domain deconvolution, and (4) a receiver function quality factor, ν, quantifying the shape of the resulting receiver function (for further details about these four parameters, see Burky et al. 2021*b*). We accepted receiver functions with SNR values greater than 2, quality of fit greater than 80%, and ν greater than 0.1. After this step, 40,571 receiver functions remained (see Figure 4.2 for the geographic distribution of the accepted receiver functions). Although our dataset shows a geographic bias in terms of the distribution of events, this does not influence any of our interpretation due to the extremely dense station coverage provided by the USArray (see Figure 4.3).

4.4 Methods

In order to meaningfully analyze and interpret our receiver functions, we performed additional processing steps to resolve the mantle transition zone discontinuities that we are concerned with imaging. The first of these steps is the moveout correction of our data, allowing us to go from the time domain to the depth domain via a seismic velocity model. Then, using these depth domain receiver functions, we can produce images of the desired discontinuities by utilizing stacking techniques. These stacks can then be visualized and analyzed to construct maps of the MTZ properties across our study region.

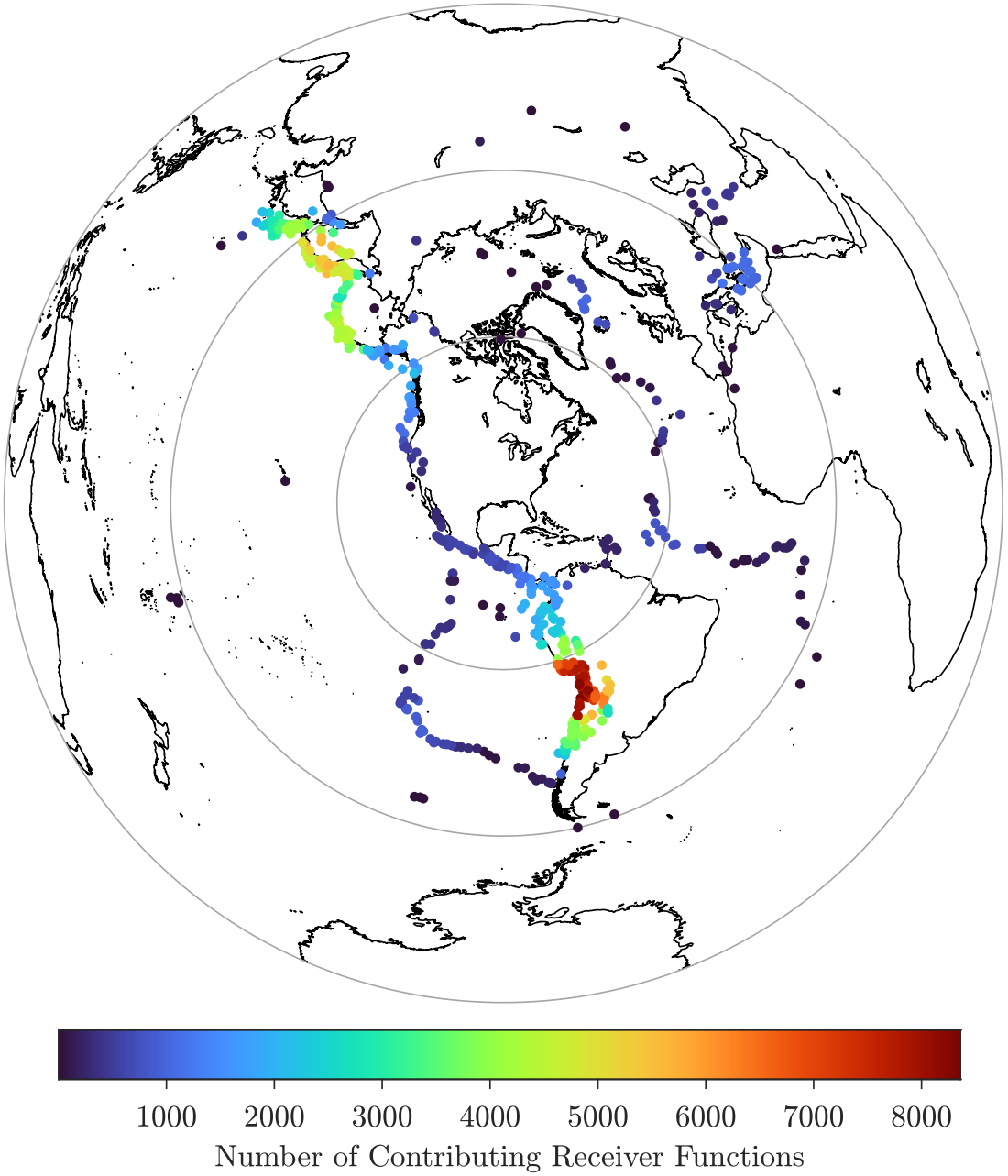


Figure 4.2: Geographic distribution of the events contributing to the 40,571 high quality receiver functions used in this study. Concentric gray circles are evenly spaced at distances of 45° from one another, up to a maximum of 135° from the center of the array. Most of our data come from events along the Pacific Ring of Fire, but there are additional contributions from the Mid-Atlantic Ridge and the eastern Mediterranean.

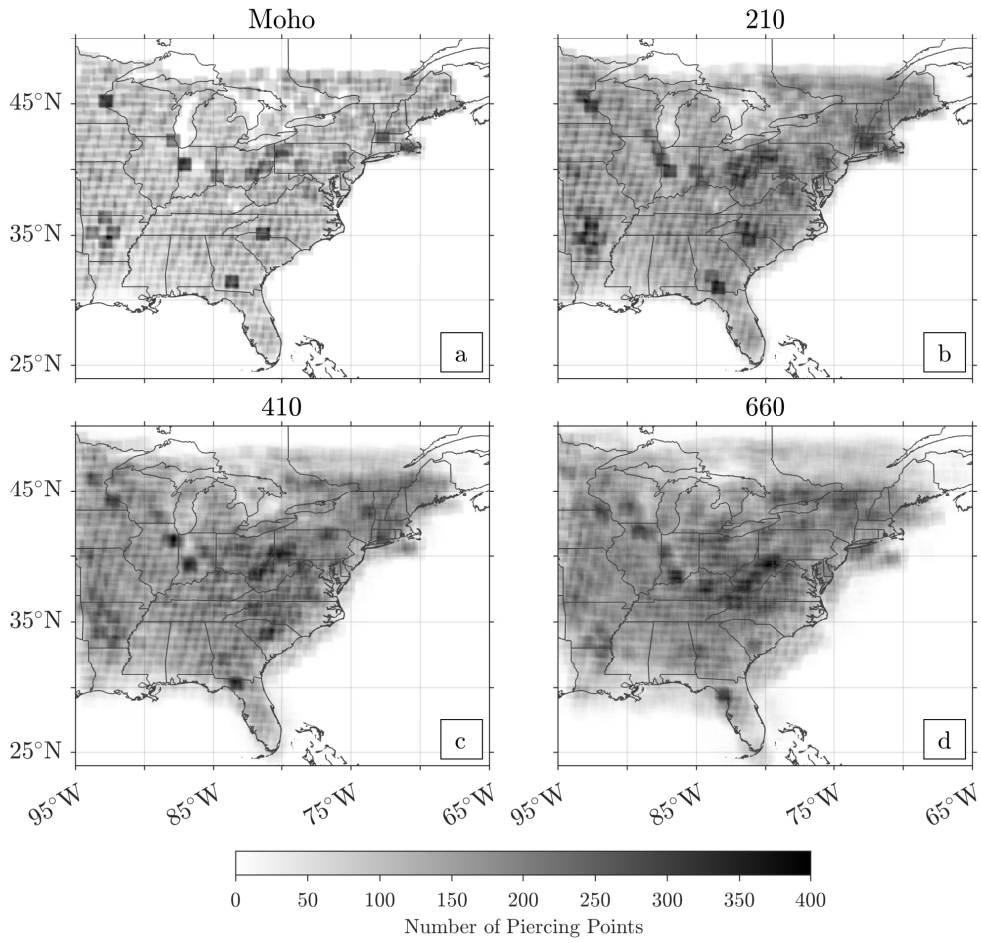


Figure 4.3: Density maps showing the number of receiver functions contributing to each of our $1^\circ \times 1^\circ$ cells at four depths in the mantle (Moho corresponds to a depth of 35 km). Note that the ray coverage is fairly uniform throughout the mantle transition zone, but is biased by the locations of stations at shallower depths.

4.4.1 Time to Depth Conversion

To accomplish our first task of depth converting the receiver functions, we make use of the following time to depth conversion formula (Chevrot et al. 1999):

$$t_{Pds}(p,z) = \int_0^Z \left[\sqrt{V_S^{-2}(z) - p^2 r^{-2}} - \sqrt{V_P^{-2}(z) - p^2 r^{-2}} \right] dz, \tag{4.1}$$

where $t_{Pds}(p,z)$ is the time in the receiver function corresponding to a conversion from a particular depth, Z, in a seismic velocity model with P and S wave speeds as a function of depth z, given by $V_P(z)$ and $V_S(z)$. p is the P wave ray parameter (s/km)

of the particular event station pair, and $r \in [0, 1]$ is the ratio of the discontinuity radius, $R_\oplus - Z$, to the Earth's radius, $R_\oplus$. We compute this integral in six different velocity models, using a depth increment of $\Delta z = 0.1$ km.

The first model which we used to perform time-to-depth conversion was one-dimensional (1-D) model IASP91 (Kennett & Engdahl 1991). Next, we used a hybrid 1-D/3-D model made by replacing the crust in IASP91 by the 3-D global crustal velocity model CRUST1.0 (Laske et al. 2013). Lastly, we used four different 3-D tomography models. Three of these models are global models: GyPSuM (Simmons et al. 2010), LLNL_G3-D_JPS (Simmons et al. 2012), and GLADM25 (Lei et al. 2020), and the fourth model is a regional model of North America, SL2013NA (Schaeffer & Lebedev 2014). In order to use the integral above with these 3-D models, we had to raytrace to find the paths corresponding to each event-station pair in our dataset. For model LLNL_G3D_JPS, this was possible using the software package which accompanies the model which performs raytracing between two arbitray coordinates. For the remaining models, paths computed in 1-D models IASP91 and PREM (Dziewoński & Anderson 1981) using the Tau-P toolkit were used. The models were then queried along these raytraced paths to construct the necessary velocity profiles, $V_P(z)$ and $V_S(z)$.

4.4.2 Common Conversion Point Stacking

The dense geographic distribution of stations in our dataset allowed us to employ array processing techniques to robustly construct high resolution images of the MTZ beneath eastern North America. Specifically, we produced common conversion point (CCP) stacks of our data, inspired by the method outlined by Dueker & Sheehan (1997).

First, we calculated theoretical raypaths through 1-D model IASP91 for all of our event-station pairs using the TauP Toolkit (Crotwell et al. 1999). Next, we

constructed a grid containing the latitude range 22.5°N to 51.5°N, and the longitude range 98.5°W to 63.5°W, with a $1° \times 1°$ grid size. We then found where the computed raypaths pierced our grid at depths: 35 km, 210 km, 410 km and 660 km. Depth-converted receiver functions corresponding to each of these rays were then stacked together with the other rays which were contained in the $1° \times 1°$ cell, to create a volume where the center of each cell contained a CCP stacked receiver function. The entire grid was then shifted sequentially by increments of 0.1°, and the stacking was repeated, until the grid had been shifted by 1°. This resulted in a volume with CCP stacks of $1° \times 1°$ stacking width on a grid of resolution $0.1° \times 0.1°$. Finally, the CCP volumes containing each of our four chosen piercing depths (35 km, 210 km, 410 km, and 660 km) were stitched together to construct our final CCP volume, where the depth range 0 to 120 km corresponds to the 35 km stack, 120 to 300 km corresponds to the 210 km stack, 300 to 530 km corresponds to the 410 km stack, and 530 to 750 km corresponds to the 660 km stack (the stitched joins can be seen in the cross-section slices shown in Figures 4.4–4.6).

The data density of our CCP stack is shown in Figure 4.3. Our data coverage in the mantle transition zone is fairly consistent over the entire study region, and the majority of bins beneath the continent contain at least 100 receiver functions.

4.5 Results

After computing the CCP stacks described above, we have at our disposal a collection of six different images of the mantle transition zone beneath Eastern North America. Using these stacks, we can gain insight into two important questions: first, what is the effect of the choice of seismic velocity model on the resulting image? And second, are there specific features of the mantle transition zone discontinuity structure which are clearly and commonly resolved in each of our CCP stacks?

In an effort to answer the first question, we start by visually comparing a sequence of cross sections taken through each of our CCP stacks. Selected cross sections can be found in Figures 4.4, 4.5, and 4.6. The first point to note is that we clearly resolve both the 410 and 660 in each of these cross sections, regardless of the velocity model used to moveout correct our receiver functions. Second, the average amplitude of the 410 signal tends to be higher than that of the 660 signal (see Figure 4.15). Third, each of the selected cross sections displays a considerable amount of topography on the MTZ discontinuities. This is explored more fully below. Finally, the resulting images seem to resolve consistent features regardless of the velocity model used, but with relative shifts in the depths of the discontinuities.

To further explore this final point, we performed pairwise cross correlations of each of our CCP stacks, in an effort to see how consistent the resolved features were. We found that our stacks were strongly correlated with one another ($\rho > 0.9$) with relative shifts of about 10–20 km. Animations showing these cross correlations across the entire CCP volume can be found in the Supplement. This result shows that the choice of velocity model used in depth converting receiver functions can lead to large variations in the resulting depths of the 410 and 660 discontinuities. However, these variations tend to shift both discontinuities in the same direction, implying that the resulting measured thickness of the mantle transition zone is less sensitive to the choice of velocity model.

To help illustrate this point, as well as to explore the geographic variations in the MTZ discontinuity structure, we made maps showing the depths of the 410 and 660, as well as the measured MTZ thickness, in all of our 3-D corrected CCP stacks (see Figure 4.7). In these maps, we can see that model GLADM25 tends to shift the 410 and 660 to greater depths, while model SL2013NA tends to shift them to shallower depths. Models GyPSuM and LLNL_G3-D_JPS show less exaggerated shifts of the discontinuities away from 410 and 660 km. All four models, however, show a relatively

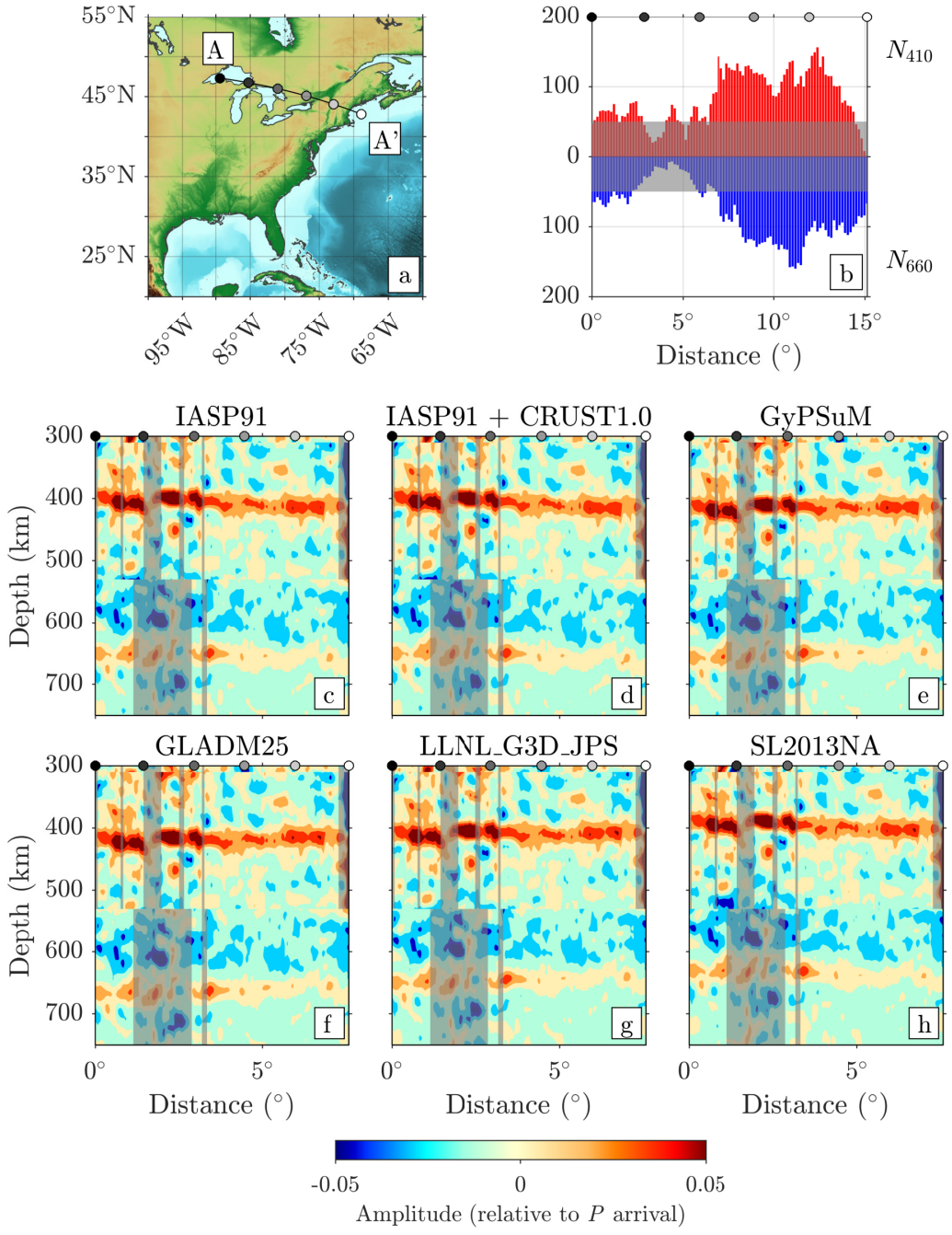


Figure 4.4: (a) Map showing the location of the cross section taken through the six different CCP stacks explored in our study. This particular cross section cuts through the purported NAA. (b) Histogram showing the number of receiver functions contributing to the (red) 410 portion and (blue) 660 portion of the CCP stacks. Data quantity tapers off near the Great Lakes and into Canada. (c-h) Cross sections through CCP stacks in the six different velocity models described in the Methods section. Bins with less than 50 receiver functions are covered with a transparent grey box, corresponding to the greyed out region of panel (b). Note the relative thinning from NW to SE along this cross section, coincident with the location of the NAA.

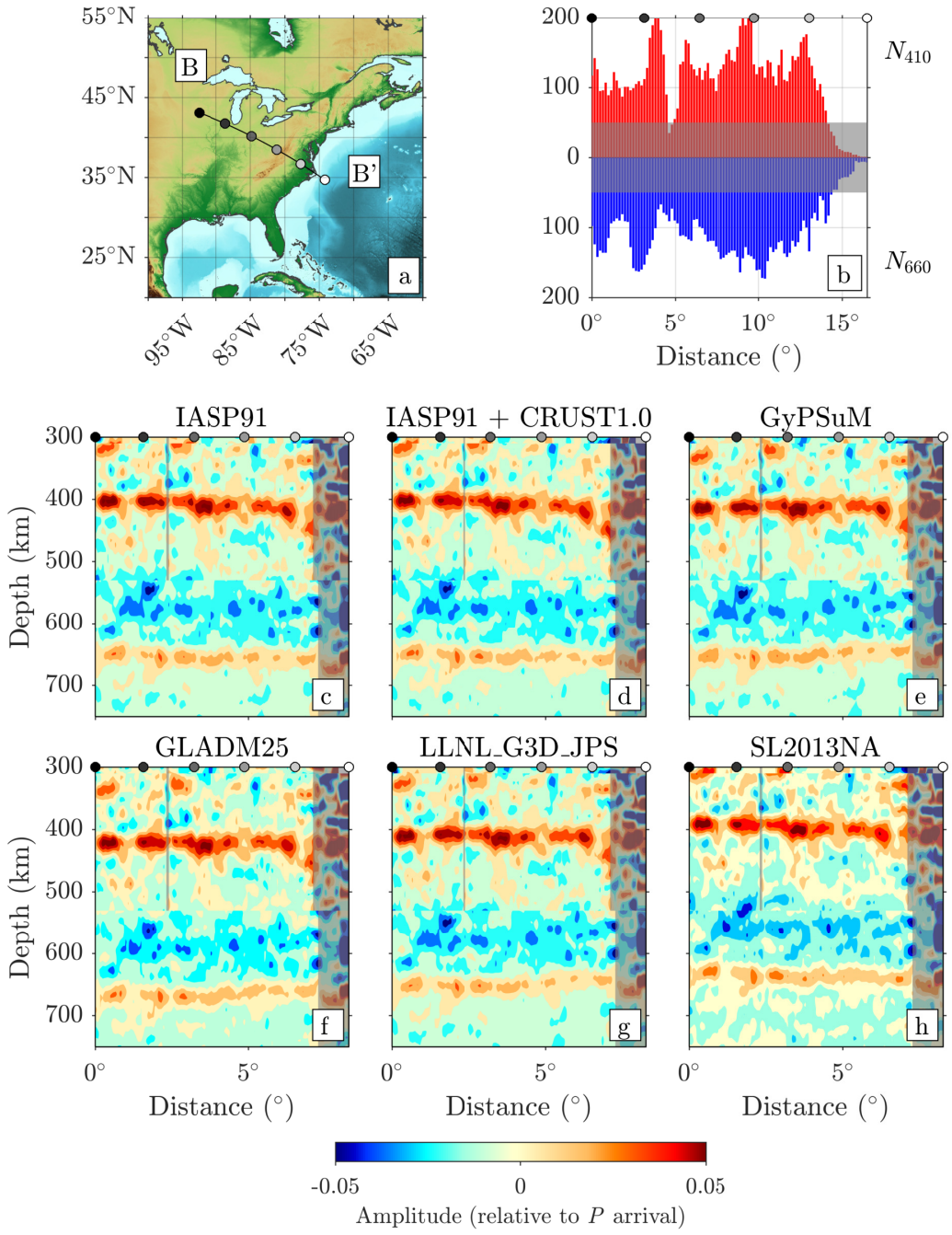


Figure 4.5: Same as Figure 4.4, but for a cross section taken along the CAA (a). Note the considerable amount (c-h) of topography on the 410 discontinuity, and the strong thinning of the MTZ in the SE end of the cross section. Also note (b) the data sparsity and poor resolution at the southeasternmost end of this cross section.

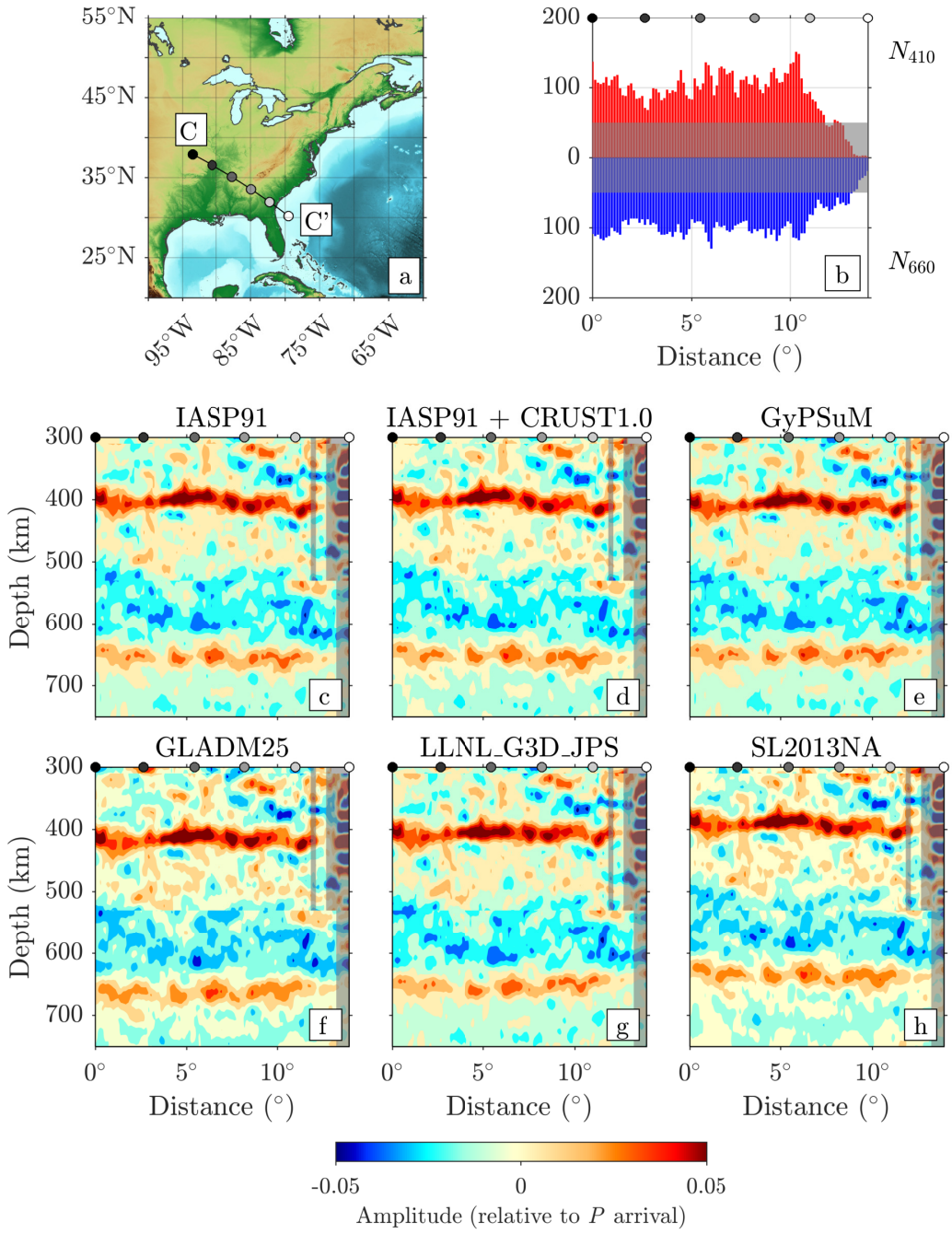


Figure 4.6: Same as Figures 4.4 and 4.5, but for a cross section taken along the Southern Appalachian Anomaly (a). Once again, note the strong topography (c-h) on the 410, as well as the 660 discontinuities. This cross-section shows significant thickening of the MTZ beneath the western end of the cross section (third gray dot), beneath western Tennessee. (b) Data coverage is fairly uniform alonng this cross section, with resolution tapering off at the southeasternmost end of this cross section.

thinned region east of the Appalachians, compared to the global average of 242 km (Lawrence & Shearer 2006), and a relatively thickened region to the west of the Appalachians. Of particular interest are two roughly linear thinned zones which trend NW-SE. These thinned zones correspond to cross sections A-A', B-B' (see Figures 4.1, 4.4, and 4.5). In addition, a thickened region exists beneath western Tennessee and can be seen in cross section C-C' (see Figure 4.6).

4.6 Discussion

4.6.1 The Importance of 3-D Moveout Corrections

We have shown that the choice of seismic velocity model has a considerable effect on the apparent depth of the MTZ discontinuities. In the most extreme case, an average discrepancy of 21.6 km in the apparent depth of the 410 and an average discrepancy of 26.1 km in the apparent depth of the 660 were found between CCP stacks made using models GLADM25 and SL2013NA (see Figures 4.13 and 4.14). These discrepancies are contrasted by an average difference of 4.4 km between the apparent MTZ thicknesses found in these stacks (see Figure 4.8c). This highlights that the apparent depths of the 410 and the 660 can be difficult to accurately constrain using receiver functions, even after performing 3-D depth corrections. Fortunately, the MTZ thickness is much more consistently resolved regardless of the seismic velocity model used to depth convert receiver functions. Consequently, this is the feature which we will frame our discussion on, and we suggest that future MTZ receiver function studies follow this example.

In an effort to explore and understand the mechanism leading to these discrepancies, we performed an analysis of the time-to-depth conversion integral in Eq. 4.1 for each of the 3-D velocity models used in our study. The results of this analysis are summarized in Figure 4.9 of the Supplemental Materials. We found that the *Pds*

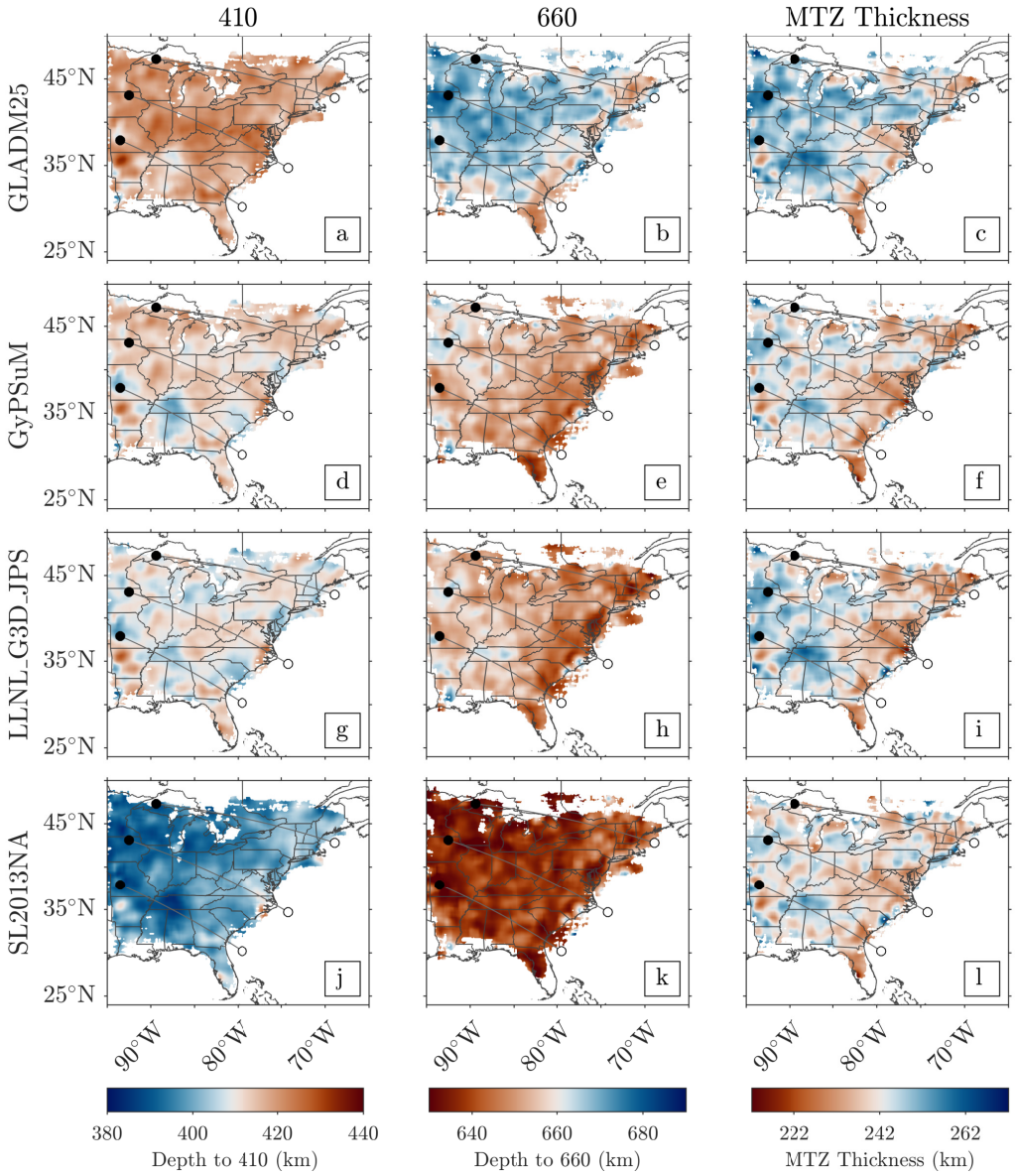


Figure 4.7: Measured 410 and 660 depths, as well as MTZ thickness, for CCP stacks made using four different 3-D velocity models in the depth conversion of our receiver functions: (a-c) GLADM25, (d-f) GyPSuM, (g-i) LLNL_G3-D_JPS, and (j-l) SL2013NA. Only locations with 50 or more receiver functions are shown. Note that models GLADM25 and SL2013NA differ markedly in the depths of the 410 and 660, while GyPSuM and LLNL_G3-D_JPS seem more consistent with one another. Also note that all four models are fairly consistent in their resolved MTZ thickness. The thinned zones shown in cross sections A-A', B-B', and C-C' (Figures 4.4, 4.5, and 4.6) are also apparent in all four models.

conversion depth associated with a particular time in a receiver function varied considerably from the outset in each of the 3-D models. For times in the range of 0 to 10 s after the P arrival in the receiver function, there is a spread in possible conversion depths of roughly 4 km. This would lead to relative discrepancies in apparent Moho depths on the order of 4 km. At times greater than 20 s, this discrepancy has grown to roughly 20 km, as can be seen in our results. The slopes of these curves, however, remain roughly constant through the times associated with MTZ Pds arrivals, which leads to the decreased variability in our observed MTZ thicknesses using different tomographic models.

4.6.2 The Northern Appalachian Anomaly

In light of the previous discussion, we are confident that the observed MTZ thinning in our CCP stacks is a robust feature. This leads to interesting implications for the NAA, which had only been observed at shallower asthenospheric depths of 100 to 300 km (Menke et al. 2016, Levin et al. 2018). We suggest that this feature extends deeper than previously known, and may be associated with a surviving hot thermal anomaly beneath New England.

We can estimate the magnitude of this thermal anomaly using the following relation from Helffrich (2000):

$$z = z_0 + \delta T \left(\frac{dz}{dP}\right) \left[\left(\frac{dP}{dT}\right)_{660} - \left(\frac{dP}{dT}\right)_{410}\right], \tag{4.2}$$

where z represents the observed MTZ thickness, $(dP/dT)_{660}$ and $(dP/dT)_{410}$ are the Clapeyron slopes of the ringwoodite to bridgmanite and magnesiowüstite (ferropericlase) phase transition, and the olivine to wadsleyite phase transition, respectively. We use a value of $z_0 = 242$ km (Lawrence & Shearer 2006) for the global average MTZ

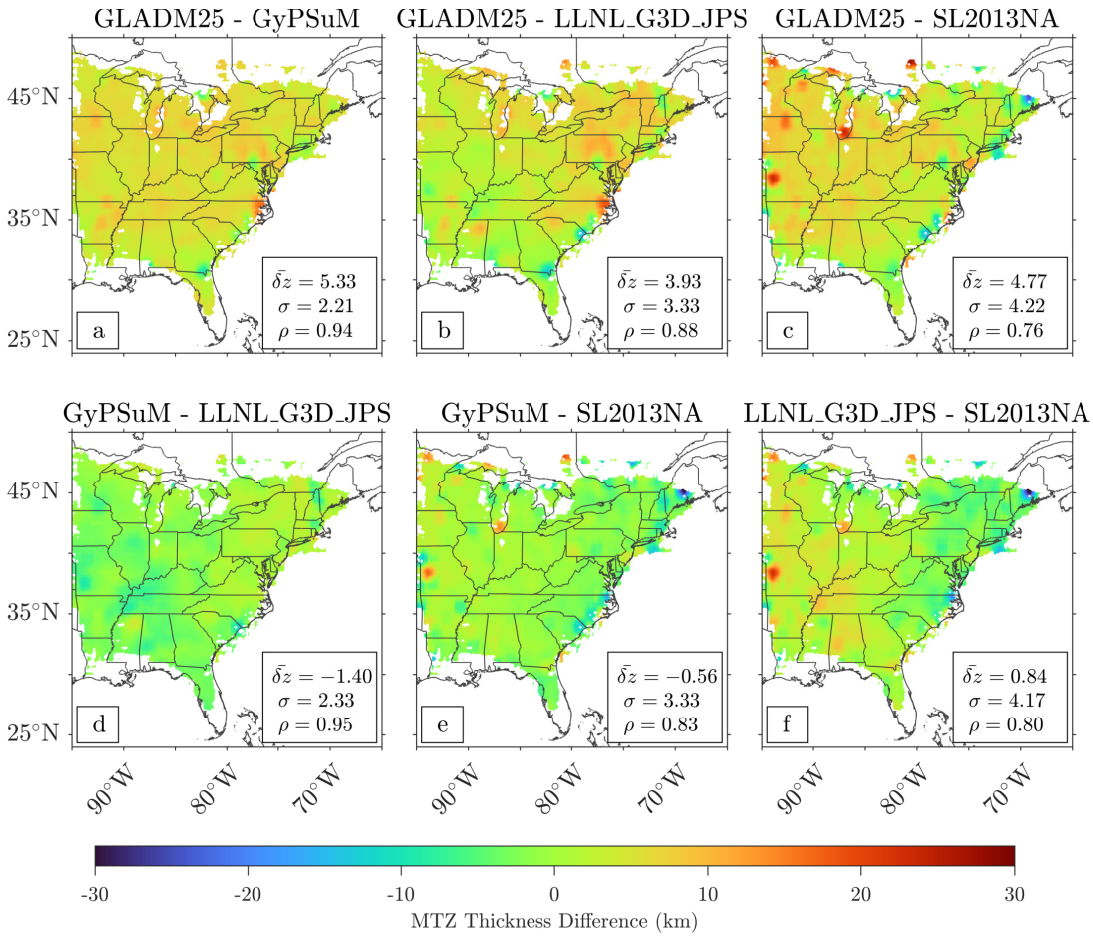


Figure 4.8: (a-f) Maps showing the differences between pairs of each of the MTZ thickness maps in Figure 4.7. The inset boxes report $\bar{\delta z}$, the mean value of the difference, σ, the standard deviation of the difference, and ρ, the correlation coefficient between the two maps. Note that the differences in thickness are on the order of a few kilometers, and that the maps tend to be well correlated ($\rho > 0.7$). For similar maps showing the differences for the 410 and the 660, the reader is referred to Supplementary Figures 4.13 and 4.14.

thickness, and values of $(dP/dT)_{660} = -2.6$ MPa/K and $(dP/dT)_{410} = 3.1$ MPa/K (Akaogi et al. 2007) for the Clapeyron slopes.

Using our four different CCP stacks, we can estimate bounds on the thermal anomaly associated with the NAA. The minimum MTZ thickness observed in our four models is 223 km (model LLNL_G3-D_JPS, beneath southern New Hampshire), but there is a range of 6 km across the models in this measurement (229 km for

model GLADM25, see Figure 4.10). Inserting these values into Eq. 4.2 gives a range for the maximum thermal anomaly of ∼89–130 K relative to global average MTZ temperature. To investigate the significance of this anomaly, we measured certain statistics of the NAA sub-region relative to our entire dataset (see Table 4.1). We found that the average MTZ thickness within the NAA was between 235 and 238 km for the four models we tested, corresponding to a modest thermal anomaly of ∼27–48 K relative to the global average. This thickness is roughly one standard deviation thinner than the average for our entire dataset.

Previous receiver function research on the MTZ beneath the NAA found no evidence of thinning or deflection of the discontinuities (Li et al. 1998). This has led recent work to suggest that this feature does not penetrate through the MTZ, and is instead confined to the shallow asthenosphere at depths less than 400 km (Menke et al. 2016). Our findings do not invalidate this previous work, but instead build upon it by suggesting that the NAA may weakly penetrate the MTZ below. In fact, if we consider the MTZ to be the lowermost extent of a shallow edge-driven convective cell, the observations of W-E aligned anisotropy can be interpreted as the horizontal flow associated with the bottom of such a cell (Long et al. 2016, Levin et al. 2018). This could reconcile the puzzling observations of null splitting and W-E anisotropy beneath the NAA which stand as outliers to the rest of northeastern North America (Li et al. 2019).

4.6.3 The Central Appalachian Anomaly

We can apply a similar analysis to the anomalously thin MTZ corresponding to the CAA to get an estimate of the magnitude of its thermal signature. The minimum MTZ thickness we observe is 214 km (model LLNL_G3-D_JPS beneath the North Carolina-Virginia border), but there is a range of 14 km across the four models (228 km in models GLADM25 and SL2013NA, see Figure 4.11). This yields a range

of ∼96–192 K for the maximum thermal anomaly relative to global average MTZ temperature. Similar to the NAA, the average MTZ thickness within the CAA is between 236 and 238 km, corresponding to an average thermal anomaly of ∼27–42 K relative to the global average.

When we consider all of the information presented so far, the CAA and NAA seem to be very similar in terms of their observed features. Both locations have records of igneous activity within the last 150 Myrs, and the present day MTZ anomalies are of nearly identical magnitudes. We suggest that both of these features may be associated with small scale convective cells generated by the contrast with the nearby Farallon slab remnants and continental craton. These cells seem to be long-lived, and may have been present during the passage of both the Great Meteor and Bermuda hotspots, providing them with the additional heat and buoyancy required to initiate active volcanism and plutonism. This interpretation is consistent with null splitting observations in both regions (Long et al. 2016), and with an edge-driven convection model (King & Anderson 1998). Perhaps with the passage of another transient heat source these regions would become active again.

4.6.4 MTZ Thickening Associated with the Laramide Slab

In addition to resolving regions of thinned MTZ beneath the NAA and CAA, we observe modest topography and thickening of the MTZ west of the Appalachians. Of particular note is a significantly thickened patch beneath western Tennessee, which we argue is associated with the stagnant Laramide slab. The Laramide slab is not an entire, distinct slab, but is rather the expression of a period of shallow angle subduction of the Farallon slab which occurred 80 to 60 Ma (Humphreys et al. 2015). This shallow subduction was terminated by a break-off at depth and a westward migration of the trench around 50 Ma (Sigloch et al. 2008), leaving the shallowly subducting slab stalled in the transition zone. Recent tomographic images support this inter-

pretation, showing evidence of shallow (< 700 km) seismically fast anomalies in the transition zone beneath the Midwest (Sigloch 2011). In the model of Sigloch (2011), these anomalies are greatest in the MTZ beneath western Tennessee, consistent with our observations of maximum thickening there.

To quantify the magnitude of the thermal anomaly associated with this relict slab, we measure the maximum MTZ thickness beneath this region (see Figure 4.12). We observe a maximum MTZ thickness of 263 km (beneath western Tennessee in model GLADM25), and a range of 6 km for the maximum thickness (257 km in models GyPSuM and SL2013NA). These values correspond to a range of about −103 K to −144 K for the maximum cold thermal anomaly relative to global average MTZ temperature. The average MTZ thickness within this anomaly spans a range of 245 to 249 km, and corresponds to an average thermal anomaly of about −21 K to −48 K relative to the global average. These anomalies are smaller than those observed beneath active subduction zones at present (van Stiphout et al. 2019), but this is not surprising considering how long the Laramide slab has been stalled in the MTZ.

4.7 Conclusion

We have performed an extensive analysis of the structure of the MTZ beneath eastern North America, and have developed and provided a methodological approach by which to do so. Specifically, we have found that the choice of velocity model used to depth-convert receiver functions can lead to significant variations in the observed depths of the 410 and 660 km discontinuities. The overall MTZ thickness, however, is found to be less sensitive to the differences in velocity models, and is therefore a more robust feature when it comes to interpreting receiver function results in their respective geologic and geodynamic contexts. With this in mind, we explored a variety of significant features in our dataset: notably, the NAA, CAA, and Laramide

slab anomaly. These features correspond to positive and negative thermal anomalies on the order of ±100 K, which may seem modest beneath an active margin or mantle plume, but are noteworthy considering the current status of the region as a passive margin. These observations enhance our understanding of the NAA and CAA, suggesting that they may penetrate into the MTZ instead of being solely confined to shallow asthenospheric depths. Our observations of the stagnant Laramide slab provide additional evidence for slabs stalling in the MTZ, and reinforce the theory of the Farallon slab's two-stage subduction.

4.8 Acknowledgments

The computer code developed for this work, `rflexa` (Burky et al. 2021*a*), is available online at: `https://github.com/alexburky/rflexa`. We acknowledge the use of the Seismic Analysis Code (SAC) Version 101.6a (Goldstein & Snoke 2005). Data for this study were provided by the IRIS DMC (doi: 10.7914/SN/TA). This work was partly supported by the U.S. National Science Foundation (NSF) under grants EAR-1736046 and OCE-1917085, and by Princeton University. High-performance computing resources were provided by the Princeton Institue for Computational Science & Engineering (PICSciE).

4.9 Supplement

The following seven figures and one table are a supplement to the main text. Each of the figures is referenced in the main text, and a thorough description of each figure is provided in the figure captions. The animations mentioned in the main text can be found on the website where the original paper is published.

Summary of MTZ Thickness Observations				
	GLADM25	GyPSuM	LLNL_G3D_JPS	SL2013NA
$\bar{z} + 2\sigma$	259	253	256	252
$\bar{z}$	246	241	242	241
$\bar{z} - 2\sigma$	233	229	228	230
Northern Appalachian Anomaly				
$\bar{z} + 2\sigma$	245	244	244	243
$\bar{z}$	238	236	235	238
$\bar{z} - 2\sigma$	231	228	227	232
δz_{min}	229	224	223	227
Central Appalachian Anomaly				
$\bar{z} + 2\sigma$	244	244	245	243
$\bar{z}$	238	236	236	237
$\bar{z} - 2\sigma$	233	228	227	231
δz_{min}	228	216	214	228
Laramide Slab Anomaly				
δz_{max}	263	257	262	257
$\bar{z} + 2\sigma$	257	251	256	251
$\bar{z}$	249	246	248	245
$\bar{z} - 2\sigma$	240	240	240	240

Table 4.1: Summary of the MTZ thickness observations from our study. The top of the table summarizes the entire dataset, and the following three sections summarize measurements of the NAA, CAA, and Laramide Slab Anomaly. For the NAA and CAA, the statistics are measured for areas below the 242 km contour line in the regions enclosed by Figures 4.10 and 4.11, and areas above the 242 km contour line in the region enclosed by Figure 4.12 are used for the Laramide Slab Anomaly. $\bar{z}$ is the mean MTZ thickness, and σ is the standard deviation. Note that the minima and maxima associated with all three anomalies are outside of the 2σ range.

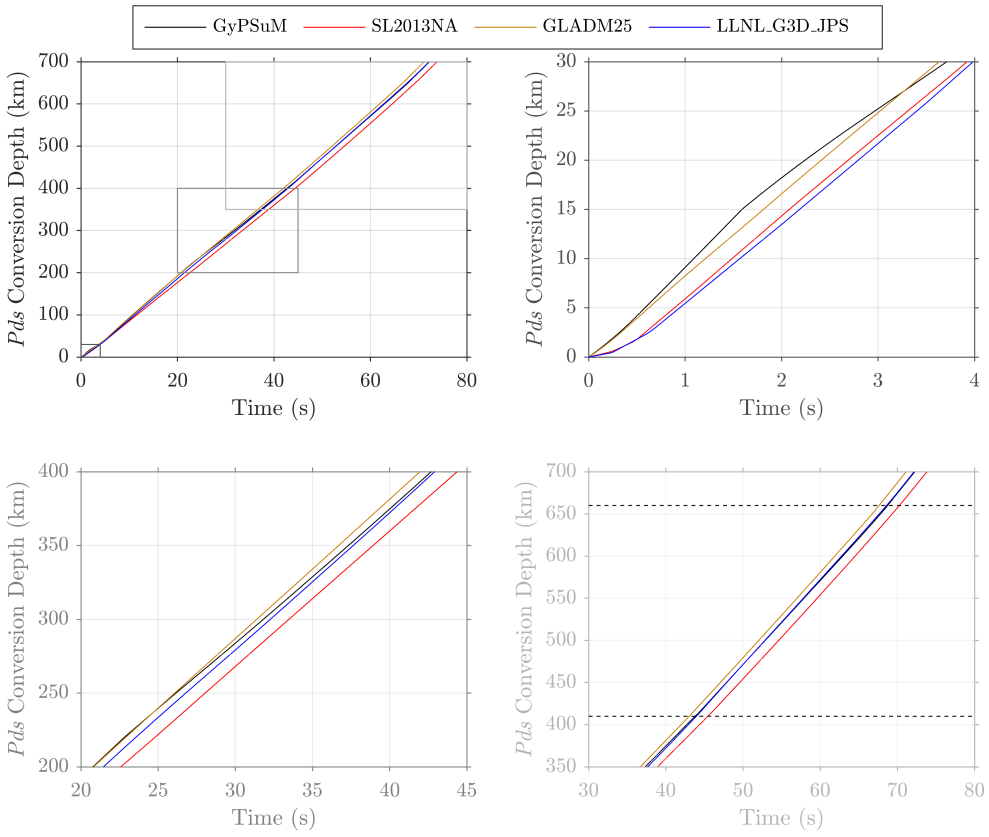


Figure 4.9: Plots showing the relationship between *Pds* conversion depth and time relative to the main *P* arrival in an individual receiver function. These relationships are shown for the four different choices of 3D velocity model used in our study, and are used to transform receiver functions from the time-domain to the depth-domain. To illustrate how to comprehend these plots, the reader's attention is drawn to the top-right panel. A peak 1 s after the main *P* arrival would be mapped to a depth of $\sim$ 5 km using models LLNL_G3D_JPS and SL2013NA, but would be mapped to a depth of $\sim$ 9 km with models GLADM25 and GyPSuM. The behavior of these curves in the lower-right panel explains the spread in the 410 and 660 depths seen in Figure 4.7 of this chapter. Since these curves are essentially parallel through the MTZ, the measured MTZ thickness is consistent regardless of the chosen model.

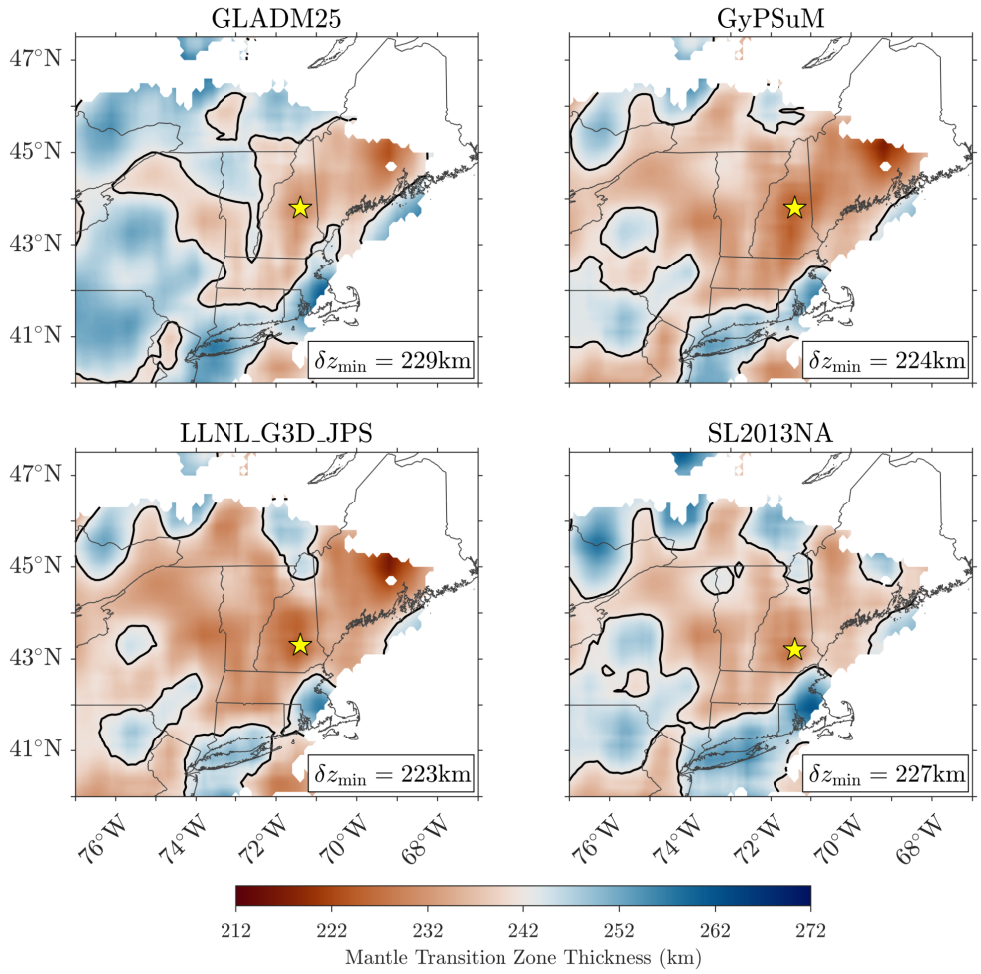


Figure 4.10: Maps showing the measured MTZ thickness in the region corresponding to the Northern Appalachian Anomaly (NAA). The star indicates the location of the minimum measured thickness, which is used in this chapter to estimate the upper limit on the magnitude of the potential thermal anomaly. We have restricted this measurement to be reasonably far from the edges of this region where data coverage is less robust. The measured thickness is indicated in the inset boxes by $\delta z_{\min}$. The solid black contour lines denote the 242 km level, which corresponds to the global average MTZ thickness (Lawrence & Shearer 2006).

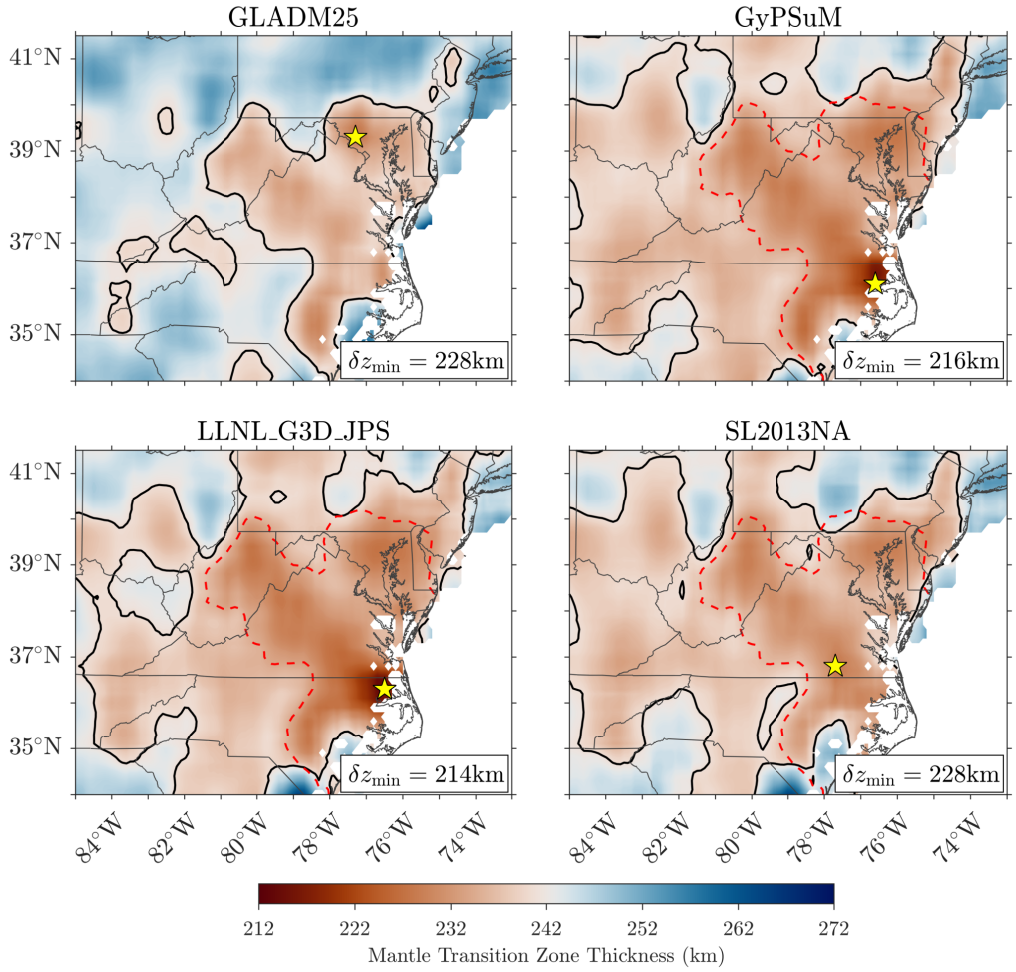


Figure 4.11: Same as Figure 4.10, but for the Central Appalachian Anomaly (CAA). However, the black contour line is drawn at 241 km to better highlight the feature in model GLADM25. Note that the thinning is more pronounced when depth-converting with models GyPSuM and LLNL_G3D_JPS, consistent with Figure 4.10. The extent of the anomaly is consistent beneath Maryland, Virginia, and eastern West Virginia across all four models. This can be seen from the contour extracted from model GLADM25 (dashed red lines) overlain on the other three models.

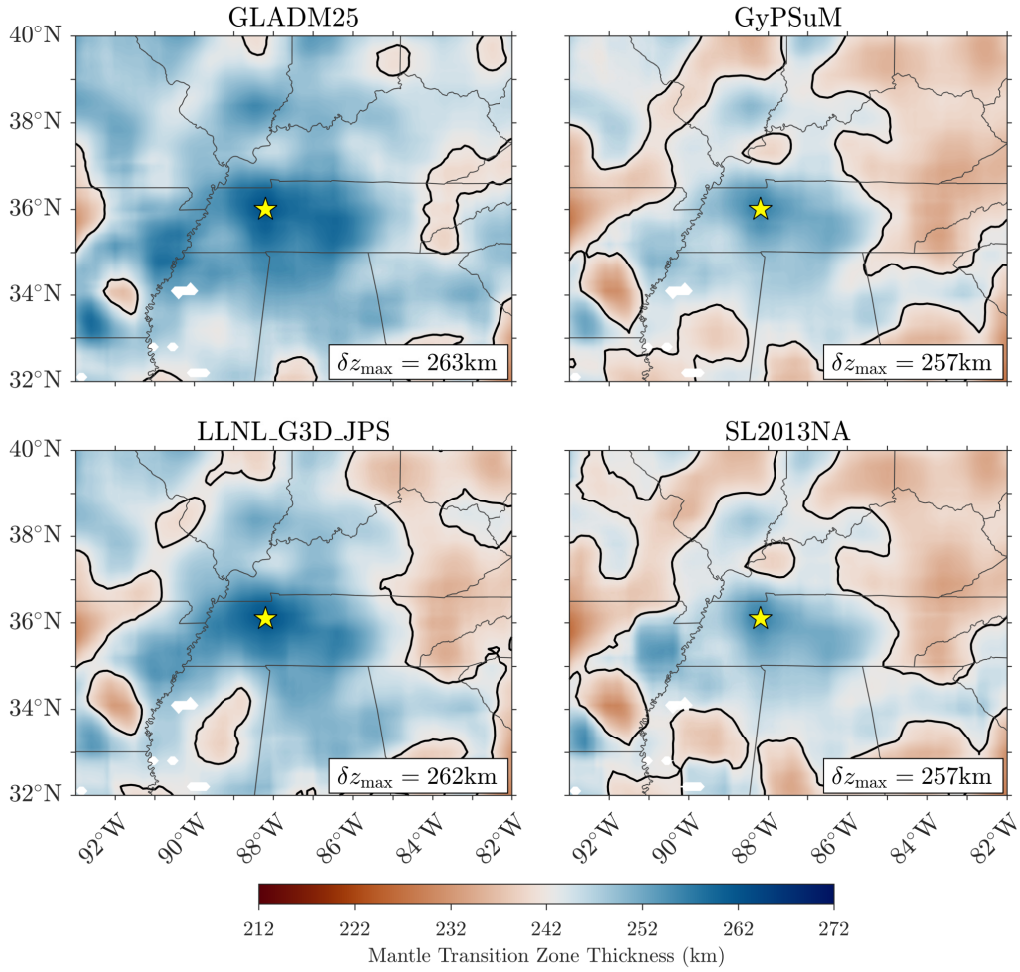


Figure 4.12: Same as Figure 4.10, but for the thickened MTZ anomaly beneath western Tennessee. Note that the location of the maximum thickness is consistent across all four models, and that the geometry of the anomaly is also roughly consistent. The range of the maximum thickness anomaly is fairly small between all four models (6 km variation).

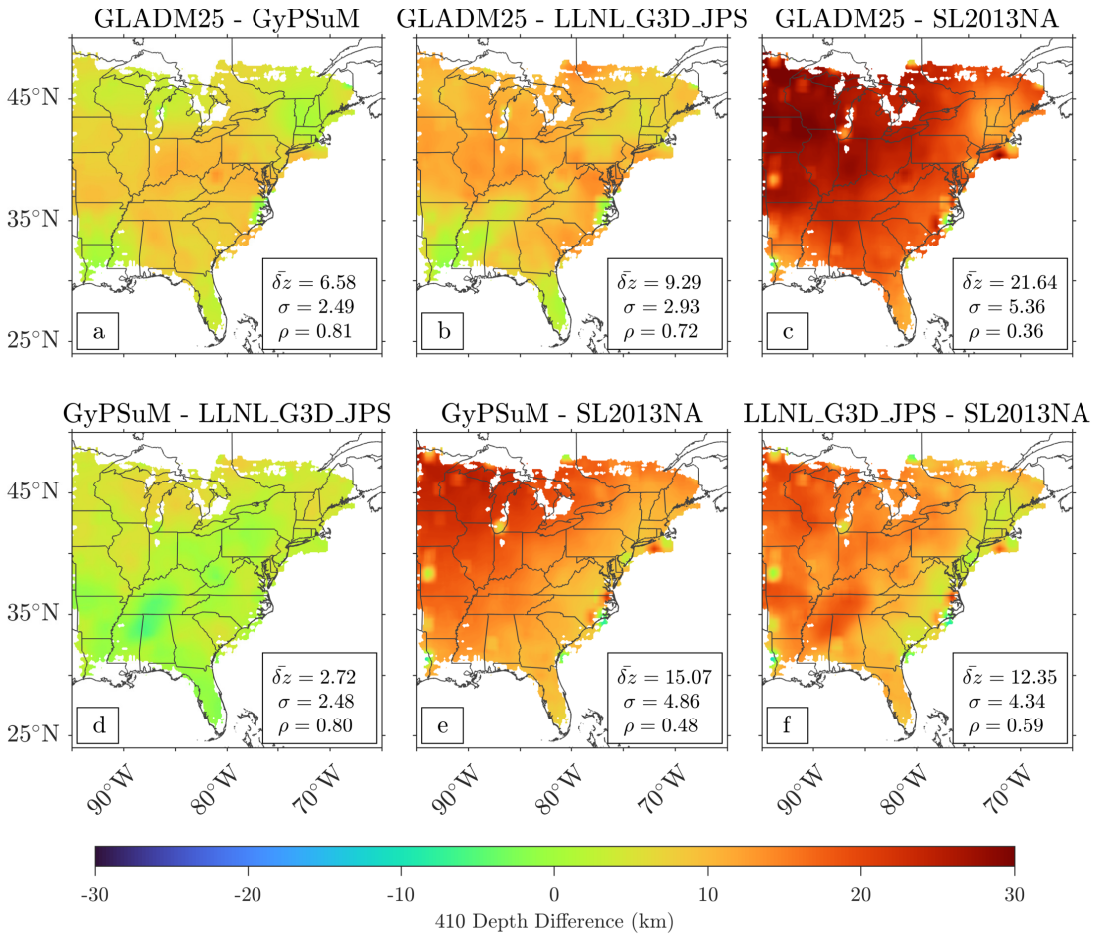


Figure 4.13: Same as Figure 4.8 of this chapter, but showing differences in the 410 between each pair of models. Note that the average differences ($\bar{\delta z}$) between models are greater than they were for the MTZ thickness. The correlation coefficients (ρ) are consistently smaller than they were for the MTZ thickness, reinforcing the idea that the MTZ thickness is a more robust measurement than the absolute depth of the 410.

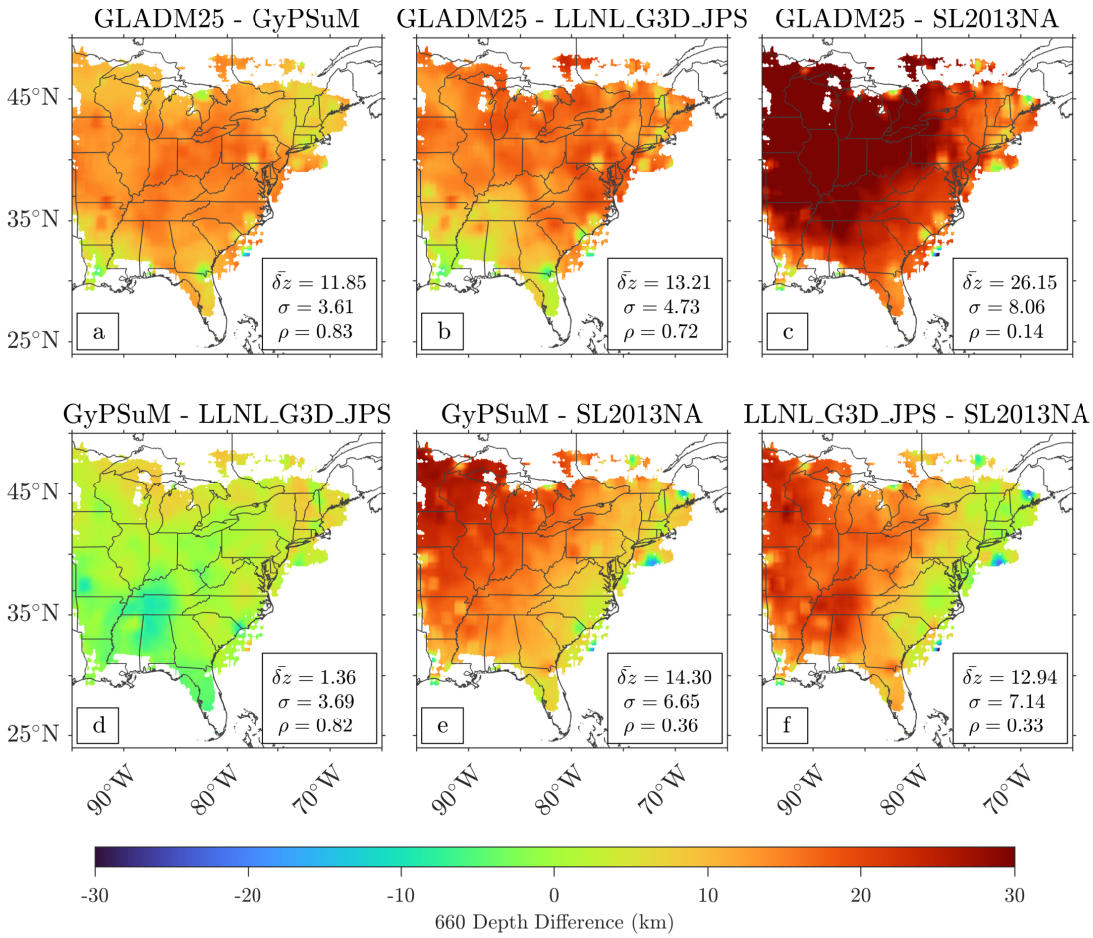


Figure 4.14: Same as Figure 4.13, but for differences in the 660 between each pair of models. Once again note the smaller correlation coefficient between models compared to that found for the MTZ thickness. Model SL2013NA in particular shows very poor correlation with the other three models.

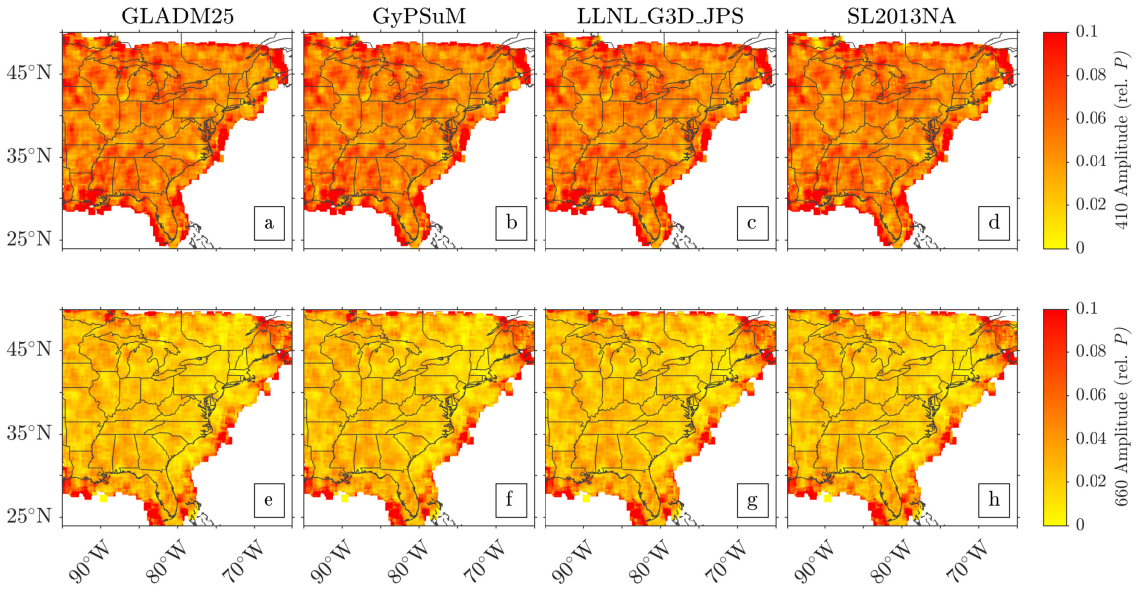


Figure 4.15: Maps showing the average measured amplitude of the 410 and 660 signals relative to the main P arrival (defined as 1). Note that the 410 signal is consistently larger than the signal from the 660. This can also be seen in the cross-sections shown in Figures 4.4-4.6 of this chapter.

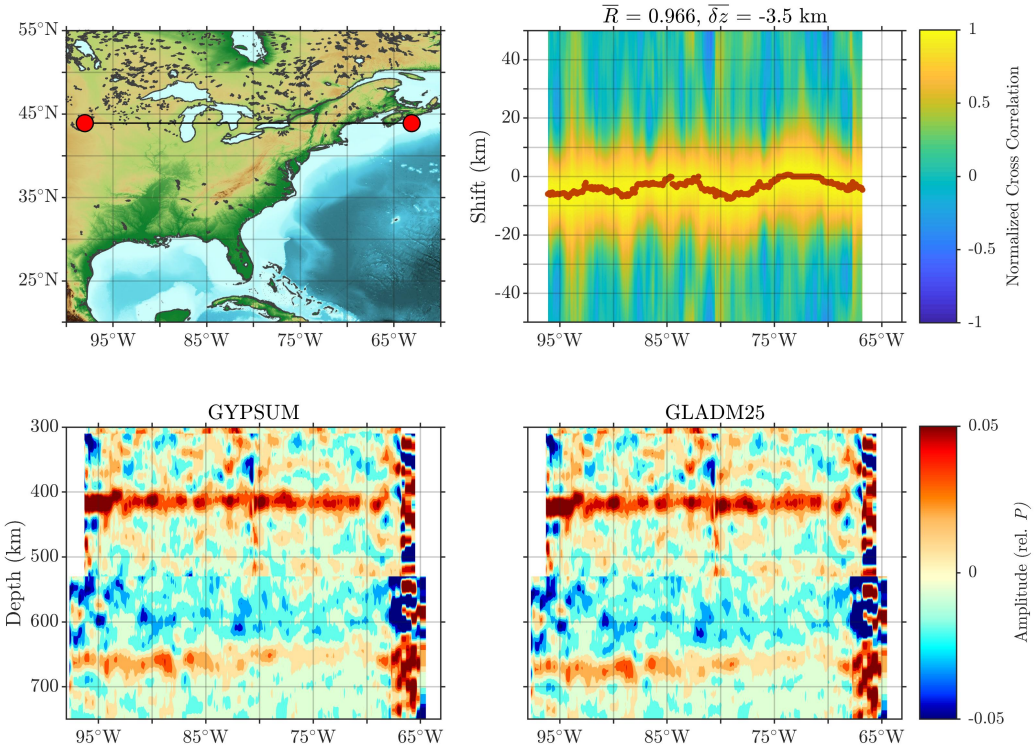


Figure 4.16: Snapshot from the supplemental videos showing the cross correlation between two CCP stacks. The bottom panel shows the CCP stacks, and the top right panel shows the cross correlation of the two stacks. The red line indicates the maximum of the cross correlation at each longitude point. $\bar{R}$ is the average value of the correlation coefficient, and $\bar{\delta z}$ is the average value of the shifts indicated by the red line. For all of the different CCP stacks, the correlation coefficient tends to be high, but there is a great deal of variability in the relative shifts of the stacks $\bar{\delta z}$.

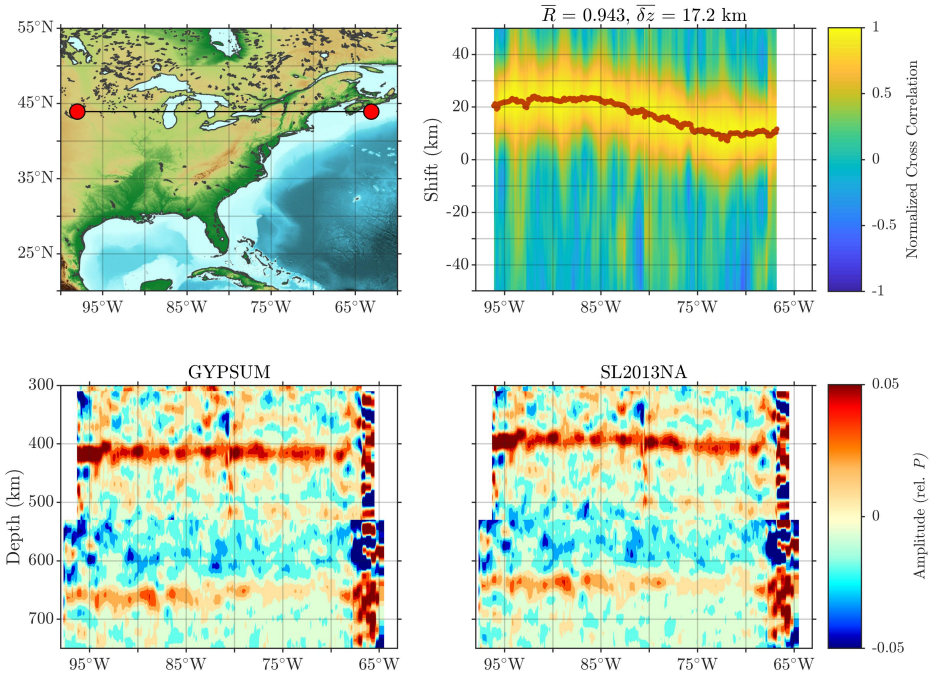


Figure 4.17: Same as Figure 4.16 but for models GyPSuM and SL2013NA.

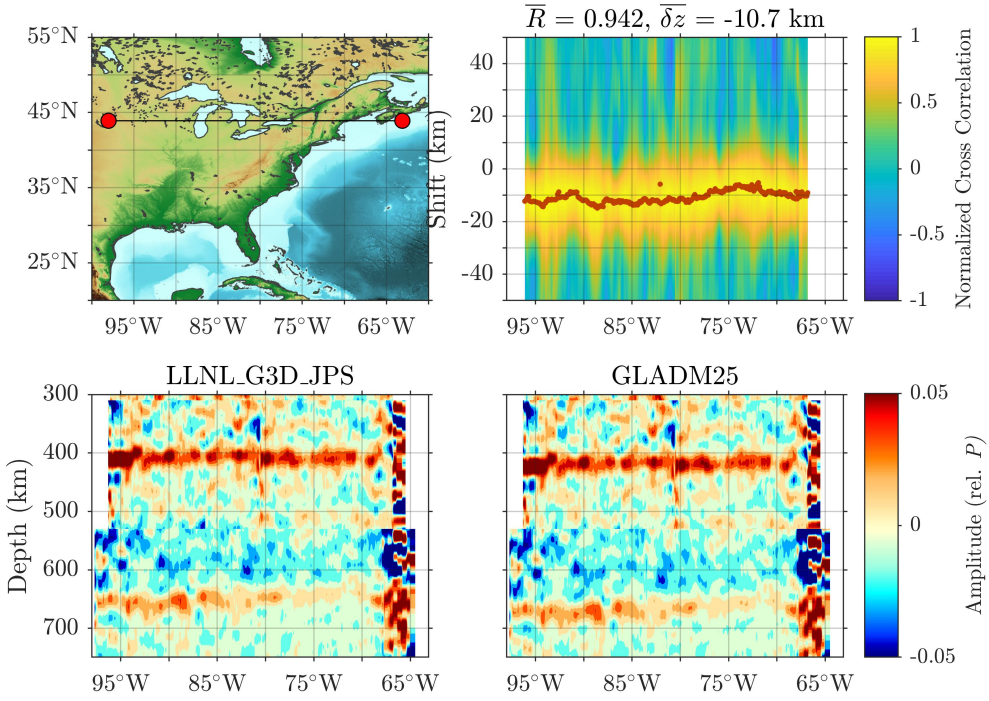


Figure 4.18: Same as Figure 4.16 but for models LLNL_G3D_JPS and GLADM25.

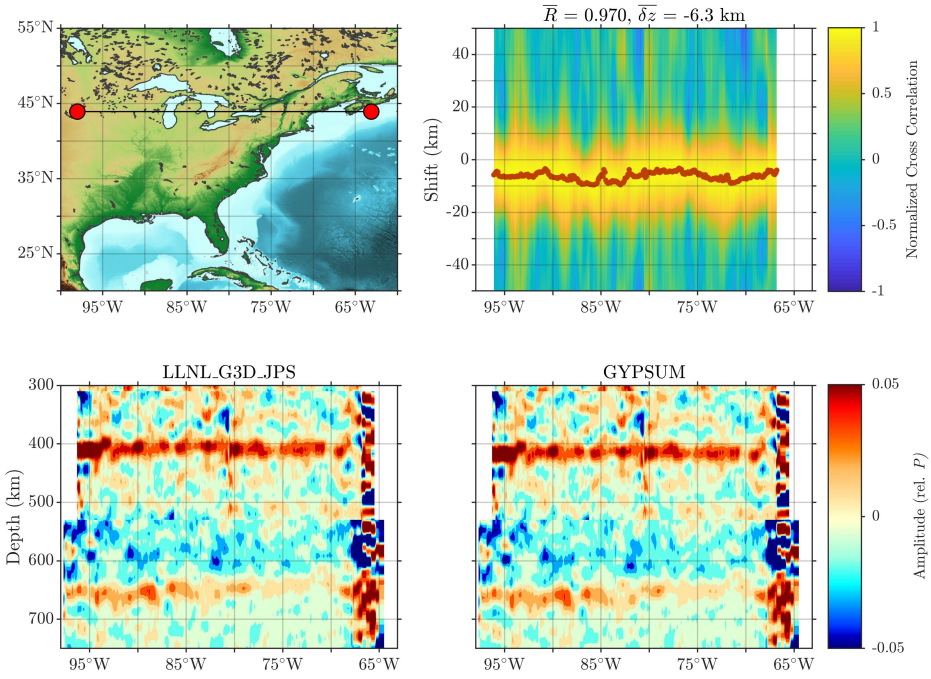


Figure 4.19: Same as Figure 4.16 but for models LLNL_G3D_JPS and GyPSuM.

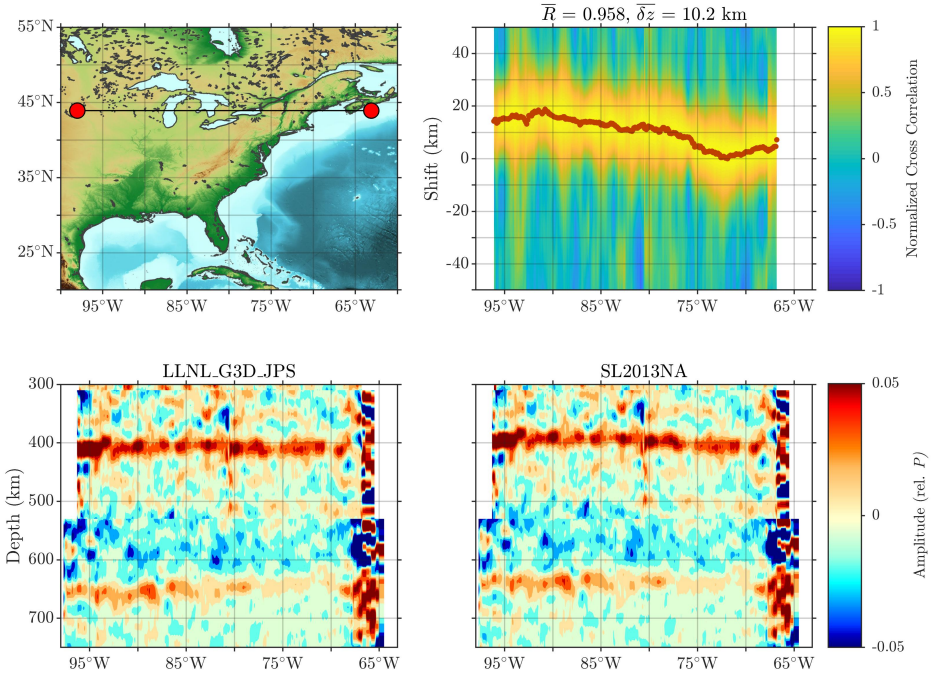


Figure 4.20: Same as Figure 4.16 but for models LLNL_G3D_JPS and SL2013NA.

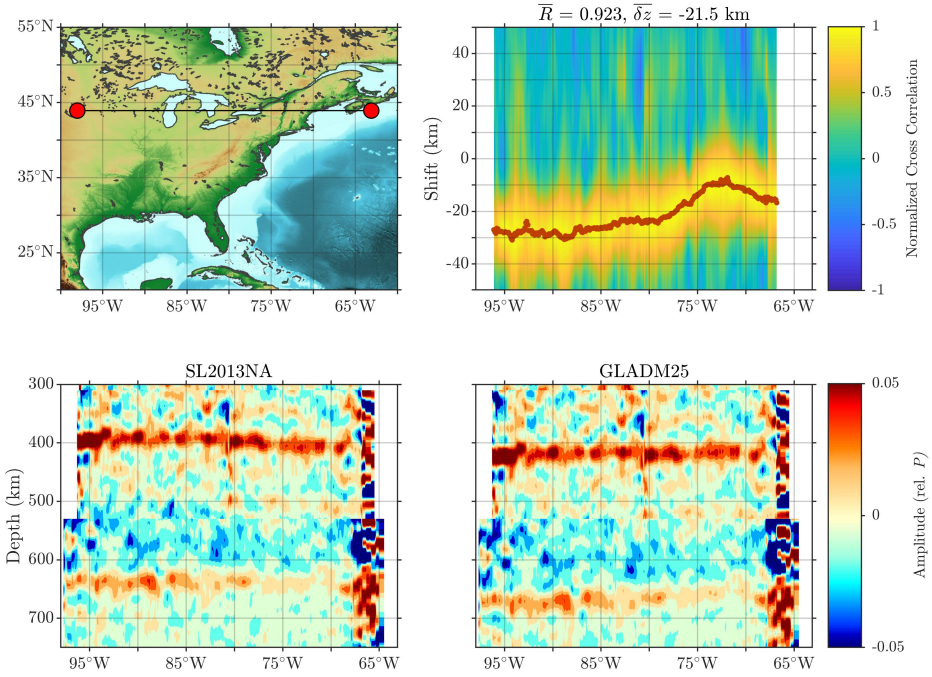


Figure 4.21: Same as Figure 4.16 but for models SL2013NA and GLADM25.

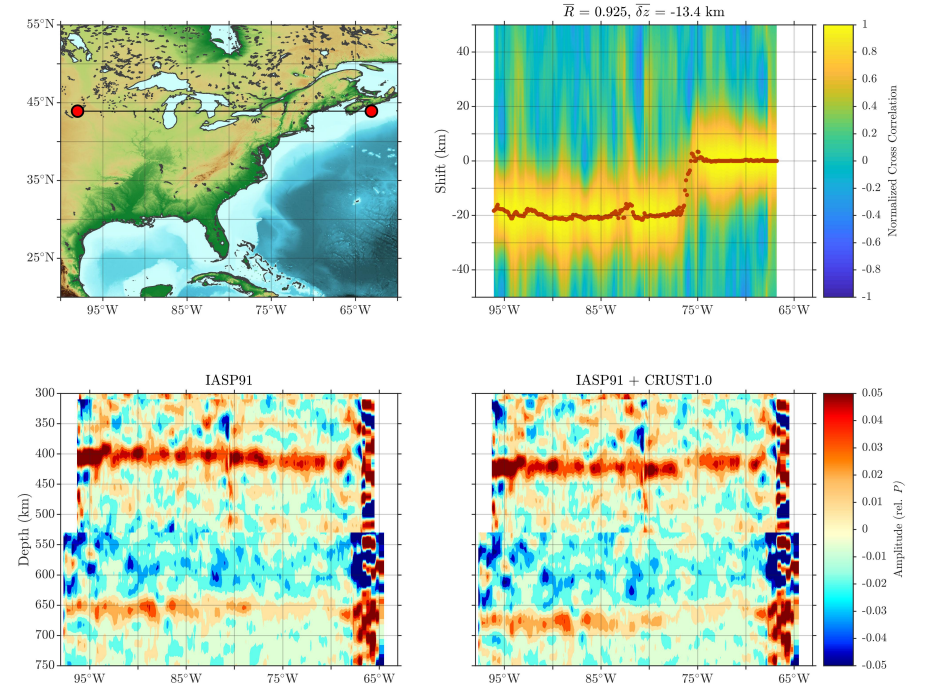


Figure 4.22: Same as Figure 4.16 but for models IASP91 and IASP91 + CRUST1.0.

Chapter 5

Conclusion

5.1 Summary of Contributions

In this dissertation, we explored the geologic history and state of the mantle transition zone beneath eastern North America and the western Atlantic Ocean. Along the way, we developed a suite of software tools to perform this analysis. The first major contributions were new MATLAB and Python implementations of the instrument response removal procedure performed by the Seismic Analysis Code (SAC) (Goldstein & Snoke 2005), detailed in Chapter 2. This new software was accompanied by a thorough explanation of the underlying mathematical theory, which should prove useful to new students and researchers hoping to work with seismic data. We then developed a new quality control criterion for MTZ receiver functions in Chapter 3, and showed how it could be used in an automated workflow to image the MTZ beneath Bermuda. This development was accompanied by a comprehensive review of the theory behind the iterative time-domain deconvolution algorithm of Ligorría & Ammon (1999). Finally, we used this software to produce high-resolution images of the MTZ beneath eastern North America, resulting in a complex interpretive story which is summarized in Figure 5.1. There is clearly a lot that we still have to learn about the nature of the Earth beneath this part of the world, but perhaps now we know a little bit more than we used to.

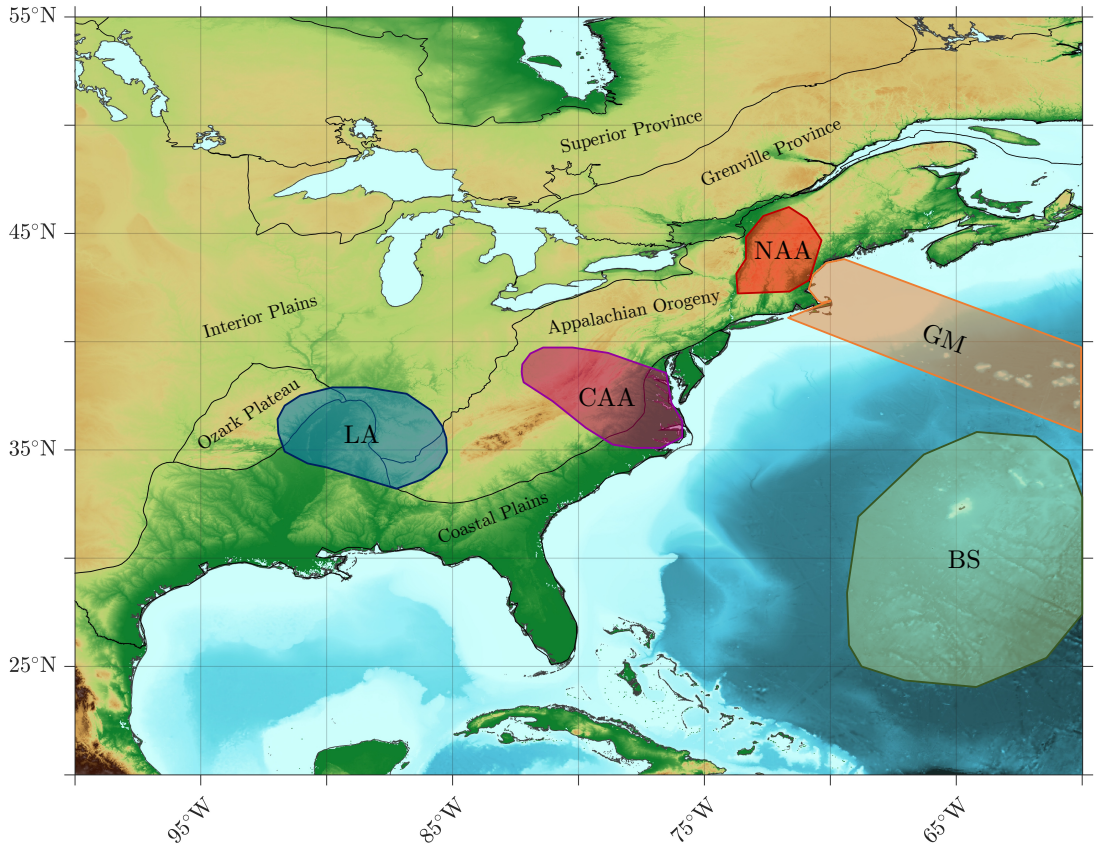


Figure 5.1: Summary map showing the tectonic provinces of eastern North America amd the western Atlantic, overlain with markers indicating the MTZ features discussed in this thesis. The labels represent, BS: Bermuda swell, CAA: central Appalachian anomaly, GM: Great Meteor hotspot track, LA: Laramide slab anomaly, and NAA: northern Appalachian anomaly, respectively. The connection between the offshore magmatic events and the Appalachian anomalies remains uncertain, and could be improved by offshore seismic deployments in the region.

5.2 Looking Forward

At the end of this dissertation, I stand in the fortunate position of having more research ideas than I had started my PhD with. This is likely the inevitable reality of the pursuit of knowledge; the more you learn, the more you realize there's still a lot you don't know. As far as research goes, there are a few pathways that would seem to be obvious starting places for subsequent work. First, an extension of the analysis performed here to a global dataset seems like a strong candidate for a rel-

atively straightforward research project. This would be a valuable stress-test of the methodology developed in this thesis, and would provide the opportunity for further software optimization. In addition, it would naturally build on the receiver function database presented in Appendix A, resulting in a valuable reference for the research community.

A second possible opportunity would be a more comprehensive investigation of receiver functions from a forward modeling perspective. We are currently in a place where high-frequency global wave propagation software (Nissen-Meyer et al. 2014) is capable of modeling the behavior of receiver functions in complex tectonic environments. It would be interesting to do a thorough comparison of the effects of plume-like and slab-like structures on receiver functions, to reinforce the interpretive results of Chapter 4. This effort could be integrated with an inversion for the topography of the MTZ discontinuities in a region.

A third, and for the sake of this discussion, final possibility would be learning an entirely new set of methods for an entirely new set of problems. To date, my work has been focused on the MTZ, but many of the methods I have learned could be used to investigate shallower features in the Earth's subsurface, such as the Moho and the lithosphere asthenosphere boundary. Receiver functions represent a tiny fraction of the methods available to observational seismologists, so it would be interesting to learn some new techniques as part of future research work. In closing, there is one thing that I am certain of at this point - tomorrow is a new day ready to be filled with new and exciting adventures.

Appendix A

Additional Figures and Data Products

A.1 Tomographic Cross Sections

This appendix contains additional figures that were made during my thesis. The first set of figures (A.1-A.3) shows cross sections through the four selected tomography models used to depth convert the receiver functions in Chapter 4, along the same profiles used there. The cross sections display the variation in shear wave speed (δV_S) relative to the average one-dimensional velocity profile of the region. To calculate this variation, the average shear wave velocity is calculated at each depth in the region of interest, and is then subtracted from the individual shear wave velocities at each point, normalized, and multiplied by 100.

Cross sections A-A' and B-B' (Figures A.1 & A.2) clearly show low velocity anomalies beneath the Northern Appalachian anomaly and Central Appalachian anomaly. These figures round out the story of Chapter 4, because they show that these features are not solely an artifact of the receiver function method that we used, since they are present in tomography models as well. It is interesting to note that this low velocity anomaly is present in all four tomography models, emphasizing the robustness of the feature. The cross section through C-C', however, shows slightly more disagreement between the four tomography models (see Figure A.3). Models

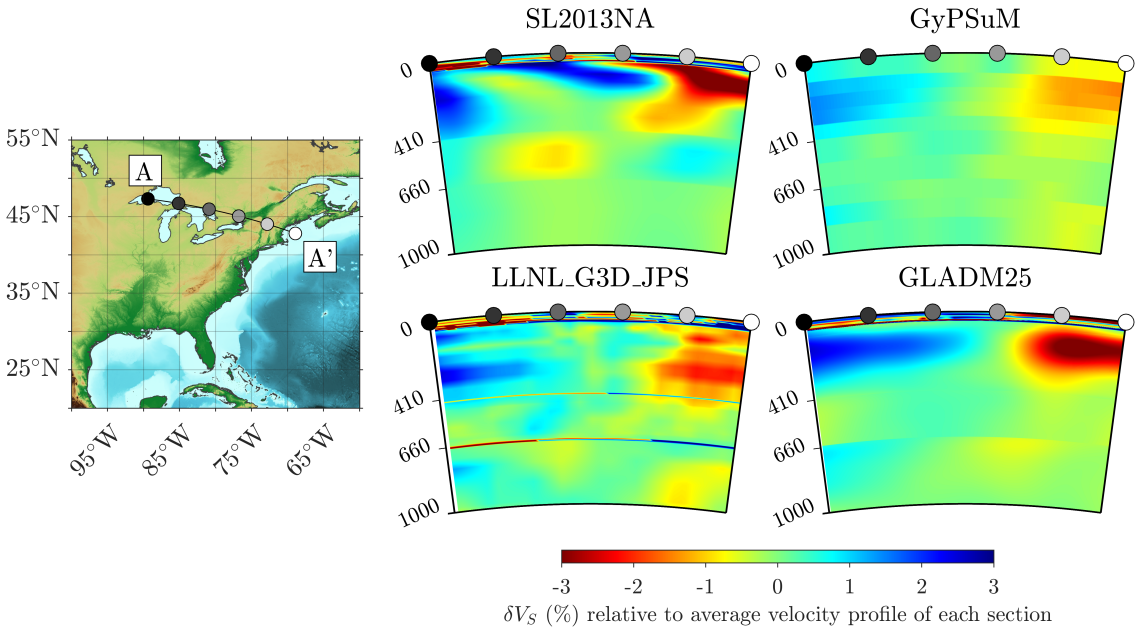


Figure A.1: Cross sections through four selected tomography models along line A-A', as in Chapter 4. Note the presence of a strong low velocity anomaly beneath New England (the NAA). The anomaly appears to be confined to the upper mantle above the MTZ, but the receiver function data suggest that it has an effect on the MTZ. Plotted is the percent variation of the S wave velocity from the average one-dimensional velocity profile of the entire cross section.

LLNL_G3D_JPS, GyPSuM, and GLADM25 show a fast anomaly in and above the transition zone coincident with the inferred location of the Laramide slab, but this feature is not resolved clearly in model SL2013NA. This is consistent with the results of Chapter 4, where the strength of this feature was diminished in the CCP stacks constructed with model SL2013NA.

Another interesting thing to note, and perhaps the subject of future investigation, is the different treatment of the MTZ discontinuities in each of these models. There are clearly discontinuous segments in each of these cross sections, and it appears that the MTZ topography is allowed to undulate in model LLNL_G3D_JPS. The strange behavior of tomographic models near discontinuities highlights the importance of the receiver function method as a means of resolving the topography on these discontinuities.

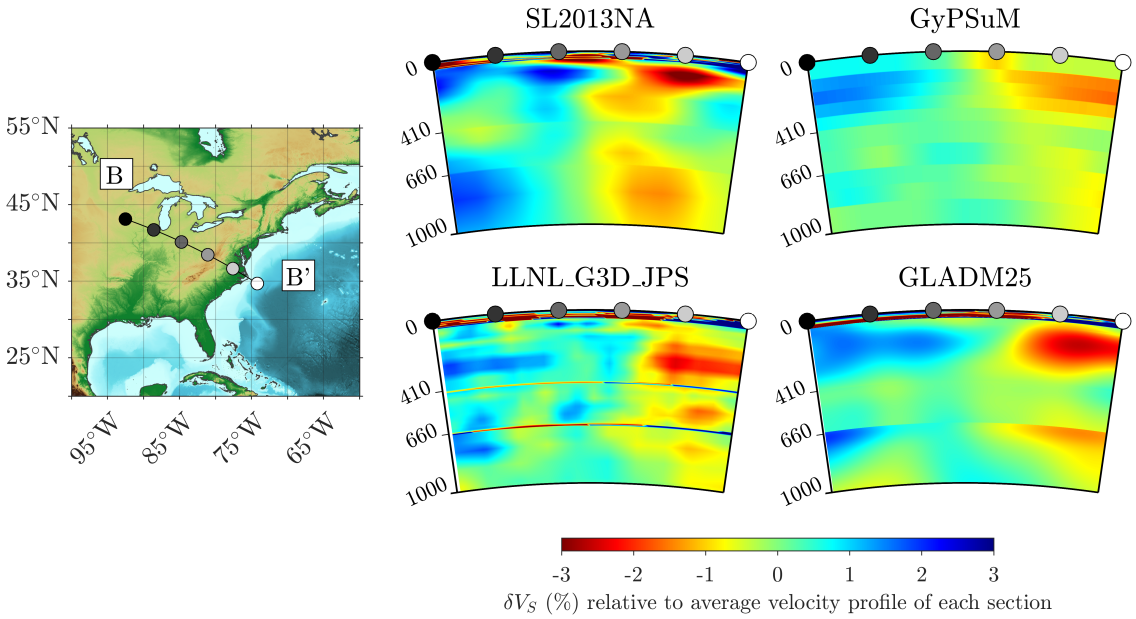


Figure A.2: Same as Figure A.1 but for cross section B-B'.

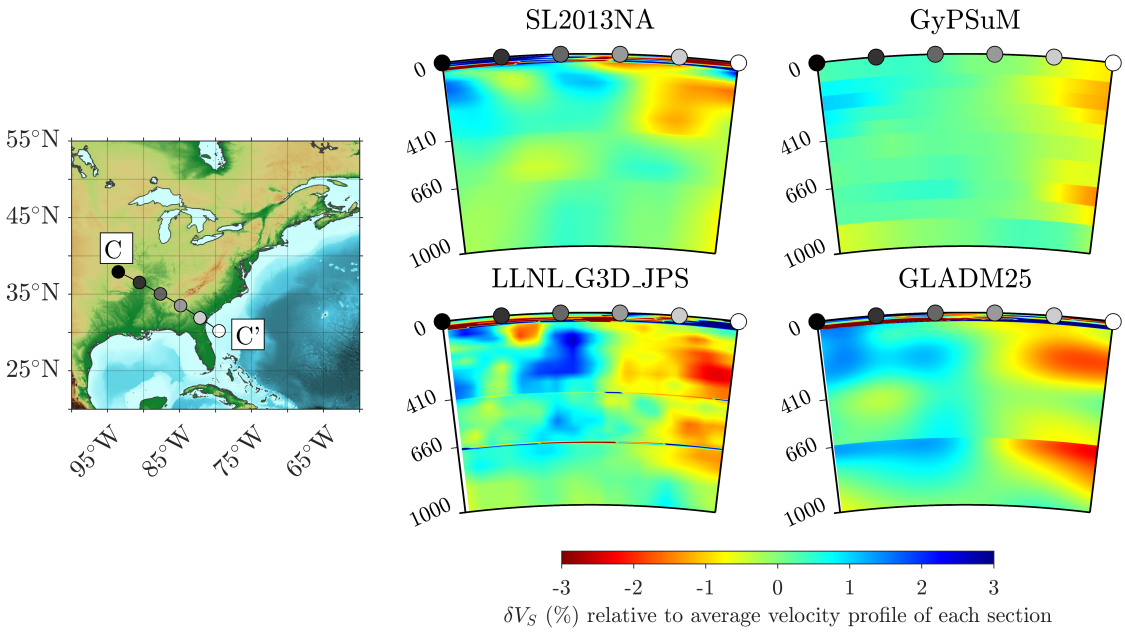


Figure A.3: Same as Figure A.1 but for cross section C-C'.

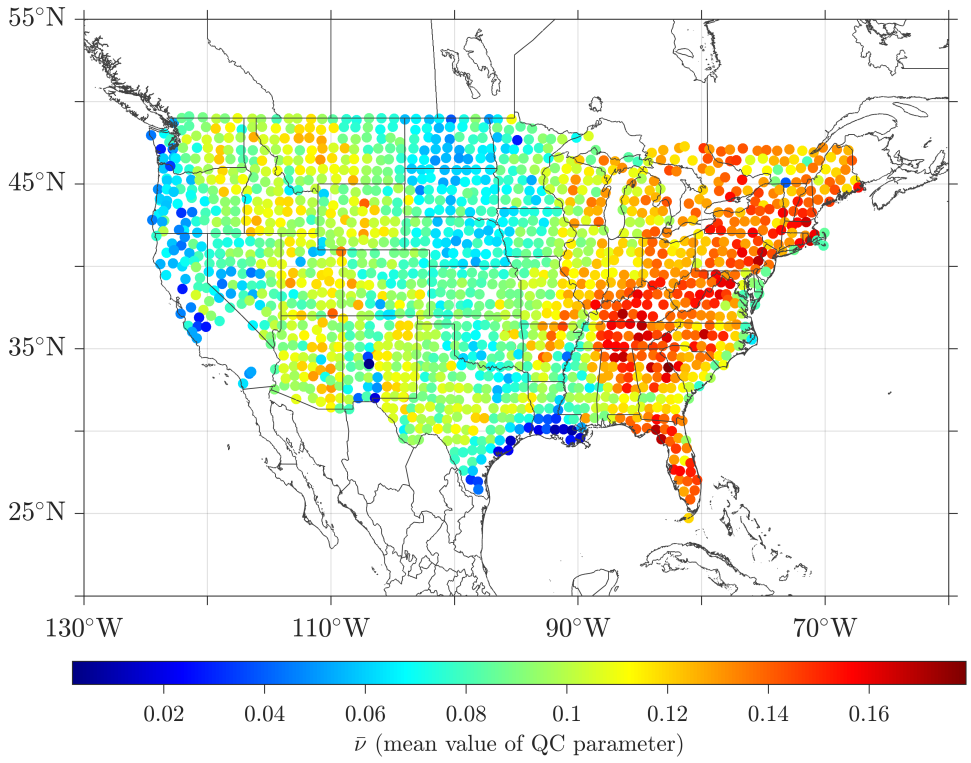


Figure A.4: Map showing the average value of ν for all of the stations in the USArray (network TA). Note the remarkable similarity to Figures A.5 and A.6. In particular, the low ν values seen in the Gulf of Mexico in Texas and Louisiana seem to correspond to the thick sediment layers shown in Figure A.6. The values of the QC parameter are very high across the Appalachians and into the Midwest, as well as in Florida. Further investigation of these features may be the subject of a future study.

A.2 Quality Control and Crustal Thickness

The second set of figures shows some characteristics of the crustal structure beneath North America, accompanied by a plot showing the average value of our quality control parameter, ν, defined in Chapter 3. The crustal thickness and sediment thickness values are taken from CRUST1.0 (Laske et al. 2013), and the average ν value was calculated as part of the work shown in Chapter 4. There appears to be remarkable similarity between the features shown in each of these figures. The thick sediment layers shown in Figure A.6 are mirrored by low $\bar{\nu}$ values in the same region, and the areas with relatively thick crust seem to mirror the areas with high $\bar{\nu}$ values. A more thorough investigation of these similarities, as well as the utility

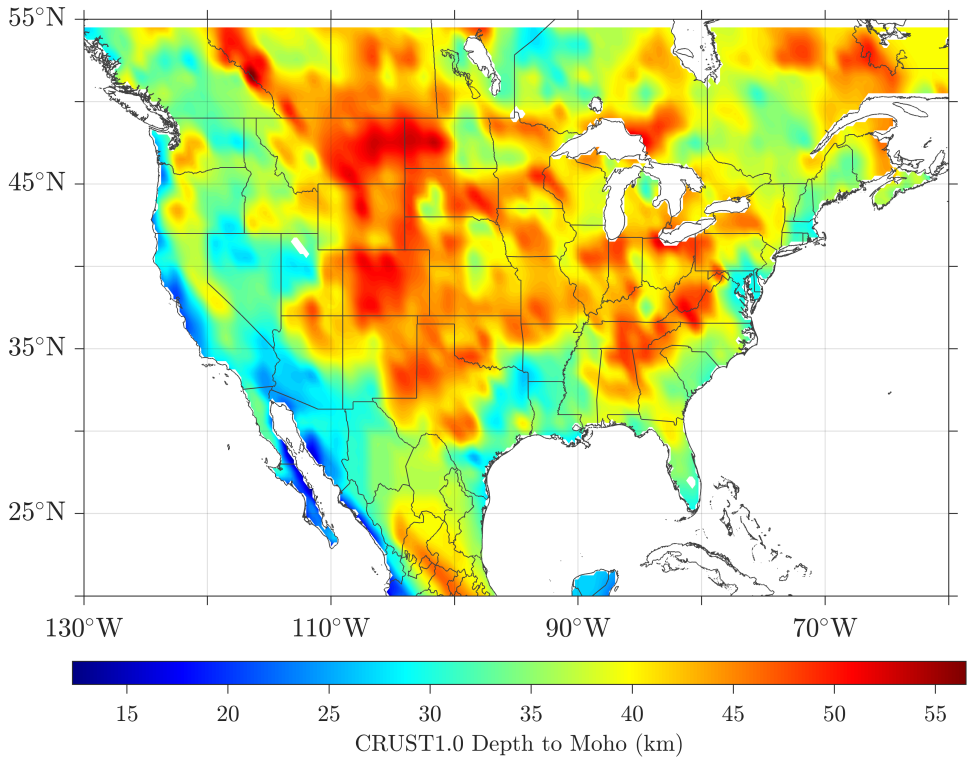


Figure A.5: Map of the depth to the Moho across North America according to CRUST1.0 (Laske et al. 2013). Note the relatively thick craton beneath much of central and eastern North America, and the relatively thin crust along the west coast and the Gulf of Mexico.

and significance of ν are the subject of ongoing work. In addition, an extension of the methods developed here are being developed for applications in shallower crustal studies using receiver functions.

A.3 The US Array Receiver Function Explorer

In the process of computing receiver functions for eastern North America, we compiled a database of single-station MTZ receiver function stacks and accompanying statistics. Summary plots from this dataset can be explored interactively online at: `https://aburky.mycpanel.princeton.edu/usarray/us_array.php`. This web-based tool allows the user to pan and zoom across a map of North America, and all of the available stations are indicated on the map with red triangles (see Figure A.7.

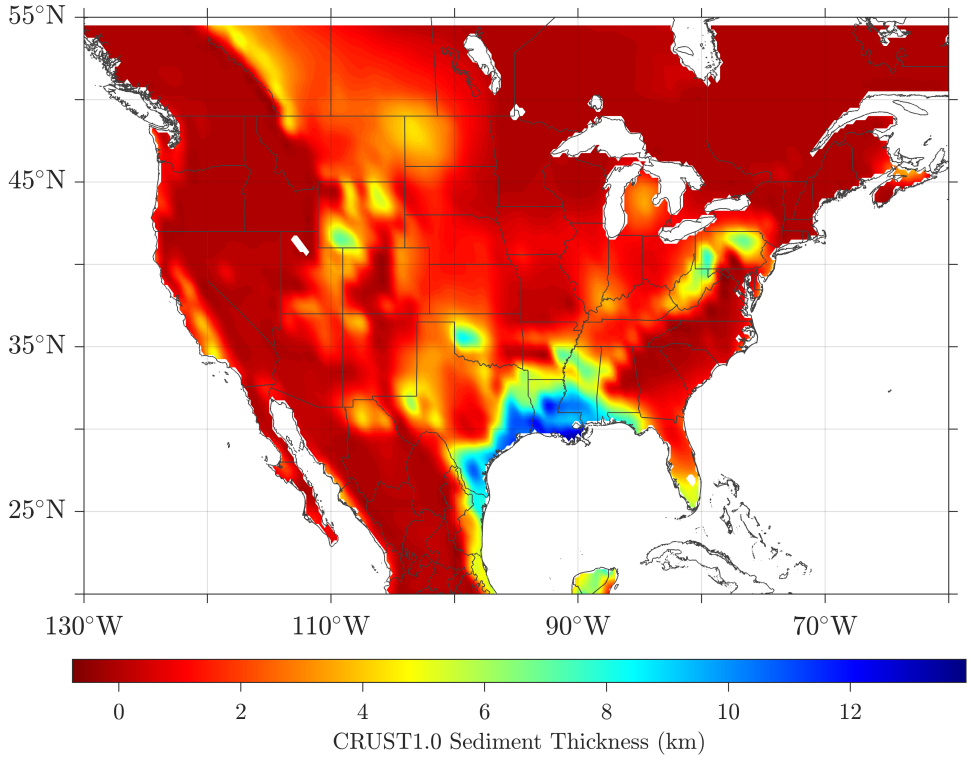


Figure A.6: Map of the sediment thickness across North America according to CRUST1.0 (Laske et al. 2013). Note the thick sediments near the Gulf of Mexico, coincident with the lowest values of $\bar{\nu}$ shown in Figure A.4.

Upon hovering over one of the triangles, the station code is displayed. When the user clicks on one of the stations, a plot showing the stacked receiver function with $\pm 2\sigma$ uncertainties indicated is shown (see Figures A.8, A.9, & A.10). In addition, scatter plots showing the magnitude-epicentral distance distribution, and the quality control parameter, ν, vs. quality of deconvolution fit for the data are shown. Finally, the total number of receiver functions, N, and the number of receiver functions used in the stack, N', are indicated at the top of the plot. Future work may see the extension of this tool to the entire US Array, and the inclusion of more data products for each individual station (such as additional choices of filtering parameters, gaussian width factors).

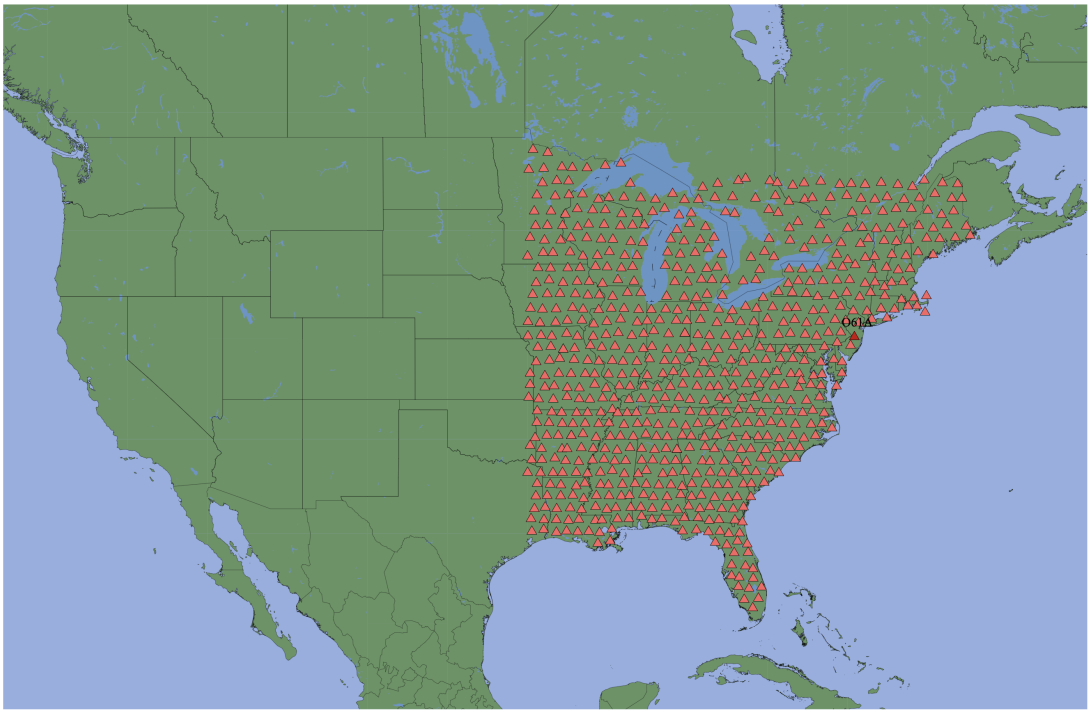


Figure A.7: Screenshot of the US Array receiver function explorer (`https://aburky.mycpanel.princeton.edu/usarray/us_array.php`).

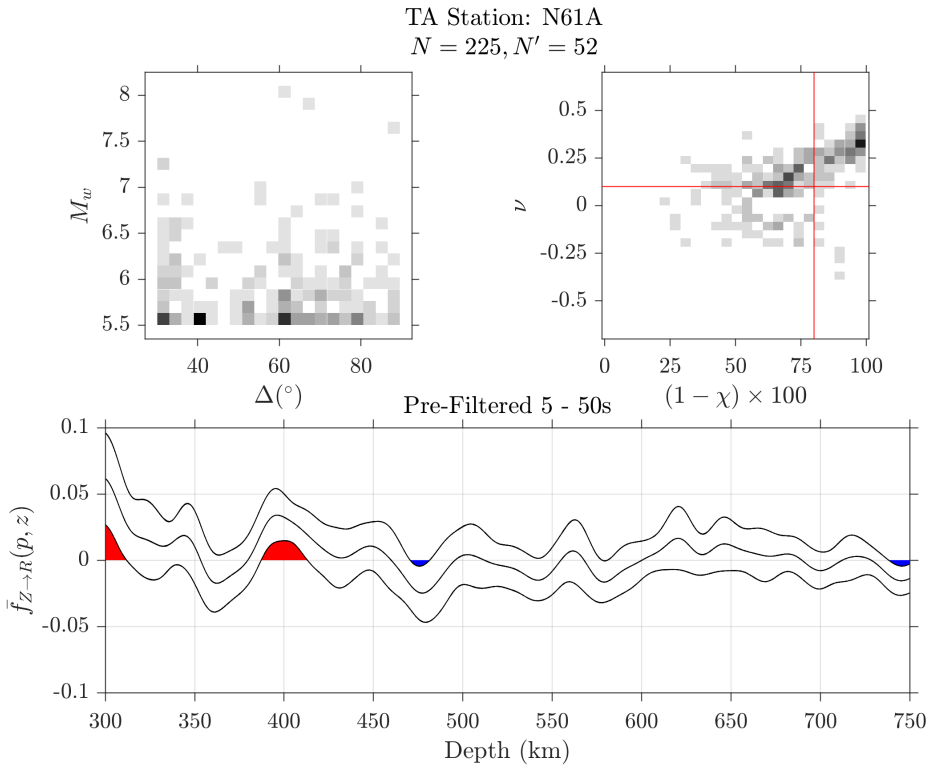


Figure A.8: Automated MTZ receiver function for station N61A.

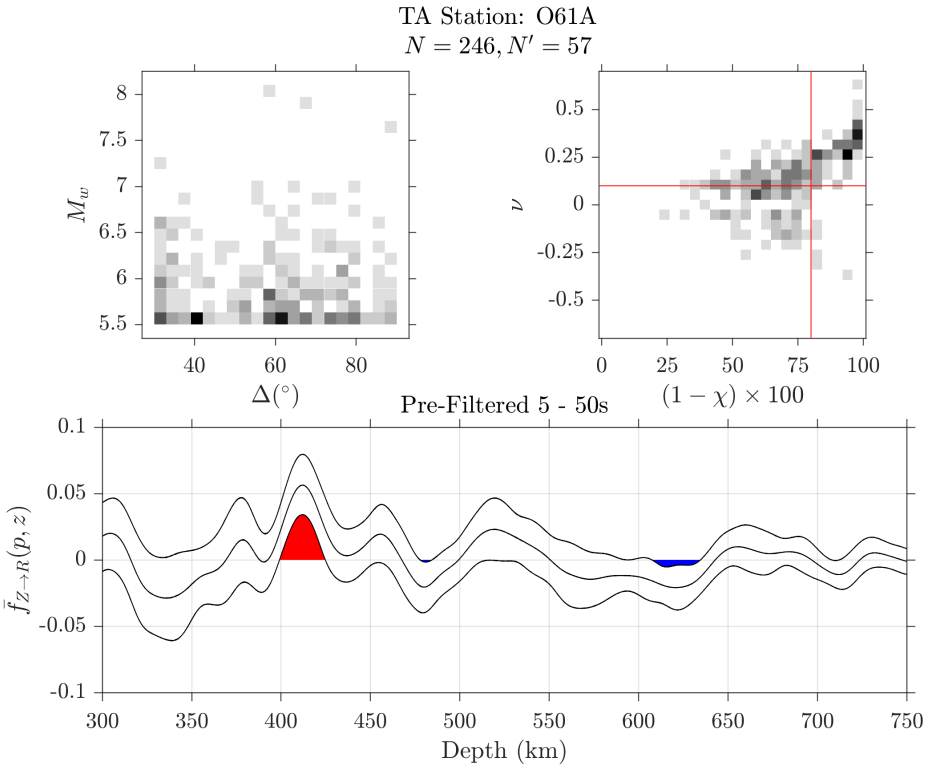


Figure A.9: Automated MTZ receiver function for station O61A.

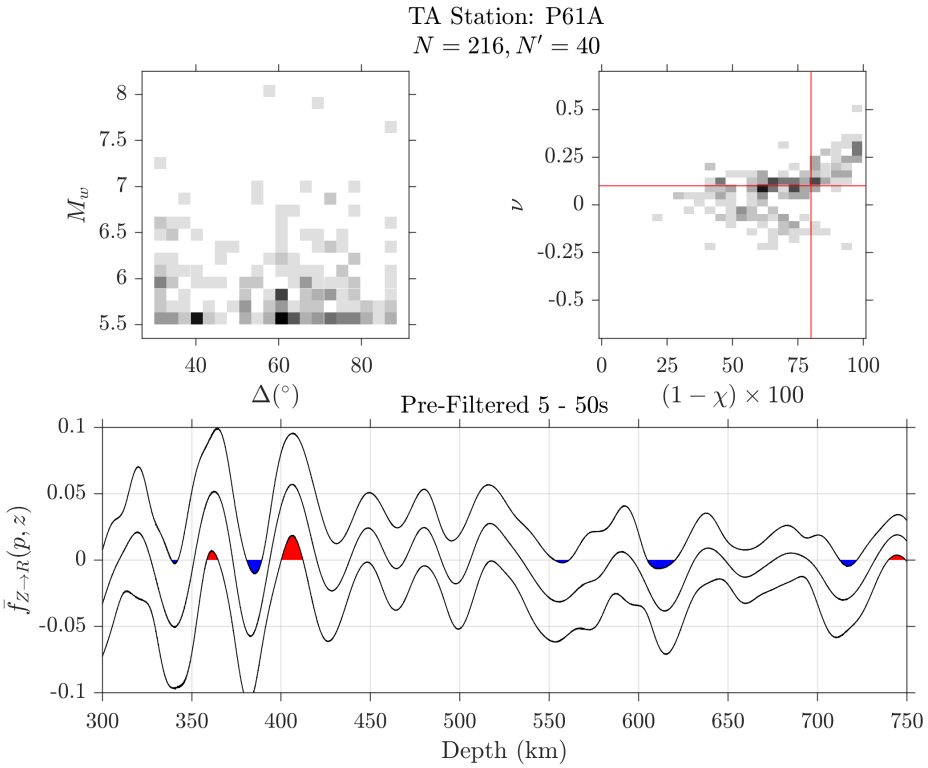


Figure A.10: Automated MTZ receiver function for station P61A.

Appendix B

Software Guide: `rflexa`

"`rflexa`, what does the mantle transition zone look like underneath network IU, station SACV?"

– Anonymous Graduate Student

Just as we use technological devices in our daily lives to play our favorite songs, or add items to our grocery list, `rflexa` came about from the desire to quickly and automatically construct MTZ receiver functions. As mentioned in earlier chapters of this thesis, all of the code is freely and publicly availabe in an open-source repository located at **github.com/alexburky/rflexa**. This section is meant to provide a summary of the useful functions present in the `rflexa` software package.

There are two main branches of `rflexa`: one written in Python, and the other written in MATLAB. Most of the functions were initially written in MATLAB, but halfway through development it was decided that Python was better suited to the open-access philosophy of this work. Because of this, nearly every function in `rflexa` has an implementation in both languages, but their usage varies due to the syntactical differences of each language. In this section, we give a high-level overview of the key functionality offered by `rflexa`. For a complete guide to getting started with the package, the reader is referred to the GitHub page.

B.1 fetchRF

```
% fetchRFQuakes.m
%
% This script fetches earthquake data for receiver function analysis,
% and additionally fetches poles and zeros data for the selected
% stations and channels. The earthquake data are saved as .SAC files,
% and their filenames are formatted so that they can be easily linked
% to their corresponding poles and zeros data.
%
%-------------------------------------------------------------------------
% Last updated 4/11/2021 by aburky@princeton.edu
%-------------------------------------------------------------------------

clear,clc

% Define the directory where you would like to save the data
sacDir = '/Users/YOURPATH/';

% Define the network/station that you would like to fetch data for
network = 'AF';
station = 'SVMA';
location = '*';
channel = 'BH*';

% Define desired earthquake parameters
minMag = 5.5;
maxMag = 9.0;
minRad = 30;
maxRad = 90;
```

As can be seen from the code excerpt above, the `fetchRF` function takes very few input arguments, but does a lot of work under the hood. First, the user needs to specify the seismic network code, station code, location code, and channel. Then, they specify the magnitude range of earthquake data they would like to download, and the distance range from the station to acceptable events. With these eight parameters, and the path to a folder to save the data, `fetchRF` queries the IRIS web server systematically to find all of the stations and events which satisfy these criteria. In a typical MTZ receiver function workflow, this code would be called first to save a database of seismograms on the user's computer, ready for subsequent receiver function calculations.

B.2 computeRFs

```
# ------------------------------------------------------------------
# computeRFs.py
#
# This function calculates receiver functions and saves them to a
# directory upon completion. The user can specify a choice of filter
# and Gaussian width factors for use in the data processing. The
# resulting SAC files are saved with additional metadata in the header:
#
# USER0: Vertical component SNR
# USER1: Radial component SNR
# USER2: RMS error calculated during iterative time domain deconvolution
# USER3: Quality metric, nu
#
# ------------------------------------------------------------------
# Last updated 11/12/2021 by aburky@princeton.edu
# ------------------------------------------------------------------


def computeRFs(network, location, data_directory, input_units,
    gaussian_width, high_cut, low_cut, station):
```

The `computeRF` function is intended to easily follow the `fetchRF` function. The user specifies the network, location, and station passed to `fetchRF`, as well as the path to the data that was saved by `fetchRF`, and the function then produces receiver functions. The additional parameters which must be specified are the desired physical units of the seismogram after instrument response removal (displacement, velocity, or acceleration, see Chapter 2), the gaussian width factor to be used in the deconvolution, and two optional parameters specifying the high and low frequency corners of a bandpass filter applied to the data before deconvolution. This function then calculates receiver functions using the `iterdecon` function, and saves them to a user-specified location.

B.3 iterdecon

The `iterdecon` function re-implements the Fortran code of Ligorría & Ammon (1999) to perform iterative time-domain deconvolution. The input parameters are the vertical and radial components of seismic data, and quantities specifying the resulting receiver function. This function is called by the `computeRFs` function during the bulk computation of receiver functions.

```
def iterdecon(num, den, dt, nt, tshift, f0, itmax, errtol):
    """
    Calculate a receiver function using the iterative time-domain
        deconvolution algorithm outlined by
    Ligorria & Ammon 1999.

    :param num: Numerator in deconvolution (radial component data for Z
        -> R receiver functions)
    :param den: Denominator in deconvolution (vertical component data
        for Z -> R receiver functions)
    :param dt: Sampling interval of data (seconds)
       :param nt: Length of input data vectors (samples)
    :param tshift: Desired time shift of resulting receiver function (
        seconds)
    :param f0: Gaussian width factor determining width of gaussian
        filter used in deconvolution
    :param itmax: Maximum allowed number of iterations before giving up
        and outputting receiver function
    :param errtol: Minimum change in error between iterations before
        giving up and outputting receiver function

    :return: RFI, RMS: An array containing the resulting receiver
        function (time-domain) and an array containing the RMS error
        from each iteration.
    """
```

B.4 transfer

```
def transfer(data, delta, freq_limits, units, file, file_type):
    """
    Remove the instrument response from a seismogram using a SAC Pole
        Zero (SAC_PZ) or RESP file.
    :param data: Vector containing seismic data
    :param delta: sample rate of the seismic data (s)
    :param freq_limits: Vector containing corner frequencies of cosine
        filter applied to seismic data
                        before deconvolution. This step is necessary to
                            stabilize the division.
    :param units: Desired output units. Currently supported values are '
        displacement', 'velocity', or
                    'acceleration'
    :param file: Full path to the response file
    :param file_type: File type containing the response information, one
         of 'sacpz' or 'resp'
    :return data: Vector containing the seismic data with the instrument
         response removed
    """
```

The `transfer` function has been extensively discussed in Chapter 2 of this thesis, and the reader is referred there for a thorough description of its usage and applications.

B.5 qcRF

```
function [rfQuality] = qcRF(rf,t)
% QCRF Calculate quality ratio for receiver function data.
%      For a complete description of the quality ratio
%      algorithm, see Burky et. al, 2020.
%
% >> [rfQuality] = QCRF(rf)
%
%---Input Variables-------------------------------------------
% rf          - Vector of receiver function data
% t           - Vector of corresponding time data (assumes RF
%               has been shifted to align the maximum at 10s)
%
%---Output Variables------------------------------------------
% rfQuality   - Scalar receiver function quality ratio
%
%-------------------------------------------------------------
% Last updated 1/5/2021 by aburky@princeton.edu
%-------------------------------------------------------------
```

The `qcRF` function implements the calculation of the quality control metric, ν, as described in Chapter 3 of this thesis. This metric is calculated during the call to `computeRFs` and is saved with the resulting receiver function so the user can utilize it for subsequent analysis.

B.6 rfDepcon

```
function [rf_d] = rfDepcon(rf, dt, rayParam, dz, model, normalize)
% RFDEPCON Depth convert receiver functions using a one-dimensional
%          earth model.
%
% >> [rf_d] = RFDEPCON(rf, dt, rayParameter, dz, model)
%
%---Input Variables-------------------------------------------------
% rf        - Receiver function data
% dt        - Sample rate of data (s)
% rayParam  - P-wave ray parameter (s/km)
% dz        - Depth sampling rate (km)
% model     - Earth model (accepted values: 'iasp91', 'prem')
% normalize - Normalize the receiver function amplitude ('true','false')
%
%---Output Variables------------------------------------------------
% rf_d      - Depth converted receiver function
%
%-------------------------------------------------------------------
% Last updated 5/27/2021 by aburky@princeton.edu
%-------------------------------------------------------------------
```

The `rfDepcon` function converts receiver functions from the time domain to the depth domain, via a velocity model. The excerpt shown is for the case of a one-dimensional velocity model, but there is a variant of the function `rfDepcon3D` which can be used to depth convert with a three-dimensional velocity model. This function was used extensively in the work of Chapters 2 and 3, and is critical in producing receiver functions which can be interpreted.

B.7 Utility Functions

The functions described above are the most critical pieces of software required to generate MTZ receiver functions, but they are only a small part of the software contained in `rflexa`. For the sake of brevity, the additional functions of `rflexa` will only be listed below, without a full description. The interested reader is invited to visit the GitHub page for complete documentation of any of these functions:

- `bodePlot` - visualize instrument response functions
- `ccpStack` - produce a CCP stack from a collection of receiver functions
- `parsePZ` - parse a SAC_PZ file for relevant information
- `parseRESP` - parse a RESP file for relevant information
- `rfCrossSection` - produce a cross section plot from receiver functions
- `savePZ` - save a SAC_PZ file during data download
- `saveRF` - save a receiver function as a SAC file
- `saveSAC` - save data as a SAC file
- `seisrt` - rotate a seismogram to the RTZ system
- `stackRFs` - stack a collection of receiver functions

References

Agee, J. J., Garrison, J. R. & Taylor, L. A. (1982), 'Petrogenesis of oxide minerals in kimberlite, Elliott County, Kentucky', *American Mineralogist* **67**(1-2), 28–42.

Akaogi, M., Takayama, H., Kojitani, H., Kawaji, H. & Atake, T. (2007), 'Low-temperature heat capacities, entropies and enthalpies of Mg_2SiO_4 polymorphs, and α-β-γ and post-spinel phase relations at high pressure', *Phys. Chem. Miner.* **34**(3), 169–183, doi: 10.1007/s00269–006–0137–3.

Akimoto, S. I. & Fujisawa, H. (1968), 'Olivine-spinel solid solution equilibria in the system mg_2sio_4-fe_2sio_4', *J. Geophys. Res.* **73**(4), 1467–1479, doi: 10.1029/JB073i004p01467.

Ammon, C. J. (1991), 'The isolation of receiver effects from teleseismic P waveforms', *B. Seismol. Soc. Am.* **81**, 2504–2510.

Andrews, J. & Deuss, A. (2008), 'Detailed nature of the 660 km region of the mantle from global receiver function data', *J. Geophys. Res.* **113**, B06304, doi: 10.1029/2007JB005111.

Anthony, R. E., Ringler, A. T., Wilson, D. C. & Wolin, E. (2019), 'Do low-cost seismographs perform well enough for your network? an overview of laboratory tests and field observations of the OSOP Raspberry Shake 4D', *Seismol. Res. Lett.* **90**(1), 219–228, doi: 10.1785/0220180251.

Asch, G. (2009), Seismic systems, *in* P. Bormann, ed., 'New Manual of Seismological Observatory Practice 2 (NMSOP-2)', Deutsches GeoForschungsZentrum, IASPEI, Potsdam, Germany, chapter 6, pp. 1–20, doi: 10.2312/GFZ.NMSOP_r1_ch6.

Becker, J. J., Sandwell, D. T., Smith, W. H. F., Braud, J., Binder, B., Depner, J., Fabre, D., Factor, J., Ingalls, S., Kim, S.-H., Ladner, R., Marks, K., Nelson, S., Pharaoh, A., Trimmer, R., Rosenberg, J. V., Wallace, G. & Weatherall, P. (2009), 'Global bathymetry and elevation data at 30 arc seconds resolution: SRTM30_PLUS', *Mar. Geod.* **32**(4), 355–371, doi: 10.1080/01490410903297766.

Bendat, J. S. & Piersol, A. G. (2000), *Random Data: Analysis and Measurement Procedures*, 3 edn, Wiley, New York.

Benoit, M. H., Long, M. D. & King, S. D. (2013), 'Anomalously thin transition zone and apparently isotropic upper mantle beneath Bermuda: Evidence for upwelling', *Geochem. Geophys. Geosys.* **14**(10), 4282–4291, doi: 10.1002/ggge.20277.

Bina, C. R. & Helffrich, G. R. (1994), 'Phase transition Clapeyron slopes and transition zone seismic discontinuity topography', *J. Geophys. Res.* **99**(B8), 15853–15860, doi: 10.1029/94JB00462.

Birch, F. (1952), 'Elasticity and constitution of the Earth's interior', *J. Geophys. Res.* **57**(2), 227–286, doi: 10.1029/JZ057i002p00227.

Bormann, P., ed. (2012), *New Manual of Seismological Observatory Practice 2 (NMSOP-2)*, Deutsches GeoForschungsZentrum, IASPEI, Potsdam, Germany.

Brunsvik, B. R., Eilon, Z. C. & Lynner, C. (2021), 'Mantle structure and flow across the continent-ocean transition of the eastern North American margin: Anisotropic S-wave tomography', *Geochem. Geophys. Geosys.* **22**(12), e2021GC010084, doi: 10.1029/2021GC010084.

Bullen, K. E. (1956), 'Seismology and the broad structure of the Earth's interior', *Phys. Chem. Earth* **1**, 68–93, doi: 10.1016/0079–1946(56)90006–4.

Burky, A. L., Irving, J. C. E. & Simons, F. J. (2021*a*), 'Instrument response removal and the 2020 M_{Lg} 3.1 Marlboro, New Jersey, earthquake', *Seismol. Res. Lett.* **92**(6), 3865–3872, doi: 10.1785/0220210118.

Burky, A. L., Irving, J. C. E. & Simons, F. J. (2021*b*), 'Mantle transition zone receiver functions for Bermuda: Automation, quality control, and interpretation', *J. Geophys. Res. Solid Earth* pp. e2020JB020177, doi: 10.1029/2020JB020177.

Byerly, P. (1926), 'The Montana earthquake of June 28, 1925, GMCT', *B. Seismol. Soc. Am.* **16**(4), 209–265, doi: 10.1785/BSSA0160040209.

Byrnes, J. S., Bezada, M., Long, M. D. & Benoit, M. H. (2019), 'Thin lithosphere beneath the central Appalachian Mountains: Constraints from seismic attenuation beneath the MAGIC array', *Earth Planet. Sci. Lett.* **519**, 297–307, doi: 10.1016/j.epsl.2019.04.045.

Cammarano, F., Goes, S., Vacher, P. & Giardini, D. (2003), 'Inferring upper-mantle temperatures from seismic velocities', *Phys. Earth Planet. Inter.* **138**(3-4), 197–222, doi: 10.1016/S0031–9201(03)00156–0.

Chevrot, S., Vinnik, L. & Montagner, J.-P. (1999), 'Global scale analysis of mantle *Pds* phases', *J. Geophys. Res.* **104**(B9), 20203–20219, doi: 10.1029/1999JB900087.

Chu, R., Leng, W., Helmberger, D. V. & Gurnis, M. (2013), 'Hidden hotspot track beneath the eastern United States', *Nature Geosci.* **6**(11), 963–966.

Cottaar, S. & Deuss, A. (2016), 'Large-scale mantle discontinuity topography beneath Europe: Signature of akimotoite in subducting slabs', *J. Geophys. Res. Solid Earth* **121**(1), 279–292, doi: 10.1002/2015JB012452.

Courtillot, V., Davaille, A., Besse, J. & Stock, J. (2003), 'Three distinct types of hotspots in the Earth's mantle', *Earth Planet. Sci. Lett.* **205**(3–4), 295–308, doi: 10.1016/S0012–821X(02)01048–8.

Cox, R. T. & Van Arsdale, R. B. (2002), 'The Mississippi Embayment, North America: a first order continental structure generated by the Cretaceous superplume mantle event', *J. Geod.* **34**(2), 163–176.

Crotwell, H. P. & Owens, T. J. (2005), 'Automated receiver function processing', *Seismol. Res. Lett.* **76**(6), 702–709, doi: 10.1785/gssrl.76.6.702.

Crotwell, H. P., Owens, T. J. & Ritsema, J. (1999), 'The TauP Toolkit: Flexible seismic travel-time and ray-path utilities', *Geophys. Res. Lett.* **70**(2), 154–160, doi: 10.1785/gssrl.70.2.154.

Davies, D., Kelly, E. J. & Filson, J. R. (1971), 'Vespa process for analysis of seismic signals', *Nature Physical Science* **232**(27), 8–13, doi: 10.1038/physci232008a0.

Day, E. A. & Deuss, A. (2013), 'Reconciling *PP* and *P'P'* precursor observations of a complex 660 km seismic discontinuity', *Geophys. J. Int.* **194**(2), 834–838, doi: 10.1093/gji/ggt122.

Deuss, A., Andrews, J. & Day, E. (2013), *Seismic Observations of Mantle Discontinuities and Their Mineralogical and Dynamical Interpretation*, John Wiley & Sons, Ltd., chapter 10, pp. 295–323, doi: 10.1002/9781118529492.ch10.

Deuss, A., Redfern, S. A. T., Chambers, K. & Woodhouse, J. H. (2006), 'The nature of the 660-kilometer discontinuity in Earth's mantle from global seismic observations of *PP* precursors', *Science* **311**(5758), 198–201, doi: 10.1126/science.1120020.

Dueker, K. G. & Sheehan, A. F. (1997), 'Mantle discontinuity structure from midpoint stacks of converted *P* to *S* waves across the Yellowstone hotspot track', *J. Geophys. Res. Solid Earth* **102**(B4), 8313–8327, doi: 10.1029/96JB03857.

Dziewoński, A. M. & Anderson, D. L. (1981), 'Preliminary Reference Earth Model', *Phys. Earth Planet. Inter.* **25**(4), 297–356, doi: 10.1016/0031–9201(81)90046–7.

Eaton, D. W. & Frederiksen, A. (2007), 'Seismic evidence for convection-driven motion of the North American plate', *Nature* **446**(7134), 428–431, doi: 10.1038/nature05675.

Ebel, J. E. & Kafka, A. L. (2002), 'A non-Poissonian element in the seismicity of the northeastern United States', *B. Seismol. Soc. Am.* **92**(5), 2040–2046, doi: 10.1785/0120010211.

Efron, B. & Tibshirani, R. (1986), 'Bootstrap methods for standard errors, confidence intervals, and other measures of statistical accuracy', *Stat. Sci.* **1**(1), 54–75.

Ekström, G., Nettles, M. & Dziewonski, A. M. (2012), 'The global CMT project 2004-2010: Centroid-moment tensors for 13,017 earthquakes', *Phys. Earth Planet. Inter.* **200–201**, 1–9, doi: 10.1016/j.pepi.2012.04.002.

Forte, A. M., Mitrovica, J. X., Moucha, R., Simmons, N. A. & Grand, S. P. (2007), 'Descent of the ancient Farallon slab drives localized mantle flow below the New Madrid seismic zone', *Geophys. Res. Lett.* **34**(4), doi: 10.1029/2006GL027895.

French, S. W. & Romanowicz, B. (2014), 'Whole-mantle radially anisotropic shear velocity structure from spectral-element waveform tomography', *Geophys. J. Int.* **199**(3), 1303–1327, doi: 10.1093/gji/ggu334.

French, S. W. & Romanowicz, B. (2015), 'Broad plumes rooted at the base of the Earth's mantle beneath major hotspots', *Nature* **525**(7567), 95–99, doi: 10.1038/nature14876.

Frost, D. J. (2008), 'The upper mantle and transition zone', *Elements* **4**(3), 171–176, doi: 10.2113/GSELEMENTS.4.3.171.

Gao, S. S. & Liu, K. H. (2014), 'Mantle transition zone discontinuities beneath the contiguous United States', *J. Geophys. Res.* **119**(8), 6452–6468, doi: 10.1002/2014JB011253.

Geoffroy, L. (2005), 'Volcanic passive margins', *C. R. Geosci.* **337**(16), 1395–1408, doi: 10.1016/j.crte.2005.10.006.

Goldstein, P. & Snoke, A. (2005), 'SAC availability for the IRIS community', *Incorporated Research Institutions for Seismology Newsletter* **7**(UCRL-JRNL-211140).

Gurrola, H., Minster, J. B. & Owens, T. (1994), 'The use of velocity spectrum for stacking receiver functions and imaging upper mantle discontinuities', *Geophys. J. Int.* **117**(2), 427–440, doi: 10.1111/j.1365–246X.1994.tb03942.x.

Hatcher, R. D., Tollo, R. P., Bartholomew, M. J., Hibbard, J. P. & Karabinos, P. M. (2010), 'The Appalachian orogen: A brief summary', *From Rodinia to Pangea: The Lithotectonic Record of the Appalachian Region: Geological Society of America Memoir* **206**, 1–19, doi: 10.1130/2010.1206(01).

Havskov, J. & Alguacil, G. (2016), *Instrumentation in Earthquake Seismology*, 2 edn, Springer, Heidelberg, Germany.

Helffrich, G. R. (2000), 'Topography of the transition zone seismic discontinuities', *Rev. Geophys.* **38**(1), 141–158, doi: 10.1029/1999RG000060.

Helffrich, G. R., Asencio, E., Knapp, J. & Owens, T. (2003), 'Transition zone structure in a tectonically inactive area: 410 and 660 km discontinuity properties under the northern North Sea', *Geophys. J. Int.* **155**(1), 193–199, doi: 10.1046/j.1365–246X.2003.02036.x.

Helffrich, G. R. & Wood, B. J. (2001), 'The Earth's mantle', *Nature* **412**(6846), 501–507, doi: 10.1038/35087500.

Hirose, K. (2002), 'Phase transitions in pyrolitic mantle around 670-km depth: Implications for upwelling of plumes from the lower mantle', *J. Geophys. Res.* **107**(B4), 2078, doi: 10.1029/2001JB000597.

Houser, C. (2016), 'Global seismic data reveal little water in the mantle transition zone', *Earth Planet. Sci. Lett.* **448**, 94–101, doi: 10.1016/j.epsl.2016.04.018.

Houser, C. & Williams, Q. (2010), 'Reconciling Pacific 410 and 660 km discontinuity topography, transition zone shear velocity patterns, and mantle phase transitions', *Earth Planet. Sci. Lett.* **296**(3–4), 255–266, doi: 10.1016/j.epsl.2010.05.006.

Huang, Q., Schmerr, N., Waszek, L. & Beghein, C. (2019), 'Constraints on seismic anisotropy in the mantle transition zone from long-period *SS* precursors', *J. Geophys. Res. Solid Earth* **124**(7), 6779–6800, doi: 10.1029/2019JB017307.

Humphreys, E. D., Schmandt, B., Bezada, M. J. & Perry-Houts, J. (2015), 'Recent craton growth by slab stacking beneath Wyoming', *Earth Planet. Sci. Lett.* **429**, 170–180, doi: 10.1016/j.epsl.2015.07.066.

Ito, E., Akaogi, M., Topor, L. & Navrotsky, A. (1990), 'Negative pressure-temperator slopes for reactions forming $MgSiO_3$ perovskite from calorimetry', *Science* **249**(4974), 1275–1278, doi: 10.1126/science.249.4974.1275.

Jackson, M. G., Konter, J. G. & Becker, T. W. (2017), 'Primordial helium entrained by the hottest mantle plumes', *Nature* **542**(7641), 340–343, doi: 10.1038/nature21023.

Jenkins, J., Cottaar, S., White, R. S. & Deuss, A. (2016), 'Depressed mantle discontinuities beneath Iceland: Evidence of a garnet controlled 660 km discontinuity?', *Earth Planet. Sci. Lett.* **433**, 159–168, doi: 10.1016/j.epsl.2015.10.053.

Kafka, A. L., Schlesinger-Miller, E. A. & Barstow, N. L. (1985), 'Earthquake activity in the greater New York City area: magnitudes, seismicity, and geologic structures', *B. Seismol. Soc. Am.* **75**(5), 1285–1300, doi: 10.1785/BSSA0750051285.

Kafka, A. L., Winslow, M. A. & Barstow, N. L. (1989), Earthquake activity in the greater new york city area: A fault finder's guide, *in* 'Field Trip Guidebook, 61st Annual Meeting, New York State Geological Association', pp. 177–205.

Keifer, I. & Dueker, K. (2019), 'Testing the hypothesis that temperature modulates 410 and 660 discontinuity topography beneath the eastern United States', *Earth Planet. Sci. Lett.* **524**, 115723, doi: 10.1016/j.epsl.2019.115723.

Kennett, B. L. N. & Engdahl, E. R. (1991), 'Traveltimes for global earthquake location and phase identification', *Geophys. J. Int.* **105**(2), 429–465, doi: 10.1111/j.1365–246X.1991.tb06724.x.

Kind, R. & Vinnik, L. P. (1988), 'The upper-mantle discontinuities underneath the GRF array from P-to-S converted phases', *J. Geophys.* **62**(1), 138–147.

King, S. D. & Adam, C. (2014), 'Hotspot swells revisited', *Phys. Earth Planet. Inter.* **235**, 66–83, doi: 10.1016/j.pepi.2014.07.006.

King, S. D. & Anderson, D. L. (1998), 'Edge-driven convection', *Earth Planet. Sci. Lett.* **160**(3–4), 289–296, doi: 10.1016/S0012–821X(98)00089–2.

Kinney, S. T., MacLennan, S. A., Keller, C. B., Schoene, B., Setera, J. B., VanTongeren, J. A. & Olsen, P. E. (2021), 'Zircon U-Pb geochronology constrains continental expression of Great Meteor Hotspot magmatism', *Geophys. Res. Lett.* pp. e2020GL091390, doi: 10.1029/2020GL091390.

Langston, C. A. (1979), 'Structure under Mount Rainier, Washington, inferred from teleseismic body waves', *J. Geophys. Res.* **84**(B9), 4749–4762.

Laske, G., Masters, G., Ma, Z. & Pasyanos, M. (2013), Update on CRUST1.0 A 1-degree global model of Earths crust, *in* 'Geophys. Res. Abstracts', Vol. 15, pp. EGU2013–2658.

Lawrence, J. F. & Shearer, P. M. (2006), 'A global study of transition zone thickness using receiver functions', *J. Geophys. Res.* **111**(B06307), doi: 10.1029/2005JB003973.

Leahy, G. M. (2009), 'Local variability in the 410-km mantle discontinuity under a hotspot', *Earth Planet. Sci. Lett.* **288**(1–2), 158–163, doi: 10.1016/j.epsl.2009.09.018.

Lehmann, I. (1970), 'The 400-km discontinuity', *Geophys. J. Int.* **21**(3), 359–372, doi: 10.1111/j.1365–246X.1970.tb01797.x.

Lei, W., Ruan, Y., Bozdağ, E., Peter, D., Lefebvre, M., Komatitsch, D., Tromp, J., Hill, J., Podhorszki, N. & Pugmire, D. (2020), 'Global adjoint tomography–model GLAD-M25', *Geophys. J. Int.* **223**(1), 1–21, doi: 10.1093/gji/ggaa253.

Lekić, V., Cottaar, S., Dziewoński, A. & Romanowicz, B. (2012), 'Cluster analysis of global lower mantle tomography: A new class of structure and implications for chemical heterogeneity', *Earth Planet. Sci. Lett.* **357**, 68–77, doi: 10.1016/j.epsl.2012.09.014.

Levin, V., Long, M. D., Skryzalin, P., Li, Y. & López, I. (2018), 'Seismic evidence for a recently formed mantle upwelling beneath New England', *Geology* **46**(1), 87–90, doi: 10.1130/G39641.1.

Levin, V., Menke, W. & Park, J. (2000), 'No regional anisotropic domains in the northeastern US Appalachians', *J. Geophys. Res. Solid Earth* **105**(B8), 19029–19042, doi: 10.1029/2000JB900123.

Li, A., Fischer, K. M., Wysession, M. E. & Clarke, T. J. (1998), 'Mantle discontinuities and temperature under the North American continental keel', *Nature* **395**(6698), 160–163, doi: 10.1038/25972.

Li, Y., Levin, V., Elkington, S. & Hlavaty, J. (2019), 'Localized anisotropic domains beneath eastern North America', *Geochem. Geophys. Geosys.* **20**(11), 5499–5521, doi: 10.1029/2019GC008518.

Ligorría, J. P. & Ammon, C. J. (1999), 'Iterative deconvolution and receiver-function estimation', *B. Seismol. Soc. Am.* **89**(5), 1395–1400.

Liu, K. H. & Gao, S. S. (2006), 'Mantle transition zone discontinuities beneath the Baikal rift and adjacent areas', *J. Geophys. Res.* **111**(B11301), doi: 10.1029/2005JB004099.

Liu, L., Gao, S. S., Liu, K. H. & Mickus, K. (2017), 'Receiver function and gravity constraints on crustal structure and vertical movements of the Upper Mississippi embayment and Ozark uplift', *J. Geophys. Res.* **122**(6), 4572–4583.

Lognonné, P., Banerdt, W. B., Pike, W. T., Giardini, D., Christensen, U., Garcia, R., Kawamura, T., Kedar, S., Knapmeyer-Endrun, B., Margerin, L. et al. (2020), 'Constraints on the shallow elastic and anelastic structure of Mars from InSight seismic data', *Nature Geosci.* **13**(3), 213–220, doi: 10.1038/s41561–020–0536–y.

Long, M. D., Benoit, M. H., Chapman, M. C. & King, S. D. (2010), 'Upper mantle anisotropy and transition zone thickness beneath southeastern North America and implications for mantle dynamics', *Geochem. Geophys. Geosys.* **11**(10), doi: 10.1029/2010GC003247.

Long, M. D., Jackson, K. G. & McNamara, J. F. (2016), '*SKS* splitting beneath Transportable Array stations in eastern North America and the signature of past lithospheric deformation', *Geochem. Geophys. Geosys.* **17**(1), 2–15, doi: 10.1002/2015GC006088.

Long, M. D., Levander, A. & Shearer, P. M. (2014), 'An introduction to the special issue of Earth and Planetary Science Letters on USArray science', *Earth Planet. Sci. Lett.* **402**, 1–5, doi: 10.1016/j.epsl.2014.06.016.

Maguire, R., Ritsema, J. & Goes, S. (2018), 'Evidence of subduction-related thermal and compositional heterogeneity below the United States from transition zone receiver functions', *Geophys. Res. Lett.* **45**(17), 8913–8922, doi: 10.1029/2018GL078378.

Mazza, S. E., Gazel, E., Bizimis, M., Moucha, R., Béguelin, P., Johnson, E. A., McAleer, R. J. & Sobolev, A. V. (2019), 'Sampling the volatile-rich transition zone beneath Bermuda', *Nature* **569**(7756), 398–403.

Mazza, S. E., Gazel, E., Johnson, E. A., Kunk, M. J., McAleer, R., Spotila, J. A., Bizimis, M. & Coleman, D. S. (2014), 'Volcanoes of the passive margin: The youngest magmatic event in eastern North America', *Geology* **42**(6), 483–486.

Menke, W., Skryzalin, P., Levin, V., Harper, T., Darbyshire, F. & Dong, T. (2016), 'The northern Appalachian anomaly: A modern asthenospheric upwelling', *Geophys. Res. Lett.* **43**(19), 10–173, doi: 10.1002/2016GL070918.

Mohorovičić, A. (1992), 'Earthquake of 8 October, 1909', *Geofiz.* **9**(1), 3–55.

Morgan, W. J. (1971), 'Convection plumes in the lower mantle', *Nature* **230**(5288), 42–43, doi: 10.1038/230042a0.

Nelson, K. D. (1992), 'Are crustal thickness variations in old mountain belts like the Appalachians a consequence of lithospheric delamination?', *Geology* **20**(6), 498–502, doi: 10.1130/0091–7613(1992)020<0498:ACTVIO>2.3.CO;2.

Nishimura, E., Kishimoto, Y. & Kamitsuki, A. (1958), 'On the Nature of the 20°-Discontinuity in the Earth's Mantle', *Tellus* **10**(1), 137–144, doi: 10.3402/tellusa.v10i1.9211.

Nissen-Meyer, T., van Driel, M., Stähler, S. C., Hosseini, K., Hempel, S., Auer, L., Colombi, A. & Fournier, A. (2014), 'AxiSEM: broadband 3-D seismic wavefields in axisymmetric media', *Solid Earth* **5**, 425–445, doi: 10.5194/se–5–425–2014.

Owens, J. P., Sugarman, P. J., Sohl, N. F., Parker, R., Houghton, H. H., Volkert, R. V., Drake, A. A. & Orndorff, R. C. (1995), Geologic map of New Jersey: Central Sheet, scale 1:100,000, Open-file report 95-253, U. S. Dept. Interior, Geological Survey.

Page, M. T. & Hough, S. E. (2014), 'The New Madrid Seismic Zone: Not Dead Yet', *Science* **343**(6172), 762–764, doi: 10.1126/science.1248215.

Page, R. A., Molnar, P. H. & Oliver, J. (1968), 'Seismicity in the vicinity of the Ramapo fault, New Jersey-New York', *B. Seismol. Soc. Am.* **58**(2), 681–687, doi: 10.1785/BSSA0580020681.

Phinney, R. A. (1964), 'Structure of the Earth's crust from spectral behavior of long-period body waves', *J. Geophys. Res.* **69**(14), 2997–3017, doi: 10.1029/JZ069i014p02997.

Piermarini, G. J. (2001), 'High pressure X-ray crystallography with the diamond cell at NIST/NBS', *J. Res. Natl. Inst. Stand. Technol.* **106**(6), 889, doi: 10.6028/jres.106.045.

Ringler, A. T. & Bastien, P. (2020), 'A brief introduction to seismic instrumentation: where does my data come from?', *Seismol. Res. Lett.* **91**(2A), 1074–1083, doi: 10.1785/0220190214.

Ringwood, A. E. (1991), 'Phase transformations and their bearing on the constitution and dynamics of the mantle', *Geochim. Cosmochim. Acta* **55**(8), 2083–2110, doi: 10.1016/0016–7037(91)90090–R.

Savage, B. (2021), 'Body wave speed structure of eastern North America', *Geochem. Geophys. Geosys.* **22**(1), e2020GC009002, doi:10.1029/2020GC009002.

Schaeffer, A. J. & Lebedev, S. (2014), 'Imaging the North American continent using waveform inversion of global and USArray data', *Earth Planet. Sci. Lett.* **402**, 26–41, doi: 10.1016/j.epsl.2014.05.014.

Scherbaum, F. (2001), *Of Poles and Zeros: Fundamentals of Digital Seismology*, 2 edn, Kluwer, Norwell, Mass.

Schmandt, B. & Lin, F.-C. (2014), 'P and S wave tomography of the mantle beneath the United States', *Geophys. Res. Lett.* **41**(18), 6342–6349, doi: 10.1002/2014GL061231.

Shearer, P. M. (1990), 'Seismic imaging of upper-mantle structure with new evidence for a 520-km discontinuity', *Nature* **334**(6262), 121–126, doi: 10.1038/344121a0.

Shearer, P. M. & Buehler, J. (2019), 'Imaging upper-mantle structure under USArray using long-period reflection seismology', *J. Geophys. Res. Solid Earth* **124**(9), 9638–9652, doi: 10.1029/2019JB017326.

Shearer, P. M. & Masters, T. G. (1992), 'Global mapping of topography on the 660-km discontinuity', *Nature* **355**(6363), 791–796, doi: 10.1038/355791a0.

Sigloch, K. (2011), 'Mantle provinces under North America from multi-frequency P wave tomography', *Geochem. Geophys. Geosys.* **12**(2), doi: 10.1029/2010GC003421.

Sigloch, K., McQuarrie, N. & Nolet, G. (2008), 'Two-stage subduction history under North America inferred from multiple-frequency tomography', *Nature Geosci.* **1**(7), 458–462, doi: 10.1038/ngeo231.

Simmons, N. A., Forte, A. M., Boschi, L. & Grand, S. P. (2010), 'GyPSuM: A joint tomographic model of mantle density and seismic wave speeds', *J. Geophys. Res.* **115**, B12310, doi: 10.1029/2010JB007631.

Simmons, N. A. & Gurrola, H. (2000), 'Multiple seismic discontinuities near the base of the transition zone in the Earth's mantle', *Nature* **405**(6786), 559–562, doi: 10.1038/35014589.

Simmons, N. A., Myers, S. C., Johannesson, G. & Matzel, E. (2012), 'LLNL-G3Dv3: Global P wave tomography model for improved regional and teleseismic travel time prediction', *J. Geophys. Res.* **117**, B10302, doi: 10.1029/2012JB009525.

Simmons, N. A., Myers, S. C., Johannesson, G., Matzel, E. & Grand, S. P. (2015), 'Evidence for long-lived subduction of an ancient tectonic plate beneath the southern Indian Ocean', *Geophys. Res. Lett.* **42**(21), 9270–9278, doi: 10.1002/2015GL066237.

Simon, J. D., Simons, F. J. & Irving, J. C. E. (2021), 'A MERMAID miscellany: Seismoacoustic signals beyond the P wave', *Seismol. Res. Lett.* pp. 1–11, doi: 10.1785/022021005.

Sleep, N. H. (1990), 'Hotspots and mantle plumes: Some phenomenology', *J. Geophys. Res.* **95**(B5), 6715–6736, doi: 10.1029/JB095iB05p06715.

Steinberger, B., Sutherland, R. & O'Connell, R. J. (2004), 'Prediction of Emperor-Hawaii seamount locations from a revised model of global plate motion and mantle flow', *Nature* **430**, 167–173, doi: 10.1038/nature02660.

Tauzin, B., Debayle, E. & Wittlinger, G. (2008), 'The mantle transition zone as seen by global Pds phases: No clear evidence for a thin transition zone beneath hotspots', *J. Geophys. Res. Solid Earth* **113**(B08309), doi: 10.1029/2007JB005364.

Torgersen, T., Drenkard, S., Stute, M., Schlosser, P. & Shapiro, A. (1995), 'Mantle helium in ground waters of eastern North America: Time and space constraints on sources', *Geology* **23**(8), 675–678, doi: 10.1130/0091–7613(1995)023<0675:MHIGWO>2.3.CO;2.

Tsujino, N., Yoshino, T., Yamazaki, D., Sakurai, M., Sun, W., Xu, F., Tange, Y. & Higo, Y. (2019), 'Phase transition of wadsleyite-ringwoodite in the Mg_2SiO_4-Fe_2SiO_4 system', *Am. Mineral.* **104**, 588–594.

Vacher, P., Mocquet, A. & Sotin, C. (1998), 'Computation of seismic profiles from mineral physics: the importance of the non-olivine components for explaining the 660 km depth discontinuity', *Phys. Earth Planet. Inter.* **106**(3), 275–298, doi: 10.1016/S0031–9201(98)00076–4.

van der Lee, S., Regenauer-Lieb, K. & Yuen, D. A. (2008), 'The role of water in connecting past and future episodes of subduction', *Earth Planet. Sci. Lett.* **273**(1-2), 15–27, doi: 10.1016/j.epsl.2008.04.041.

van der Meijde, M., Marone, F., Giardini, D. & van der Lee, S. (2003), 'Seismic evidence for water deep in Earth's upper mantle', *Science* **300**(5625), 1556–1558, doi: 10.1126/science.1083636.

van Driel, M., Krischer, L., Stähler, S., Hosseini, K. & Nissen-Meyer, T. (2015), 'Instaseis: Instant gloabl seismograms based on a broadband waveform database', *Solid Earth* **6**(2), 701–717, doi: 10.5194/se–6–701–2015.

van Stiphout, A. M., Cottaar, S. & Deuss, A. (2019), 'Receiver function mapping of mantle transition zone discontinuities beneath Alaska using scaled 3-D velocity corrections', *Geophys. J. Int.* **219**(2), 1432–1446, doi: 10.1093/gji/ggz360.

Vinnik, L. (1977), 'Detection of waves converted from P to SV in the mantle', *Phys. Earth Planet. Inter.* **15**(1), 39–45.

Vogt, P. & Jung, W.-Y. (2007), 'Origin of the Bermuda volcanoes and the Bermuda Rise: history, observations, models, and puzzles', *Geol. Soc. Am. Special Papers* **430**, 553–591, doi: 10.1130/SPE430.

Wald, D. J., Quitoriano, V., Worden, C. B., Hopper, M. & Dewey, J. W. (2012), 'USGS "Did You Feel It?" Internet-based macroseismic intensity maps', *Annals of Geophysics* **54**(6), 688–707, doi: 10.4401/ag–5354.

Wang, H., Zhao, D., Huang, Z. & Wang, L. (2019), 'Tomography, seismotectonics, and mantle dynamics of central and eastern United States', *J. Geophys. Res. Solid Earth* **124**(8), 8890–8907, doi: 10.1029/2019JB017478.

Waszek, L., Schmerr, N. C. & Ballmer, M. D. (2018), 'Global observations of reflectors in the mid-mantle with implications for mantle structure and dynamics', *Nat. Commun.* **9**(1), 1–13, doi: 10.1038/s41467–017–02709–4.

Wessel, P., Smith, W. H. F., Scharroo, R., Luis, J. & Wobbe, F. (2013), 'Generic Mapping Tools: Improved version released', *Eos Trans. AGU* **94**(45), 409–410, doi: 10.1002/2013EO450001.

Wielandt, E. (2012), Seismic sensors and their calibration, *in* P. Bormann, ed., 'New Manual of Seismological Observatory Practice 2 (NMSOP-2)', Deutsches GeoForschungsZentrum, IASPEI, Potsdam, Germany, chapter 5, pp. 1–51, doi: 10.2312/GFZ.NMSOP–2_ch5.

Yang, X., Pavlis, G. L. & Wang, Y. (2016), 'A quality control method for teleseismic *P*-wave receiver functions', *B. Seismol. Soc. Am.* **106**(5), 1948–1962, doi: 10.1785/0120150347.

Yu, Y., Song, J., Liu, K. H. & Gao, S. S. (2015), 'Determining crustal structure beneath seismic stations overlying a low-velocity sedimentary layer using receiver functions', *J. Geophys. Res. Solid Earth* **120**(5), 3208–3218.

Zelt, B. C. & Ellis, R. M. (1999), 'Receiver-function studies in the Trans-Hudson orogen, Saskatchewan', *Can. J. Earth Sci.* **36**(4), 585–603.